ELECTRON DOSE DISTRIBUTION NEAR TISSUE-BONE INTERFACES

ELECTRON DOSE DISTRIBUTION NEAR TISSUE-BONE INTERFACES

BY

PHILIP JOHN BIALOBZYSKI, B.Sc.

A Project Report
Submitted to the School of Graduate Studies
in Partial Fulfillment of the Requirements
for the Degree
Master of Science

McMaster University
February 1987

MASTER OF SCIENCE (1987) McMASTER UNIVERSITY
(Physics)

TITLE: Electron Dose Distribution Near Tissue-Bone Interfaces

AUTHOR: Philip John Bialobzyksi, B.Sc.
(University of Alberta)

SUPERVISOR: Dr C.S. Kwok, Ph.D.

NUMBER OF PAGES: xi, 115

ABSTRACT

Recent advances in immunological technology have made it feasible to investigate the diagnosis and treatment of cancer with radiolabelled anti-tumor antibodies. The red bone marrow and endosteal cells of bone are likely to be the dose limiting tissues for systemic applications. Therefore, it is of clinical importance to quantitate their dose.

Due to the small size of the marrow cavities in trabecular bone, it is experimentally difficult to measure the electron dose distribution. A computer simulation of electron transport is used to determine the dose distribution inside the marrow cavity.

Electrons are backscattered more from bone than soft tissue, thereby increasing the dose to the radiosensitive endosteum and red bone marrow. A point source of beta activity (^{204}Tl and ^{147}Pm) sandwiched between planar slabs of bone and red bone marrow equivalent plastics and ^{7}LiF thermoluminescent dosimeters (TLD's) were used to determine the dose increase at various distances from the interface.

Experimental results were compared with calculations using the Monte Carlo codes EGS (Electron Gamma Shower, SLAC) and CYLTRAN (Oak Ridge National Laboratory). The planar geometry was used as a benchmark geometry to compare the computer codes with experiment.

After checking the accuracy of the codes for low energy electron transport, ACCEPT, a version of CYLTRAN, was used to investigate the radiation dose increase due to a point source of beta activity inside a polystyrene sphere bounded by aluminum. Spheres with radii of 200 and 500 microns were used.

ACKNOWLEDGEMENTS

I am appreciative of the opportunity and financial support from McMaster University and Dr. Kwok to complete this work.

A special thanks to Dorothy Mackeson who typed this manuscript.

TABLE OF CONTENTS

LIST OF FIGURES

List of Figures, continued

List of Figures, continued

List of Figures, continued

LIST OF TABLES

CHAPTER 1

INTRODUCTION

Recent advances in immunological technology have made it feasible to investigate the diagnosis and treatment of cancer with radiolabelled antibodies. The red bone marrow and endosteal cells of bone are likely to be the dose limiting tissues for systemic applications. Therefore, it is of clinical importance to quantitate their dose.

Due to the small size of the marrow cavities in trabecular bone, it is experimentally difficult to measure the electron dose distributuon. A computer simulation of electron transport is used to determine the dose distribution inside the marrow cavity.

Electrons are backscattered more from bone than soft tissue thereby increasing the dose to the radiosensitive endosteum and red bone marrow. A point source of low energy, beta activity (^{204}Tl and ^{147}Pm) sandwiched between planar slabs of bone and red bone marrow equivalent plastics and LiF thermoluminescent

dosimeters (TLD's) were used to determine the dose increase at various distances from the interface. Experimental results are compared with calculations using the Monte Carlo codes (Electron Gamma Shower, SLAC) and CYLTRAN (Oak Ridge National Laboratory). The planar geometry was used as a benchmark geometry to check the accuracy of the computer codes.

After checking the accuracy of the codes for low energy electron transport, ACCEPT, a version of CYLTRAN, was used to investigate the radiation dose increase due to a point source of beta activity inside a polystyrene sphere bounded by aluminum. Sphere radii of 200 and 500 microns were used corresponding to the size of typical marrow cavities inside trabecular bone (SPI69) (ECK85b).

This chapter gives background material on topics relevant to this project, namely: radioimmunotherapy, bone morphology, thermoluminescent dosimetry, the Monte Carlo method and electron interaction with matter.

RADIOIMMUNOTHERAPY

It is now possible to raise high titers of antibodies to antigens which are present on the surface of tumor cells but are at much lower density on normal

cells (HEL82). Investigations in animal tumor models have verified that antibodies can be given systemically with subsequent localization in foci of tumor cells (DEV85). These antibodies can be conjugated with chemotherapeutic drugs or radiolabelled providing a specific delivery system of cytotoxic agents to the tumor site(s). Radiolabelled antibodies provide a method of diagnosis (radioimmunodetection) and therapy (radioimmunotherapy). Radioimmunodetection offers complementary information (GOL80)(RAI83)(FAR82) which may even prove superior to existing diagnostic procedures (EPE82). Early clinical trials of radioimmunotherapy have shown lethal effects on tumor cells without excessive toxicity to patients (HAM84)(CAR84).

It is envisioned that radiommunotherapy will be performed predominantly by particulate radiation (WES86), beta emitters (^{47}Sc, ^{67}Cu, ^{131}I, and ^{90}Y), positron emitters (^{64}Cu, ^{77}Br, ^{89}Zr) and alpha emitters (^{211}At, ^{212}Bi)(FIS85). A systemic introduction of radiolabelled antibodies would be limited by the dose to the radiosensitive red bone marrow and endosteum (BIG85). It is therefore of clinical importance to quantitate the dose to these tissues. MIRD type dosimetry fails to be predictive when examining

particulate radiation in the sub-centimeter range, at tumor boundaries and at organ interfaces (WES86). Therefore, a study of the electron dose distribution near tissue-bone interfaces in the sub-centimeter range is relevant.

BONE MORPHOLOGY

There are two types of bone in the human body, cortical or hard bone and trabecular or spongy bone. Trabecular bone is composed of thin lamellae of cortical bone (trabeculae) which forms a meshwork of interconnecting spaces which are filled with red or yellow bone marrow. Red marrow is composed of the active hematopoietic cells. Yellow marrow is a structure of fibrous tissue and fat. The specific gravities of cortical bone, red marrow and yellow marrow are 1.90, 1.03 and 0.98 respectively (WOO82).

Trabecular bone is found in the interior of all bones, especially the flat bones and the ends of the long bones. Figure 1-1 (SPI69) shows a cross section of the femur, lumbar vertebrae and hip, note the cancellous network of marrow cavities of trabecular bone and outer cortex of cortical bone.

Figure 1-1
Cross Sections of Human Bones

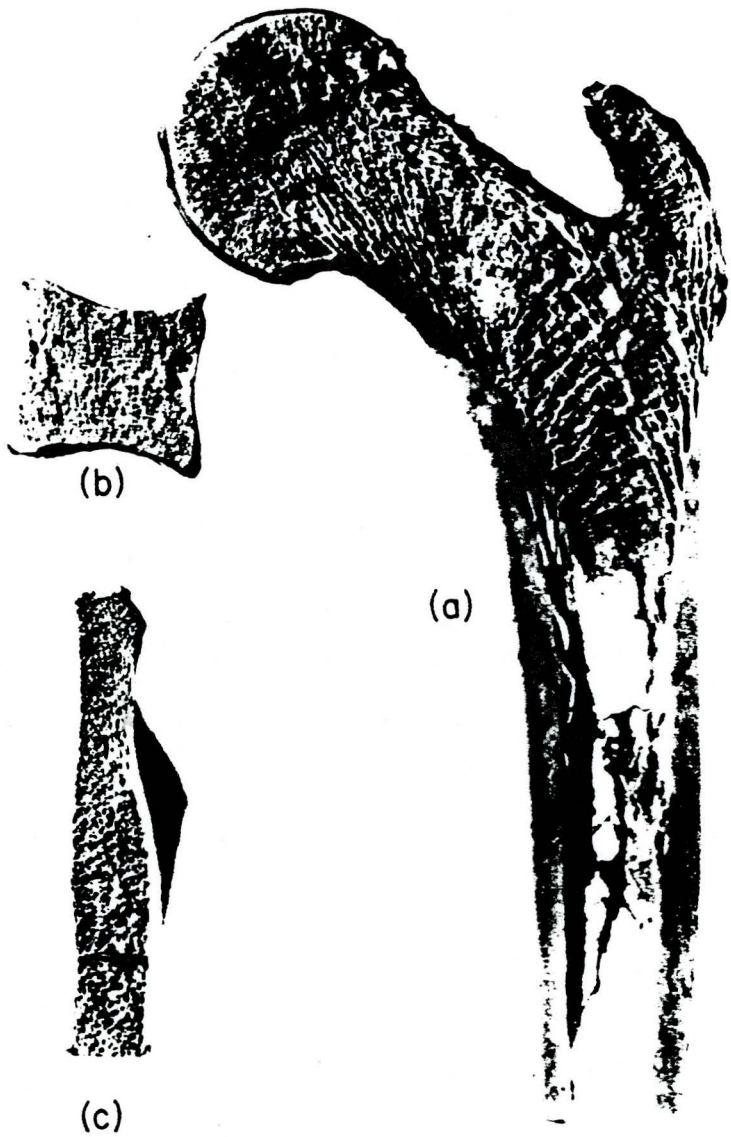

Sections of human bones: (*a*) shaft and upper end of femur; (*b*) lumbar vertebra; (*c*) part of the hip bone through the iliac crest.

Trabecular bone cannot be represented by simple geometric shapes. Spiers (SPI69) has presented the size of the marrow cavities in terms of the frequency distribution of particle path lengths traversing the marrow cavities. Figure 1-2 (SPI69) is the frequency distribution versus the mean linear dimension of the cavity size in microns. The cavities have a linear dimension which varies from 50 to 2,000 microns.

Bone marrow toxicity is the most clinically important and the most consistently and frequently encountered toxicity associated with current systemic cancer therapy (HOA84)(CRE77). Two tissues associated with the skeleton that are of primary concern with respect to cancer induction by ionizing radiation are the near endosteal surfaces (a cellular layer 10 microns thick) from which osteosarcomas are thought to arise and the hematopoietic bone marrow, considered the target tissue with respect to the induction of leukemia (ECK85b).

THERMOLUMINESCENT DOSIMETERS (TLDs)

Some inorganic crystals when subject to ionizing radiation trap electrons at its lattice defects. The electrons have a small probability per unit time of

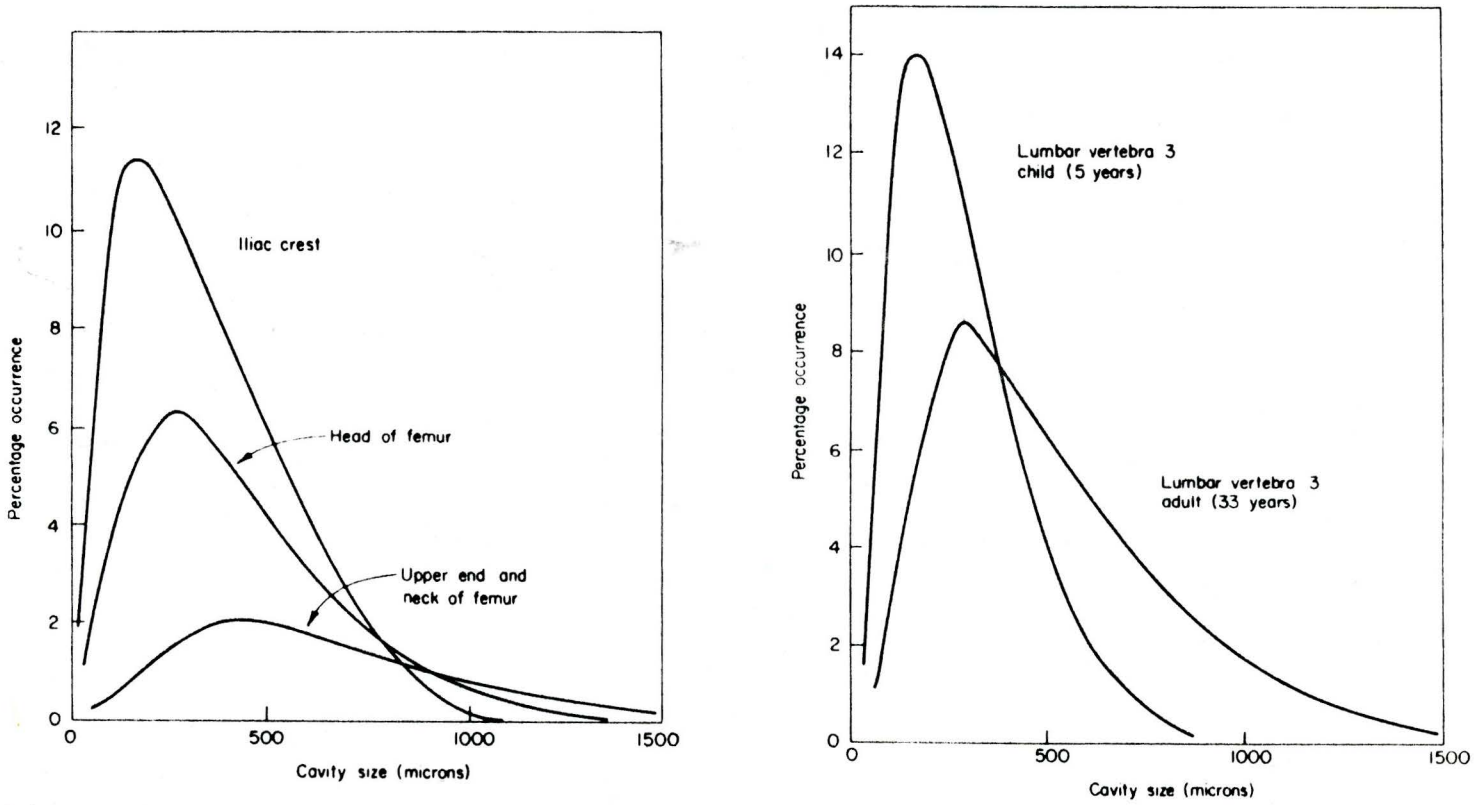

Figure 1-2
Marrow Cavity Size

Typical distribution of marrow cavity size in bones indicated (mean linear dimensions.)

escaping these "trapping centers" at room temperature. As the solid is heated the probability of escape increases. The electron escapes if enough thermal energy is supplied to the solid (the same argument applies to holes). Once having escaped, the electrons can then migrate to combine with holes or holes migrate to combine with trapped electrons releasing a photon of typically 3-4eV. The number of photons released in the heating process is directly proportional to the dose that the solid has received. The number of photons as a function of temperature is referred to as its "glow curve", the area under the glow curve is the TLD response and is proportional to the dose.

Not all the electron traps are of the same energy depth. An electron trap of low energy depth may be unstable at room temperature; it is therefore necessary to allow the TLD to "fade". Fading allows the depletion of the unstable energy traps before reading out the TLD. Without adequate fading the TLD response would depend upon the time after exposure.

To determine the TLD response, the TLD is heated to a temperature high enough to deplete most of its electron traps. During the process the amount of light

emitted is integrated and displayed. The TLD can be annealed at higher temperature to ensure all traps have been depleted and re-used.

In this project, lithium fluoride (^{7}LiF) powder in a teflon matrix was used to measure the dose increase due to electron backscatter from a planar interface of cortical bone and red marrow equivalent plastics. The LiF glow curve is shown in Figure 1-3 (CON67). LiF should be allowed to fade for 24 hours after exposure to eliminate a low temperature glow peak (KAS67). The TLD response versus dose for LiF is linear up to 10 Gy (10^{3}rad) for ^{60}CO gamma rays. The LiF TLDs used were calibrated individually with ^{60}CO gamma rays using the AECL Theratron 780, Hamilton Cancer Clinic, Hamilton, Ontario. Records of sensitivity and history for each TLD were kept throughout the experiment.

LiF is ideal for measuring high doses of low energy electrons (BAR75). Kastner et al (1967) observed that the response of LiF to electrons parallels that to ^{60}CO gamma rays but with a significant loss in sensitivity. (This loss in sensitivity does not affect the results of this work, the signal to noise ratio being typically 50.)

Figure 1-3
Glow Curves of some TLD Materials.

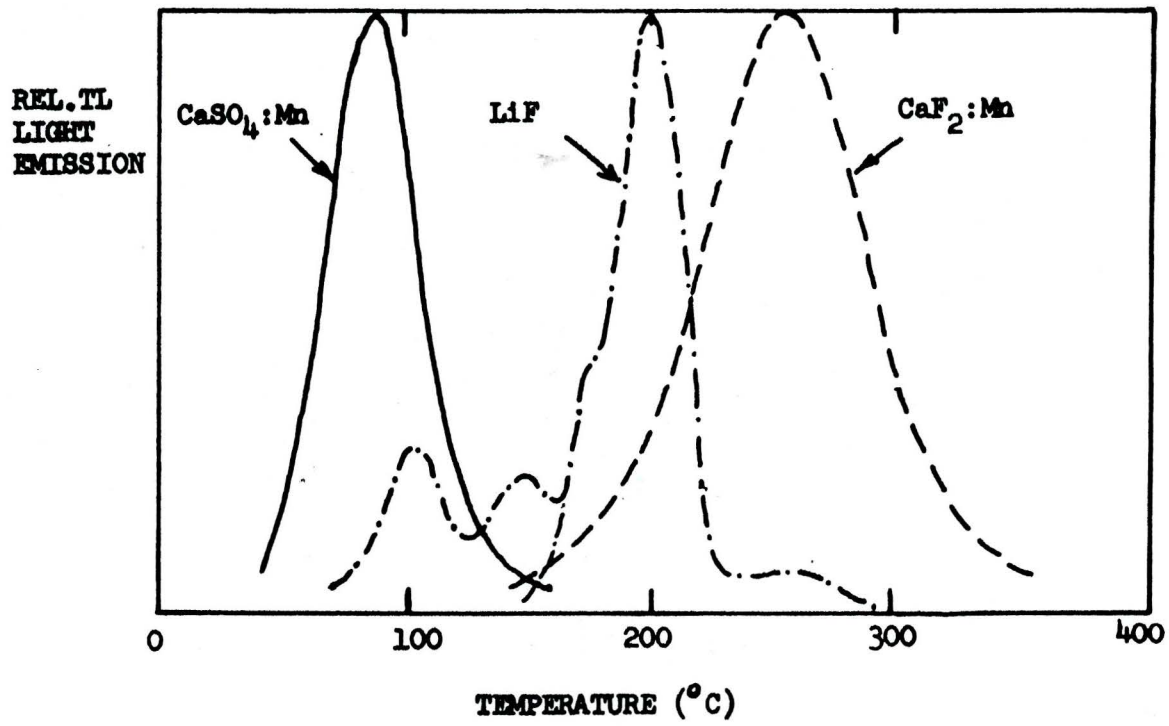

Glow curves of $CaSO_4$:Mn, LiF and CaF_2:Mn. The curves are arbitrarily normalized to the same maximum height.

MONTE CARLO METHOD

The term "Monte Carlo" in 1942 denoted a secret file at Los Alamos concerning studies of this method by Von Neuman (LAT69). The Monte Carlo method makes use of random numbers to determine the outcome of chance events. There are many applications of the Monte Carlo method. Originally, the method was applied to particle transport, which is the application used in this project.

The Monte Carlo method is a computer simulation of actual physical processes which govern the particle's behaviour. A large number (10^4) of computer simulated "particle life histories" are tracked using random sampling techniques to sample the probability laws that describe the particle interactions (WOOD82).

A large number of histories must be used for statistical accuracy. This number may be limited by CPU time, real time and the large sequence of random numbers needed.

Energy deposited, fluence and other properties of the particles may be scored in geometrical regions defined by the user in the simulation. To ascertain the accuracy of the simulations used a comparison was done

with experiment in this project.

ELECTRON INTERACTION WITH MATTER.

Electrons interacting with matter lose energy by collision and radiation (bremsstrahlung). Elastic and inelastic collisions with nuclei and bound atomic electrons are possible. For electron energies below a few MeV, radiative losses are a small fraction of energy losses due to ionization and excitation. The mass of the orbital electron is equal to the incident electron hence large energy transfers and abrupt changes in path occur. Elastic scattering from orbital electrons occurs for electrons of energy less than 100eV (EVA55).

The specific energy loss due to ionization and excitation (collisional energy losses) derived by Bethe (KNO79) takes the following form:

$$-\left(\frac{dE}{dx}\right)_c = \frac{2\pi e^4}{m_e v^2} NZ \left[\ln \frac{m_e v^2 E}{2I^2(1-\beta^2)} - \ln 2 \,(2\sqrt{1-\beta^2} - 1+\beta^2) + (1-\beta^2) + \frac{1}{8}(1-\sqrt{1-\beta^2})^2 \right]$$

Where:

N = number density of absorber atoms

Z = atomic number of absorber atoms

e = electronic charge

m_0 = electron rest mass

I = average excitation and ionization potential of absorber

v = velocity of electron

β = v/c where c is the speed of light in vacuum

E = electron energy

The linear specific energy loss for the radiative process is (KNO79).

$$-\left(\frac{dE}{dx}\right)_r = \frac{NEZ(Z+1)}{137\, m_0^2 c^4}\, e^4 \left[4 \ln \frac{2E}{mc^2} - \frac{4}{3}\right]$$

where the terms have the same meaning as in the preceeding equation.

The total linear stopping power is the sum of the collisional and radiative stopping powers:

$$\frac{dE}{dx} = \frac{dE}{dx}_c + \frac{dE}{dx}_r$$

Figure 1-4 is a plot of the mass stopping power (total linear stopping power divided by the density of the absorber) versus electron energy for polystyrene (density 1.06 g/cm^3) (ICRU37). Note the high linear energy transfer (LET) for low energy electrons.

Figure 1-4

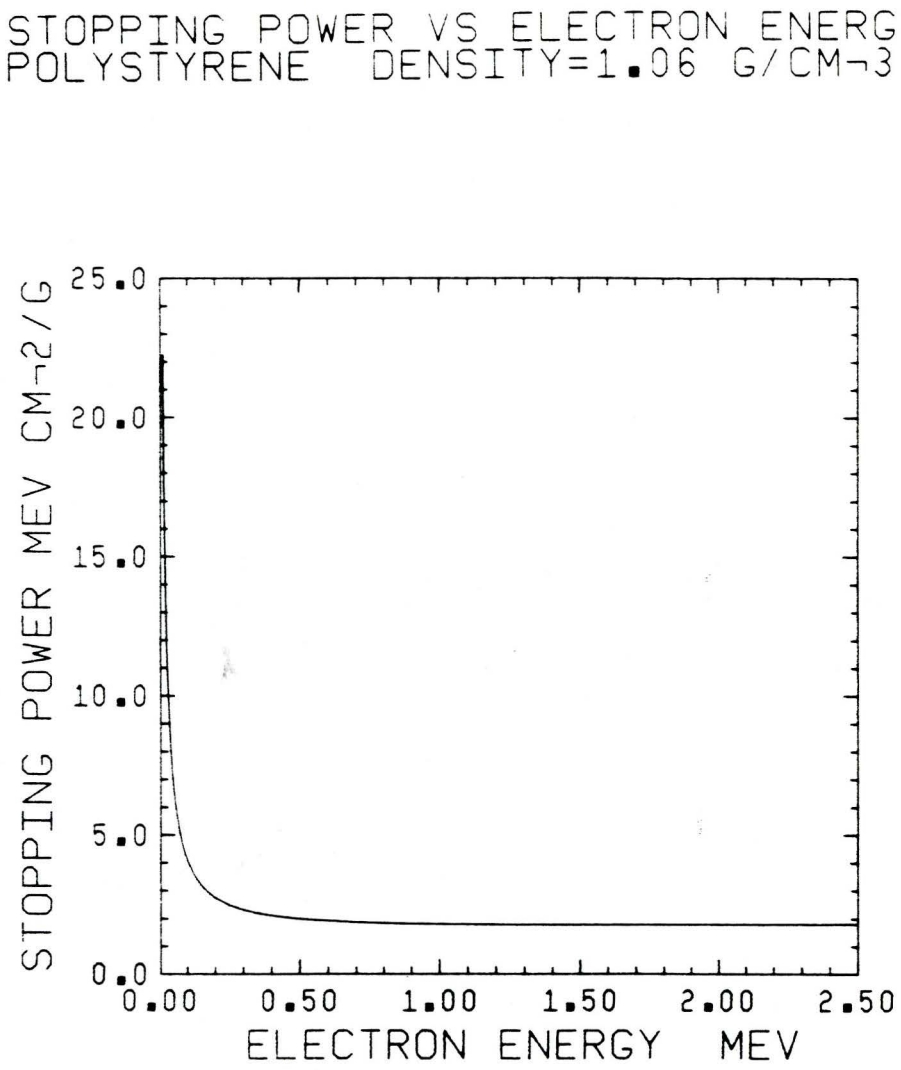
STOPPING POWER VS ELECTRON ENERGY
POLYSTYRENE DENSITY=1.06 G/CM¬3
STOPPING POWER MEV CM¬2/G
25.0
20.0
15.0
10.0
5.0
0.0
0.00
0.50
1.00
1.50
2.00
2.50
ELECTRON ENERGY MEV

Figure 1-5 shows the behaviour of mass stopping power at low electron energy (ICRU37) for polystyrene.

Electrons undergoing large angle deflections may be "backscattered". Backscatter is pronounced for electrons with low incident energy and absorbers of high atomic number.

Figure 1-5
Stopping Power vs Electron Energy

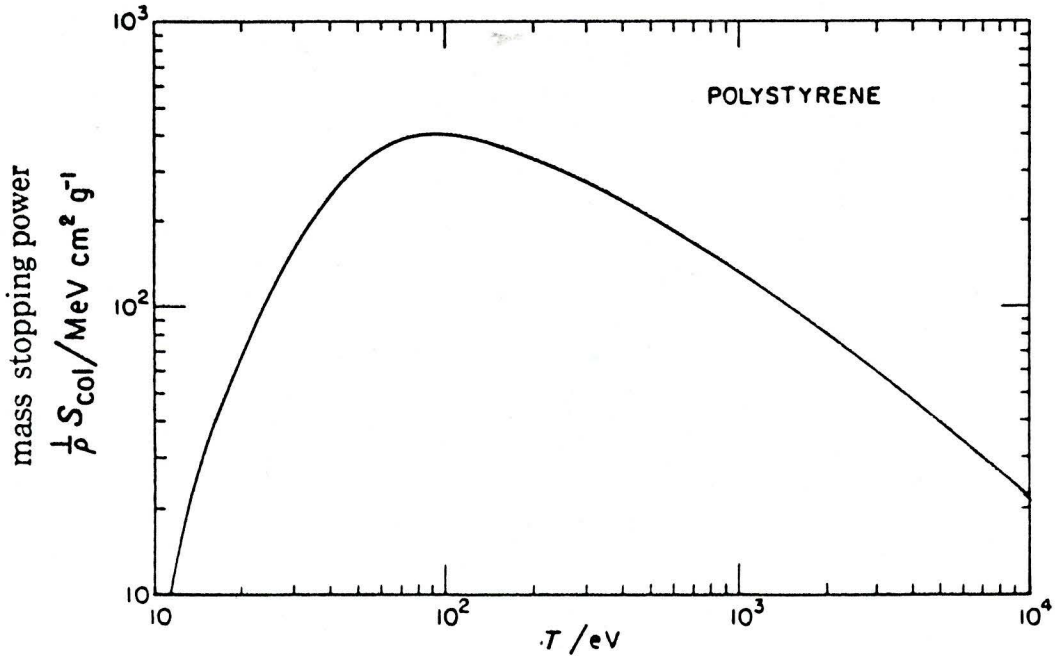

Stopping power for polystyrene (1.04 g/cm^3) for energies below 10KeV. T is the electron kinetic energy in eV.

CHAPTER 2

EXPERIMENTAL MEASUREMENT OF DOSE INCREASE DUE TO ELECTRON BACKSCATTER

The dose increase due to electron backscatter was measured in a planar geometry of cortical bone and red marrow equivalent plastics. A point source of beta activity (Promethium-147, Thallium-204, Phosphorus-32 representing beta emitters of increasing average energy)[1] and lithium fluoride (LiF) thermoluminescent dosimeters (TLDs) were used to measure the dose increase due to electron backscatter at various distances from the interface. In this chapter, the materials/methods, experimental procedure, and results of this experiment are presented.

MATERIALS AND METHODS

The materials used for this experiment were: LiF, TLDs, beta point sources of Thallium-204 and Promethium-147, cortical bone and red marrow equivalent plastic.

---

[1]Experimental determination of ^{32}P dose increase was performed by: Kwok, et al (1985) using a planar aluminum and polystyrene geometry.

Discs of LiF in teflon were obtained from Teledyne Isotopes, Westwood, New Jersey, 6.0 and 5.0 mm diameter respectively (density 2.39 g/cm^3). The LiF discs were calibrated with ^{60}Co gamma rays, 600 rads for the 12 mg/cm^2 and 300 rads for the 31 mg/cm^2 thicknesses. The response of the TLD to this calibration dose is referred to as its "sensitivity" or "sensitivity factor" which appears in the folowing dose calculations. The identity of each TLD was retained and records of sensitivity and history were kept.

Exposed discs were allowed to fade for 24 hours before being read out with a Con-Rad TLD Reader, Model 5100B Readout Instrument (Controls for Radiation Inc., Cambridge, Massachusetts) hereafter referred to as the "TLD reader".

The procedure for readout of exposed LiF discs was as follows: the TLD reader was allowed to stabilize at a photomultiplier voltage of 1080 volts. A calibration light source (tritium in a phosphor) was then used to adjust the photomultiplier tube voltage to obtain the same sensitivity as previous sessions. (The sensitivity of the photomultiplier decreases with use due to the optical coupling between the photomultiplier and

aluminum heating planchette collecting airborne residue from the heated TLDs). The heating current for the aluminum planchette was set to 0.5 Amp, the external timer setting was 4 seconds.

Figure 2-1 is an analog output of calibration light source reading and LiF glow curve for an external timer setting of four seconds. The TLD reader has a constant current heating cycle so temperature as a function of time is not linear. The method used to verify that the appropriate temperature was reached for the LiF discs was to compare the analog glow curve with the accepted glow curve from the literature.

An unexposed TLD was placed in the aluminum planchette and read twice. The initial background reading was acquired and 25 seconds later it was read again for the residual background. Likewise each exposed TLD was read twice, first for the initial reading and 25 seconds later for the residual reading. The initial and residual readings were added and background total subtracted for the "TLD response" used in dose calculations.

Figure 2-1
Analog output of calibration light source
and LiF glow curve.

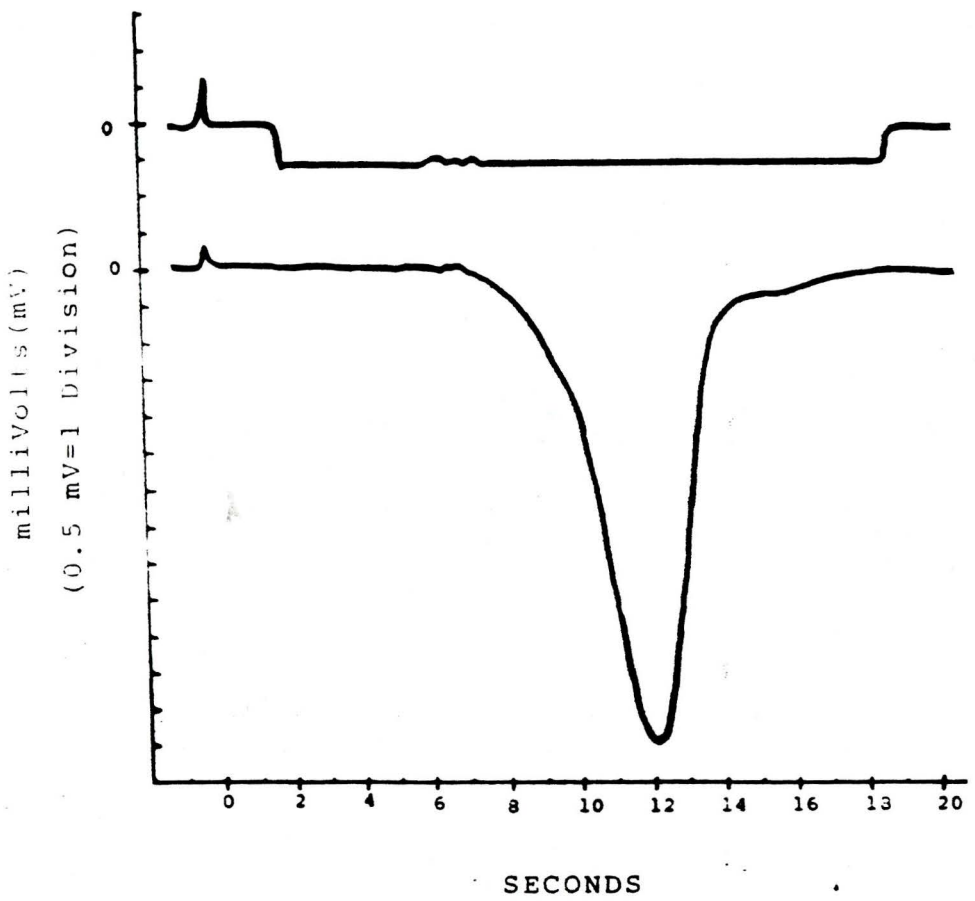

Analog output of calibration light source (upper) and exposed LiF TLD disc (lower) for external timer setting of 4 seconds.

After reading ten TLDs a "recalibration" was performed to adjust the tube voltage if necessary, and a background reading with an unexposed disc was repeated.

The TLD discs were annealed in an aluminum multiwell tray after each readout procedure, two hours at 415°C and 24 hours at 80°C. A group of ten TLDs was designated as a sensitivity control group which were "recalibrated" after each annealing procedure to monitor sensitivity change. The sensitivity of the TLDs was observed to decrease by 0-6% after each annealing.

Sources of beta activity were obtained from Amersham International Inc., Oakville, Ontario. Thallium-204 (^{204}Tl) and Promethium-147 (^{147}Pm) point sources were made by depositing one microlitre droplets of activity in aqueous solution on aluminized mylar (5.6 mg/cm^2 thick), allowed to evaporate and then sealed with scotch tape (5.2 mg/cm^2 thick). (The sources arrived in acidic solutions which needed to be neutralized to retain the integrity of the aluminum coating on the mylar.) The aluminized mylar was grounded during experimental procedures to prevent electrostatic charge build-up.

Source size was checked by autoradiography. Sources of diameter 2mm or less were used in experiments. The estimated activity of the point sources are: ^{147}Pm 3.7 MB_q (100 microCurie), ^{204}Tl 74 kB_q (2 microCurie). Figures 2-2 through 2-4 are a description of beta decay for the nuclides involved (ICRP38). Phosphorus -32 is included due to its appearance in the results. Note that ^{147}Pm decays to an alpha emitting isotope of samarium (^{147}Sm) with half life of 10^{11} years. This has an insignificant effect on the results of this experiment.

The cortical bone and red marrow equivalent plastics were obtained from Mihaela Cosma, Sloane Kettering Cancer Center, New York, New York. The plastics have approximately the same number of electrons per gram, electrons per cubic centimeter and mass density as real tissue. Table 2-1 compares the plastic with real tissue. Real tissue calculations are from H.Q. Woodward (1982).

Figure 2-2
Decay of Prometheum -147

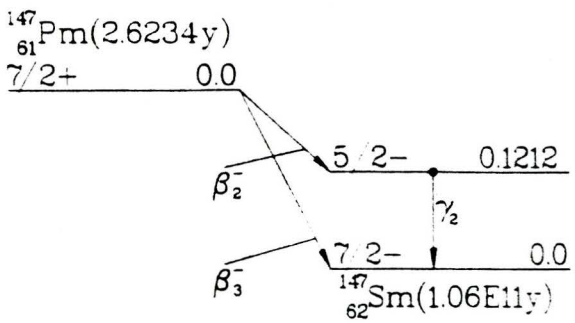

61-PROMETHIUM-147

HALFLIFE = 2.6234 YEARS 18-AUG-78
DECAY MODE(S): β^-

RADIATION	y(i) (Bq-s)$^{-1}$	E(i) (MeV)	y(i)×E(i)
β^- 3	1.00E 00	6.196E-02*	6.20E-02
γ 2	2.85E-05	1.212E-01	3.45E-06
Kα_1 X-ray	1.13E-05	4.012E-02	4.52E-07
Kα_2 X-ray	6.22E-06	3.952E-02	2.46E-07
Kβ_1 X-ray	2.21E-06	4.541E-02	1.00E-07
Kβ_2 X-ray	9.69E-07	4.661E-02	4.52E-08
Kβ_3 X-ray	1.14E-06	4.529E-02	5.16E-08
Lα X-ray	1.69E-06	5.633E-03*	9.54E-09
Lβ X-ray	1.57E-06	6.297E-03*	9.86E-09

LISTED X, γ AND $\gamma\pm$ RADIATIONS	4.37E-06
OMITTED X, γ AND $\gamma\pm$ RADIATIONS**	4.35E-09
LISTED β, ce AND Auger RADIATIONS	6.20E-02
OMITTED β, ce AND Auger RADIATIONS**	4.12E-06
LISTED RADIATIONS	6.20E-02
OMITTED RADIATIONS**	4.12E-06

* AVERAGE ENERGY (MeV)
** EACH OMITTED TRANSITION CONTRIBUTES <0.100% TO Σy(i)×E(i) IN ITS CATEGORY.
SAMARIUM-147 DAUGHTER IS RADIOACTIVE.

Figure 2-3
Decay of Thallium -204

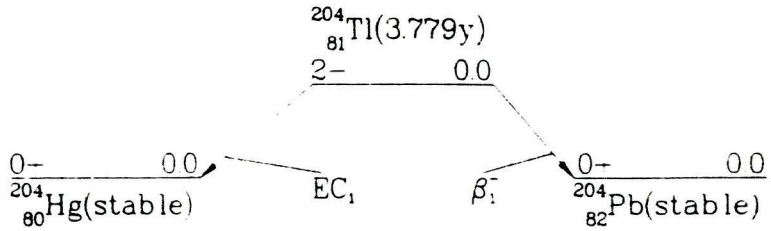

81-THALLIUM-204

HALFLIFE = 3.779 YEARS 01-OCT-78
DECAY MODE(S): EC, β^-

RADIATION	y(i) $(Bq-s)^{-1}$	E(i) (MeV)	y(i)×E(i)
$K\alpha_1$ X-ray	7.12E-03	7.082E-02	5.04E-04
$K\alpha_2$ X-ray	4.19E-03	6.889E-02	2.89E-04
$K\beta_1$ X-ray	1.62E-03	8.026E-02	1.30E-04
$K\beta_2$ X-ray	6.84E-04	8.258E-02	5.65E-05
$K\beta_3$ X-ray	8.45E-04	7.982E-02	6.74E-05
$K\beta_5$ X-ray	4.44E-05	8.077E-02	3.59E-06
Lα X-ray	3.35E-03	9.980E-03*	3.34E-05
Lβ X-ray	3.00E-03	1.185E-02*	3.55E-05
Lγ X-ray	5.51E-04	1.398E-02*	7.70E-06
Ll X-ray	1.30E-04	8.722E-03	1.13E-06
β^- 1	9.74E-01	2.439E-01*	2.38E-01

LISTED X, γ AND γ± RADIATIONS	1.13E-03
OMITTED X, γ AND γ± RADIATIONS**	7.67E-07
LISTED β, ce AND Auger RADIATIONS	2.38E-01
OMITTED β, ce AND Auger RADIATIONS**	2.29E-04
LISTED RADIATIONS	2.39E-01
OMITTED RADIATIONS**	2.30E-04

* AVERAGE ENERGY (MeV)
** EACH OMITTED TRANSITION CONTRIBUTES <0.100% TO Σy(i)×E(i) IN ITS CATEGORY.
MERCURY-204 DAUGHTER, YIELD 2.58E-02, IS STABLE.
LEAD-204 DAUGHTER, YIELD 9.742E-01, IS STABLE.

Figure 2-4
Decay of Phosphorus -32 and Samarium -147

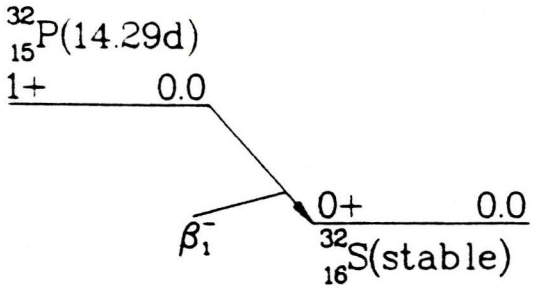

15-PHOSPHORUS-32

HALFLIFE = 14.29 DAYS 27-DEC-77
DECAY MODE(S): β

RADIATION	γ(i) (Bq-s)	E(i) (MeV)	γ(i)×E(i)
β 1	1.00E 00	6.947E-01*	6.95E-01

LISTED β, ce AND Auger RADIATIONS 6.95E-01
LISTED RADIATIONS 6.95E-01

* AVERAGE ENERGY (MeV)
SULPHUR-32 DAUGHTER IS STABLE.

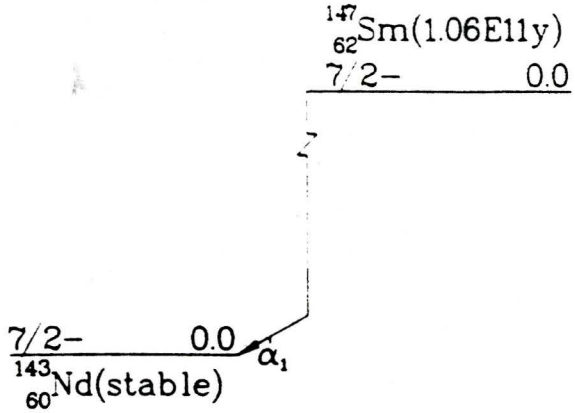

62-SAMARIUM-147

HALFLIFE = 0.106E 12 YEARS 19-SEP-78
DECAY MODE(S): α

RADIATION	γ(i) (Bq-s)⁻¹	E(i) (MeV)	γ(i)×E(i)
α 1	1.00E 00	2.248E 00	2.25E 00
α recoil	1.00E 00	6.291E-02	6.29E-02

LISTED α AND α recoil RADIATIONS 2.31E 00
LISTED RADIATIONS 2.31E 00

NEODYMIUM-143 DAUGHTER IS STABLE.

Table 2-1

Comparison of Tissue equivalent plastics with Real Tissue

TEP = Tissue equivalent plastics
RT = Real Tissue

Element	Z	Cortical Bone (g/100g) TEP	Cortical Bone RT	Red Marrow (g/100g) TEP	Red Marrow RT
H	1	2.5416	3.39	10.16	10.49
C	6	28.5540	15.50	74.48	41.60
N	7	0.8940	3.97	1.92	3.40
O	8	40.4459	44.10	13.33	44.28
Cl	17	0.5100	-	0.11	-
Ca	20	26.8268	22.20	-	-
Mg	12	0.2958	0.21	-	-
S	16	0.3903	0.31	-	-
Fe	26	-	-	-	0.08
Na	11	-	0.06	-	0.04
P	15	-	10.20	-	0.19
K	19	-	-	-	0.18
TOTAL		100.4584	99.94	100.00	100.26

	Specific Gravity TEP	Specific Gravity RT	Electrons/g ($\times 10^{23}$) TEP	Electrons/g ($\times 10^{23}$) RT	Electrons/cm ($\times 10^{23}$) TEP	Electrons/cm ($\times 10^{23}$) RT
Cortical Bone	1.901	1.90	3.0595	3.0981	5.8154	5.9485
Red Marrow	1.047	1.03	3.4656	3.3285	3.4284	3.4284

EXPERIMENTAL PROCEDURE

A pair of LiF TLD discs with matched sensitivity and history was used to measure the dose increase in a planar geometry of cortical bone (BONE) and red marrow (RM) equivalent plastics. As shown in Figure 2-5 one of the pair, TLD#1, was placed in a cortical bone - red marrow geometry (BONE-RM) and exposed for a time T1. The second TLD#2, was placed in the same position with red marrow plastic in place of cortical bone plastic (RM-RM) and exposed for a time T2.

After exposure the pair was allowed to fade and then read out consecutively. The dose ratio was calculated as follows:

$$\text{Dose Ratio} = \frac{\text{Response TLD\#1} \times \text{Exposure Time T2} \times \text{Sensitivity factor TLD\#2}}{\text{Response TLD\#2} \times \text{Exposure Time T1} \times \text{Sensitivity factor TLD\#1}}$$

where the sensitivity factor is the TLD response to the ^{60}Co calibration dose.

The position of the TLD was varied by placing known thicknesses ($\triangle X$) of red marrow plastic between the dosimeter and the source, as shown in Figure 2-6.

Figure 2-5
Experimental Procedure - Geometry.

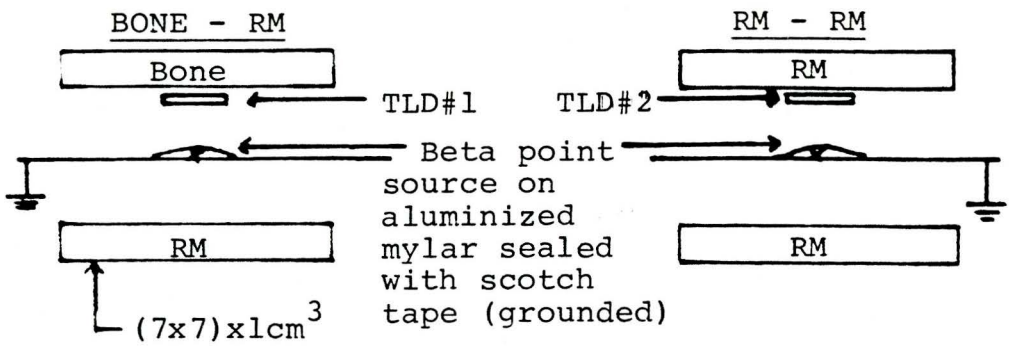

(Assembly is compressed during exposure)

Figure 2-6
Variation of TLD distance from interface.

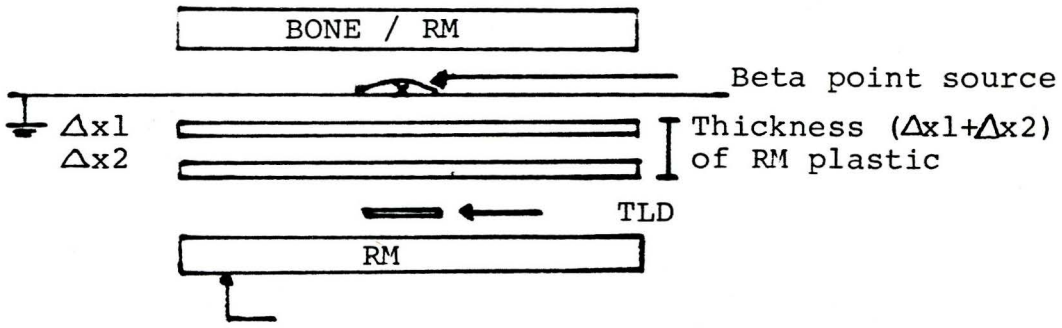

(Assembly is compressed during exposure)

RESULTS

Table 2-2 summarizes the results of this experiment, including results by Kwok et al (1985) for ^{32}P. The dose ratio is the average $\pm$ one standard deviation from the mean calculated from the number of trials indicated. The uncertainty in the dosimeter position is due to its thickness. Figure 2-7 is a graph of the results presented in Table 2-2.

Figure 2-8 is a semi-log graph of the percent backscatter dose versus separation from the (Bone-RM) interface for ^{204}Tl. This shows that the increase in dose due to electron backscatter decreases exponentially with the distance from the interface.

Table 2-2
Experimental Results

Isotope (Average Energy)* (End point Energy) MeV	Source distance from interface mg/cm^2	Energy of the** Average Energy emission on interface (MeV)	Energy of the*** Endpoint Energy on the interface (MeV)	TLD distance from interface mg/cm^2	# of Trials	Dose Ratio
32P	36	0.627	1.644	16±16	8	1.12±.03
(0.695)	36	0.627	1.644	140±16	8	1.08±.02
(1.710)	36	0.627	1.644	299±16	8	1.03±.03
	17	0.200	0.731	6±6	20	1.08±.03
204Tl	36	0.140	0.693	16±16	23	1.06±.03
(0.244)	5	0.231	0.753	132±16	18	1.05±.02
(0.763)	5	0.231	0.753	183±16	14	1.03±.02
^{147}Pm (0.062) (0.225)	17	0+	0.179	6±6	23	1.03±.03

* Taken from ICRP 38 (19)

** Energy of the average energy emission from isotope (first column) incident on Bone-RM interface

*** Energy of the endpoint energy emissions from isotope (first column) incident on Bone-RM interface

\+ "O" indicates the CSDA range for the average energy emission is shorter than the distance to the interface.

Figure 2-7

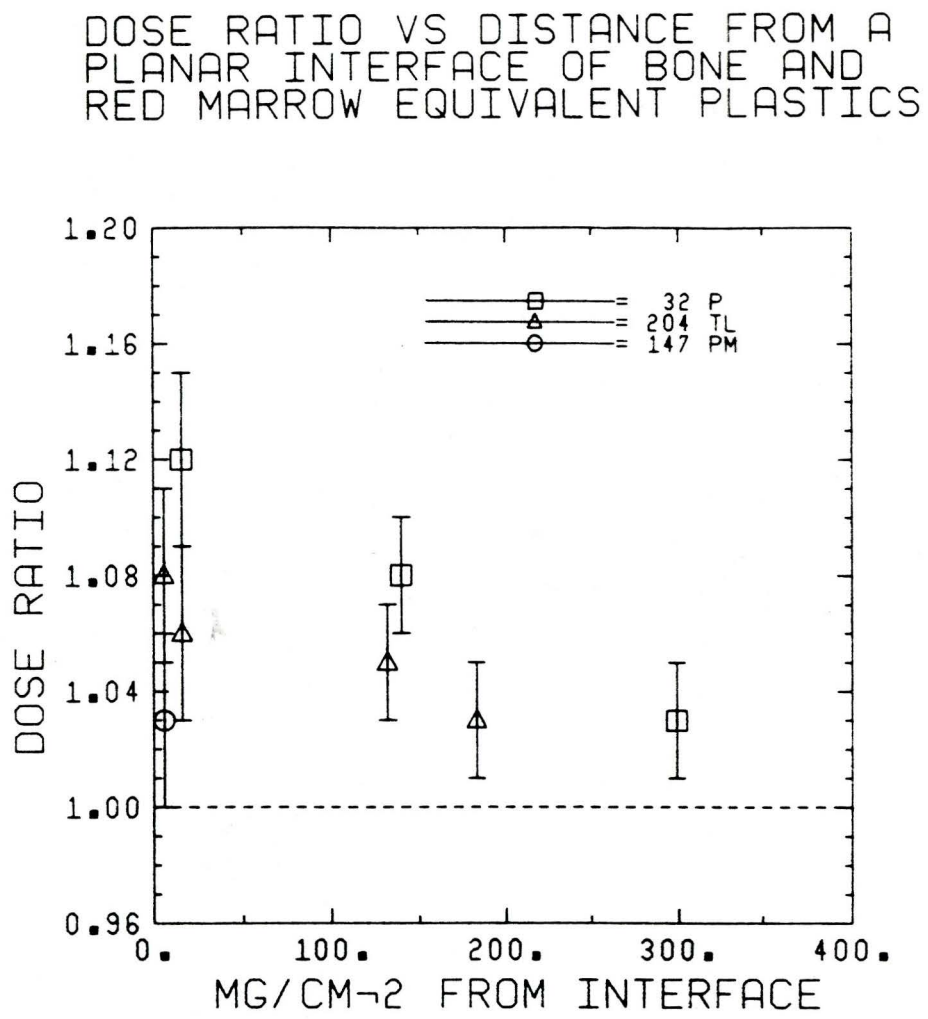
DOSE RATIO VS DISTANCE FROM A PLANAR INTERFACE OF BONE AND RED MARROW EQUIVALENT PLASTICS
= 32 P
= 204 TL
= 147 PM
DOSE RATIO
1.20
1.16
1.12
1.08
1.04
1.00
0.96
0.
100.
200.
300.
400.
MG/CM¬2 FROM INTERFACE

Figure 2-8

THALLIUM-204 PERCENT BACKSCATTER DOSE
FROM A PLANAR BONE-RED MARROW INTERFACE

(The data plotted is fit with function and parameters found in Appendix D)

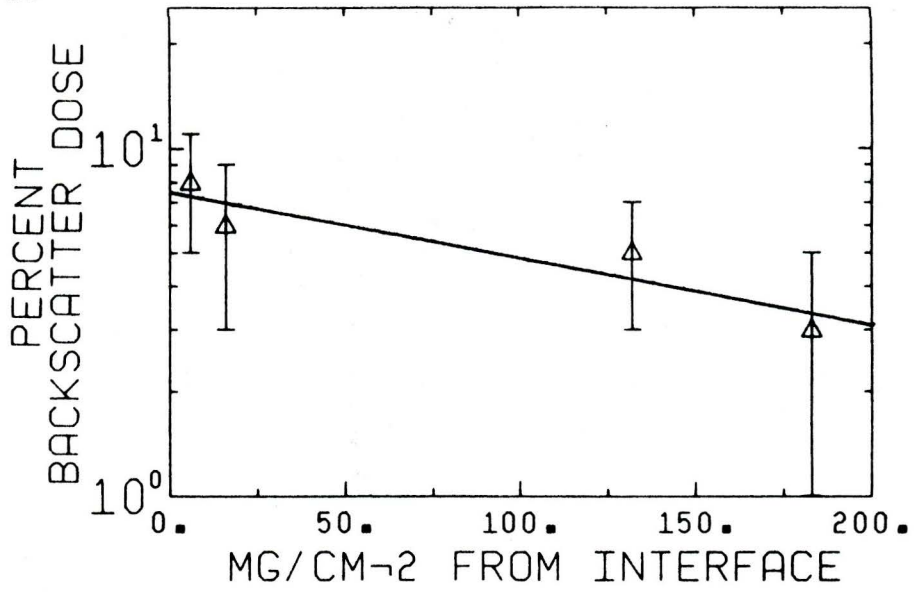

CHAPTER 3

COMPARISON OF EXPERIMENT WITH EGS AND CYLTRAN

This chapter presents a comparison of the measured dose ratios from the preceding chapter with the dose ratios generated by the Monte Carlo programs EGS and CYLTRAN. A planar geometry of aluminum (Al) and polystyrene (PST) was used to simulate the cortical bone and red marrow plastics used in the experiment. Curves of dose versus electron point source energy were generated for a region corresponding to the LiF TLD in the PST-Al and the PST-PST geometry. The dose in the TLD region due to a spectrum of electron energies was obtained by the integration of the "dose curve" with the electron energy spectrum. The validity of using the two codes for modelling the marrow cavities will be ascertained. I shall present the materials/methods, procedure and results of this investigation.

MATERIALS AND METHODS

Three computer programs were used in this investigation: EGS, CYLTRAN and a program which generated the beta spectra of the nuclides used in the experiment (^{204}Tl, ^{147}Pm, ^{32}P). Aluminum and polystyrene were

used in the simulation while cortical bone and red marrow equivalent plastics were used in the experiment, a comparison of the electron interaction properties of these materials is also presented.

EGS and CYLTRAN are Monte Carlo simulation programs for photon and electron transport in user defined media and geometry. EGS is an acronym for Electron Gamma Shower - Version IV was obtained from SLAC (Stanford Linear Accelerator, Stanford, Ca.) CYLTRAN was developed at Oak Ridge National Laboratory for the U.S. Department of Energy; it was obtained from Oak Ridge National Laboratory. (The codes are treated as black boxes in this investigation.)

The EGS user has to supply a suitable value for the parameter ESTEPE which controls the electron step size in the simulation. For low energy electrons variation of this parameter causes variation in the absolute dose deposited by several percent (RO684). This parameter was selected according to the criteria suggested by Rogers (1984), i.e. monitoring how often multiple scattering is not simulated and varying ESTEPE until the physical quality no longer changes significantly. EGS was run at different ESTEPE values to

determine an appropriate value. Figures 3-1 and 3-2 show the dose deposited in the 31 mg/cm^2 TLD scoring region for varying ESTEPE and electron point source energy. (A table of values for these figures is found in Appendix C, Table C-1.) In these figures, the parameter "NOSCAT" refers to the ratio of the number of steps EGS switched off multiple scattering to the total number of charged particle steps taken. An ESTEPE value of 0.01 was chosen for both geometries PST-Al and PST-PST because multiple scattering was not completely switched off and the dose values do not change significantly with ESTEPE.

The simulated experimental geometry for EGS and CYLTRAN used polystyrene and aluminum. A scoring region in polystyrene was defined to represent the ^{7}LiF TLD. The TLD discs have a density of 2.4 g/cm^3 and PST is 1.04 g/cm^3. To obtain the same mass thickness the dimensions of the TLD scoring region were scaled by a factor 2.4/1.04 times the actual TLD dimensions. The source size in CYLTRAN was an actual point source while EGS had a disc of radius 10 microns and thickness 10 microns. (The experiment used a source of 2 mm diameter or less as determined by autoradiography.) The integral backscatter dose was scored in a volume corresponding to the TLD.

Figure 3-1

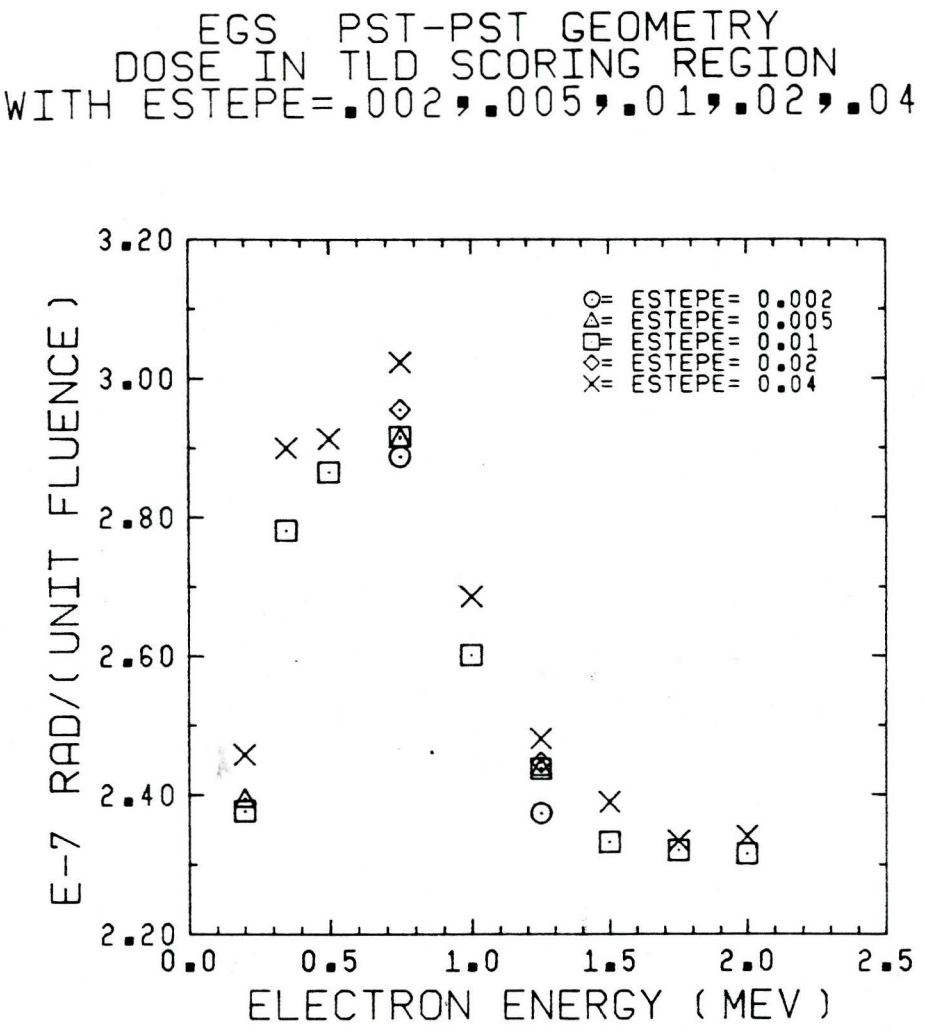

Dose deposited in TLD scoring region with different ESTEPE. Below NOSCAT (defined in text) average over electron point source energy (0.2,2.0) Mev.

ESTEPE	NOSCAT (%)
.002	69±1
.005	46±4
.01	40±2
.02	1
.04	1

Figure 3-2

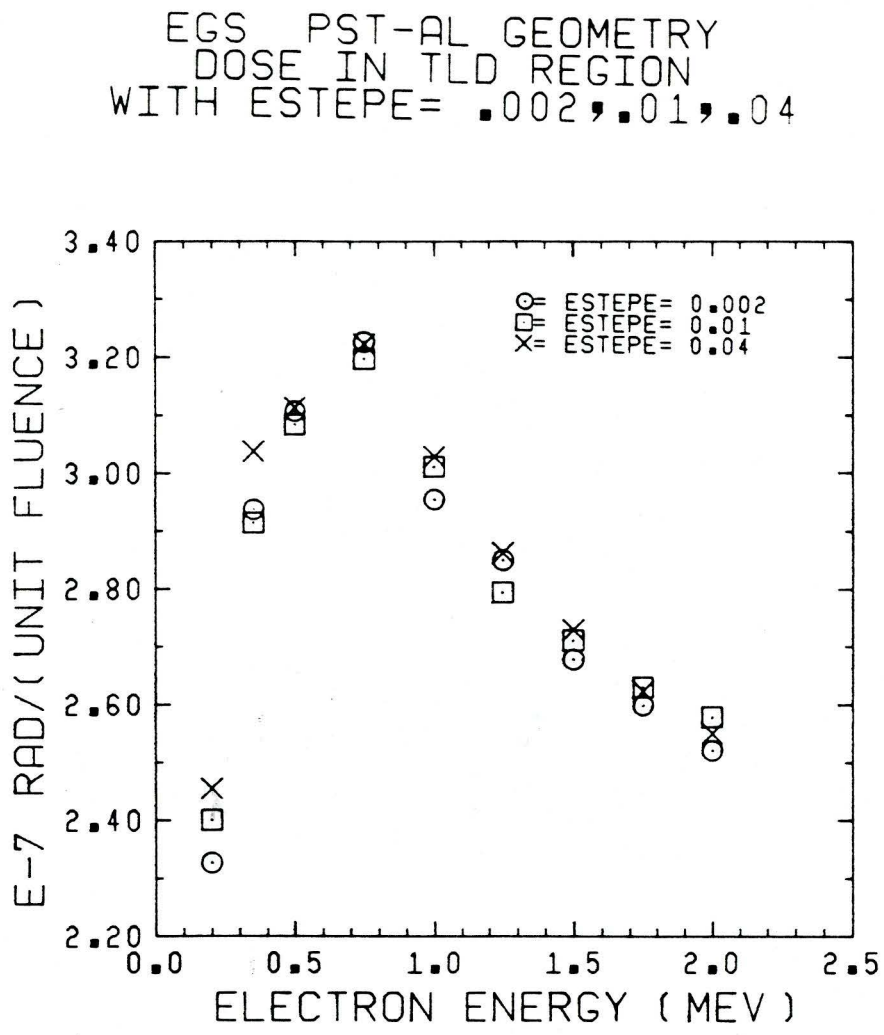

Dose deposited in TLD scoring region with different ESTEPE. Below, NOSCAT (defined in text) average over electron point source energy (0.2, 2.00 MeV)

ESTEPE	NOSCAT (%)
.002	69±4
.01	10±2
.04	1

For light elements ($Z<20$), Cross (1968) has shown that the probability of an electron scattering through an angle θ per unit energy loss ($S(E,\theta)$) is proportional to the scattering media's effective atomic number $\bar{Z}$ where $\bar{Z}$ is given by:

$$\bar{Z} = \frac{\sum N_i Z_i^2}{\sum N_i Z_i}$$

N_i is the relative number of nuclei of charge Z_i. (The summation is taken over all the constituents of the scattering medium.)

Table 3-1 compares the effective atomic numbers of the materials used in this investigation.

Table 3-1.
Comparison of Effective Atomic Numbers.

Material	$\bar{Z}$	Material	$\bar{Z}$
Al	13	PST	5.29
Cortical Bone Plastic	10.52	Red Bone Plastic	5.35
Cortical Bone*	10.50	Red Marrow*	5.93

* Based on data in Woodward (1982)

Electron backscatter increases as the atomic number of the scattering medium increases, therefore there is a larger dose due to the backscattered electrons from the Al-PST interface than the bone-red marrow plastic interface. The dependence of backscatter on atomic number is presented in the literature in several

functional forms. (BA180) (SHA79) (TAB71) (EVE60). Baily (1980) showed that electron backscatter is proportional to ln(Z+1) of the scattering medium and that this relation holds nearly exactly in the range of effective atomic numbers from fat to bone. If this model is followed the increase in electron backscatter dose from aluminum relative to bone plastic would be $\ln(Z_{Al}+1)/\ln(Z_{bone}+1) = 1.14$. The correction to the experimental dose ratio for ^{204}Tl and ^{147}Pm for this effect would be a maximum increase of 0.01, smaller than the experimental error. Even with this correction the Monte Carlo results agree with experiment. (Recall ^{32}P was performed in a planar geometry of Al and PST and is directly comparable to Monte Carlo results.)

A program which generated the beta spectrum for the nuclides used was obtained from W. Prestwich (McMaster University, Hamilton, Ontario.) (PRE85). A copy of this program is found in Appendix A. (Additional information on the analytical form used to generate the beta spectrum can be found in the reference cited.)

PROCEDURE

The variation of dose with electron point source energy was generated for each of the geometrics PST-PST

and PST-Al in a region corresponding to the TLD in the experiment. An analytical fit was made to the Monte Carlo data. Linear segments were used to join the data at low energy (below 0.10 MeV) to define the sharp rise. At energies above this the data were fitted with a function of the form C1 + C2 + Exp(- f(E)*C3) + C4*E where the C's are constants. f(E) is equal to E for EGS dosimeter thickness 12 mg/cm^2 (PST-PST), CYLTRAN dosimeter 31 mg/cm^2 (PST-Al), CYLTRAN dosimeter thickness 12 mg/cm^2 (PST-Al). f(E) is equal to E*E for EGS dosimeter thickness 12 mg/cm^2 (PST-Al), CYLTRAN dosimeter thickness 31 mg/cm^2 (PST-PST) and CYLTRAN dosimeter thickness 12 mg/cm^2 (PST-PST). The fit for EGS dosimeter thickness 31 mg/cm^2 was two linear segments joining the data below 0.2 MeV. At energies above this data were fitted with a fourth order polynomial. These functions are referred to as "dose curves". (A table of the Monte Carlo data to which the dose curves were fitted is given in Appendix C, Tables C-2 through C-5.)

In a given geometry, the dose in the TLD region due to a beta emitting nuclide is determined by integrating the beta spectrum with the "dose curve" for that geometry. For example, the dose to the TLD in the

PST-Al geometry is given by

$$\text{Dose}_{\text{PST-Al}} = \frac{\int S(E)\ \text{Dose}_{\text{PST-Al}}\ (E)\ dE}{\int S(E)\ dE}$$

where S(E) is the beta spectrum.

$\text{Dose}_{\text{PST-Al}}$ (E) is the dose curve in the PST-Al geometry. The dose ratio is given by:

$$\text{Dose Ratio} = \frac{\int S(E)\ \text{Dose}_{\text{PST-Al}}\ (E)dE}{\int S(E)\ \text{Dose}_{\text{PST-PST}}\ (E)dE}$$

where $\text{Dose}_{\text{PST-PST}}(E)$ is the dose curve in the PST-PST geometry.

EGS and CYLTRAN were run on the VAX 8600 at McMaster University . Thirty thousand electron histories were used for monoenergetic point source energies below 0.75 MeV and fifty thousand for energies equal to or above 0.75 MeV.

RESULTS

To show that the beta spectra used are accurate representations of the accepted beta spectra, the average energy calculated from the program is compared to the average energy quoted in ICRP#38(1983).

Table 3-2
Comparison of Average Energy calculated from
Beta spectra program and ICRP#38.

ISOTOPE	ICRP#38 Average Energy (Mev)	BETA SPECTRUM PROGRAM Average Energy (MeV)
^{32}P	0.6947	0.6950
^{204}Tl	0.2439	0.2407
^{147}Pm	0.06196	0.0620

A qualitative comparison is given in Figures 3-3 through 3-5. The beta spectra as generated by the program are compared to the beta spectra from W.G. Cross et al (1983) "Inset". The spectrum of Thallium-204 has a low energy "glitch" due to the shielding correction for the atomic electrons. Cross's spectrum is more accurate in this region. The glitch has an insignificant effect on the results due to the very small contribution to the total dose from electrons in this energy range.

Figures 3-6 through 3-9 are the "dose curves" generated by EGS and CYLTRAN. The symbols correspond to the Monte Carlo data. (The ordinates in the CYLTRAN "dose curves" are on $Me^{V}/_{g}$ per unit fluence deposited in the TLD region. The energy deposited differs from dose by a multiplicative constant (equal to the mass of the TLD region) which cancels in the dose ratio.)

Figure 3-3

BETA SPECTRUM 32 PHOSPHOROUS

Qualitative comparison of beta spectrum generated from computer program compared to beta spectrum from Cross (1983) inset.

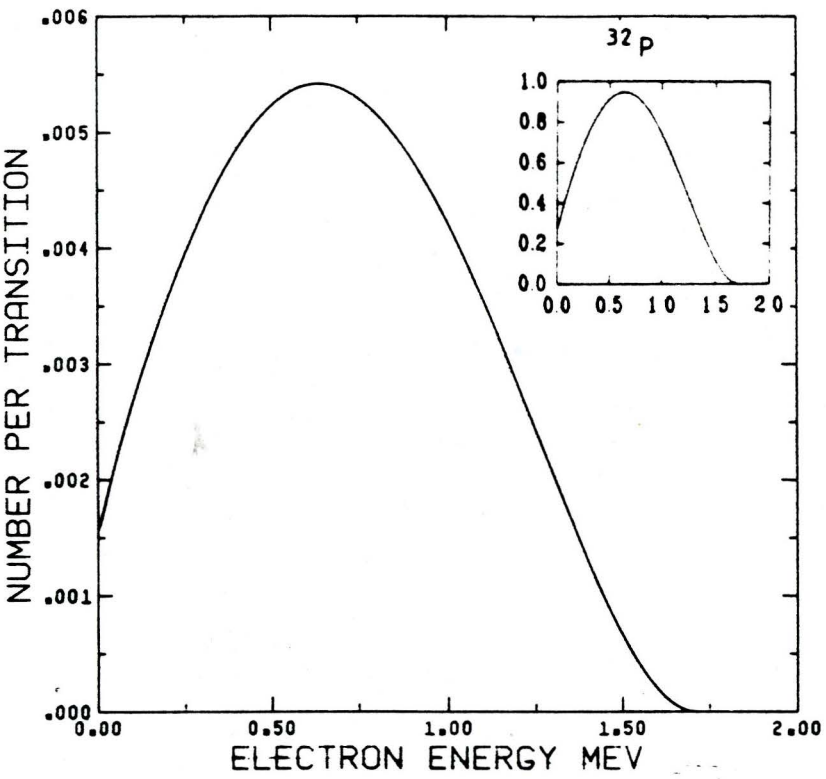

Figure 3-4

BETA SPECTRUM 147 PROMETHIUM

Qualitative comparison of beta spectrum generated from computer program compared to beta spectrum from Cross (1983) inset

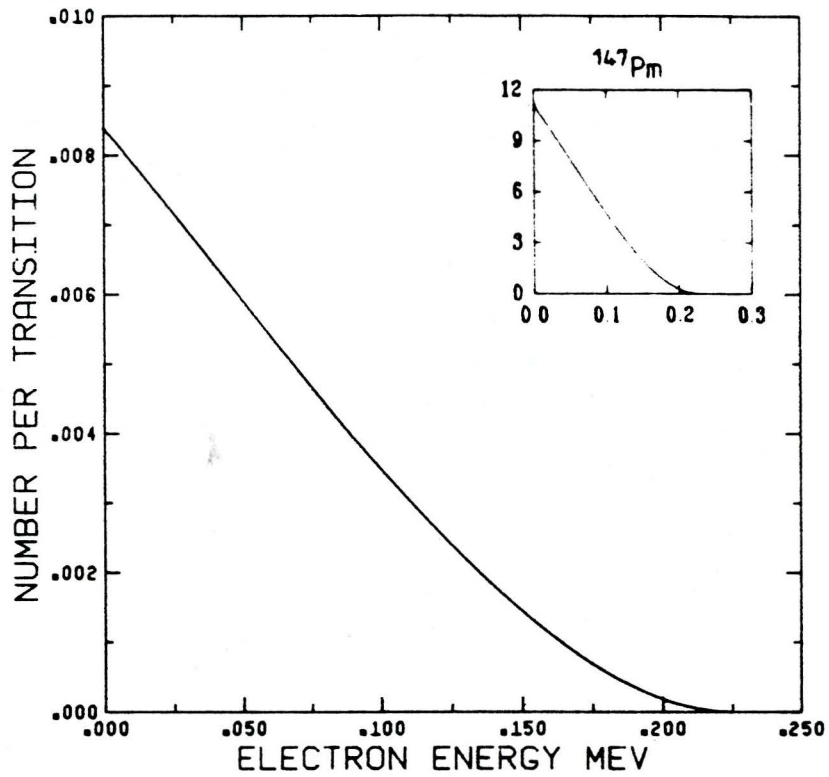

Figure 3-5

BETA SPECTRUM 204 THALLIUM

Qualitative comparison of beta spectrum generated from computer program compared to beta spectrum from Cross (1983) inset.

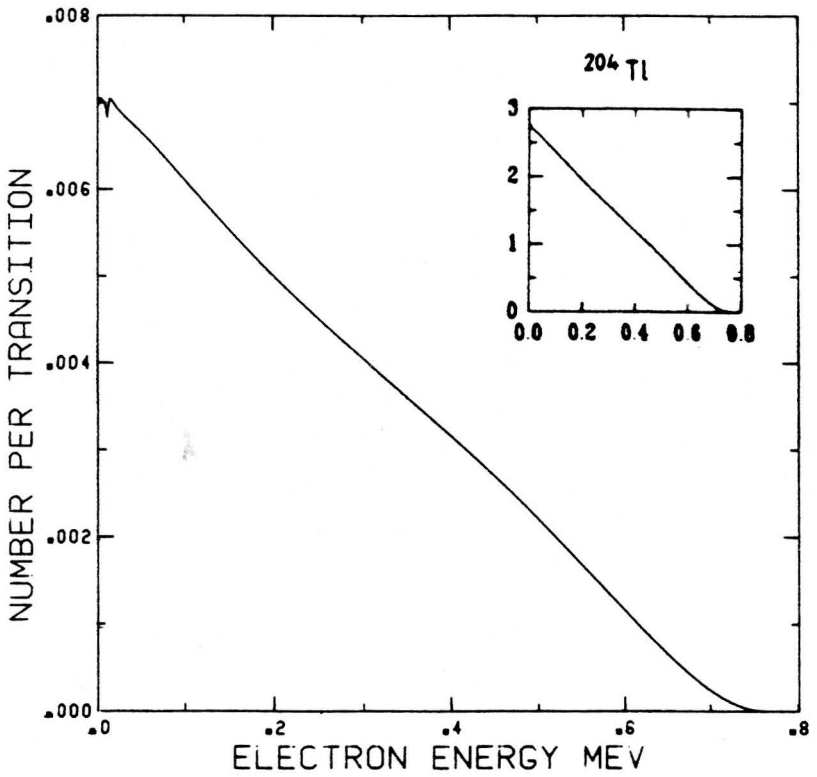

Figure 3-6

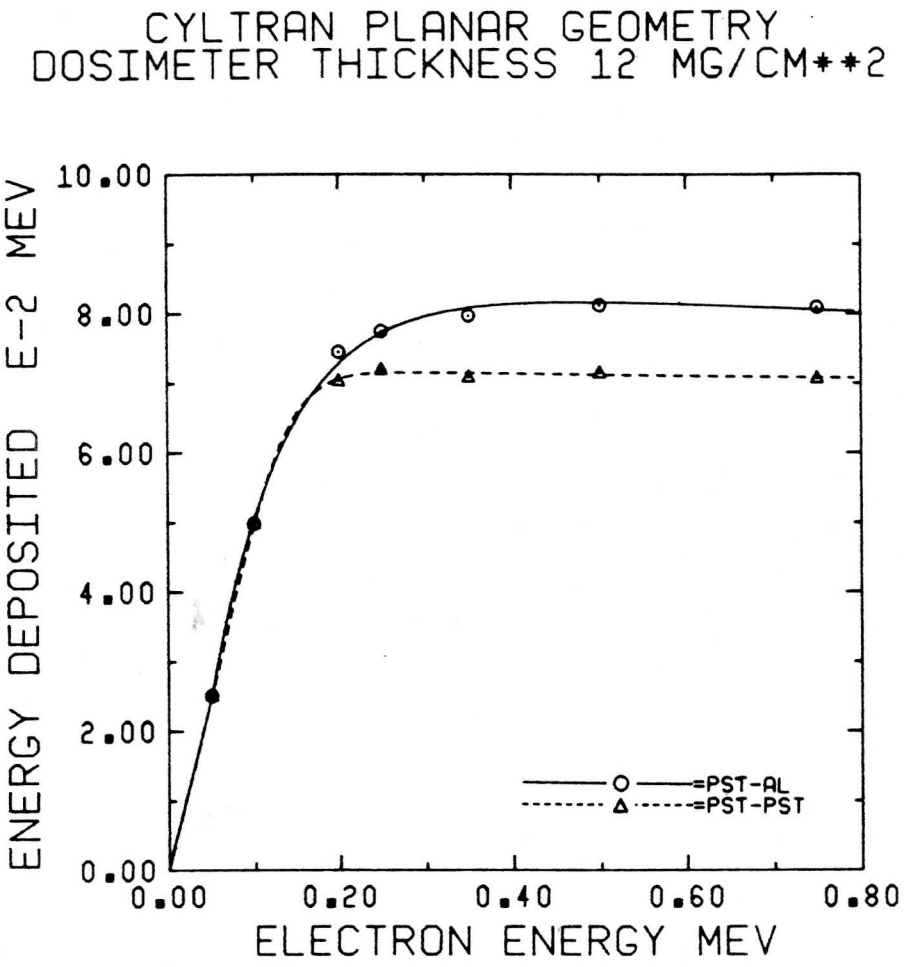

Monoenergetic point source 12 mg/cm^2 from interface. A table of the Monte Carlo values is in Appendix C, Table C-4.

Figure 3-7

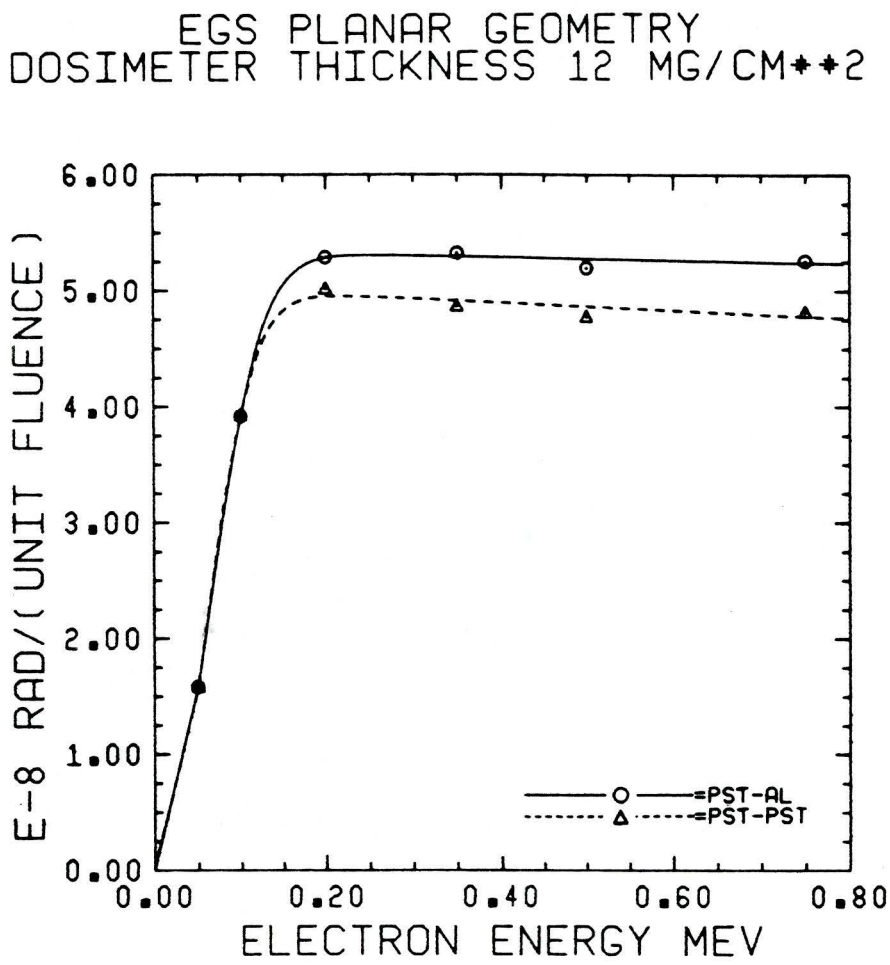

Monoenergetic point source 12 mg/cm^2 from interface. A table of the Monte Carlo values is in Appendix C, Table C-3.

Figure 3-8

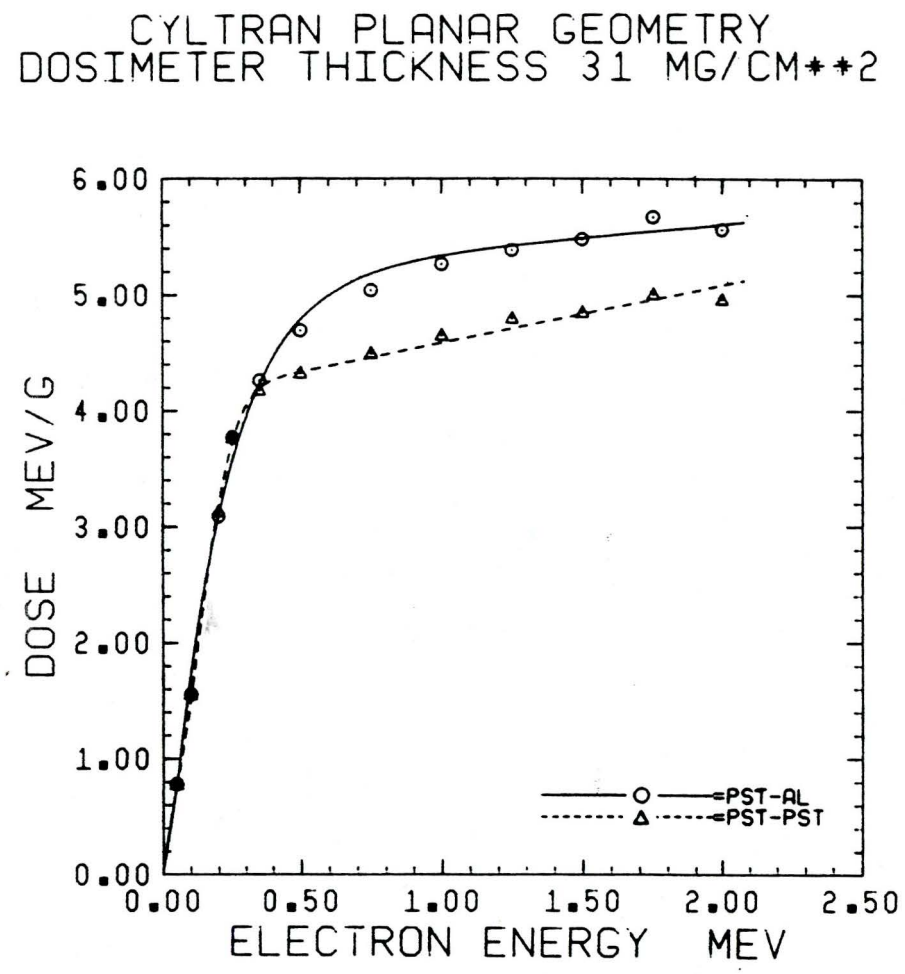

Monoenergetic point source 31 mg/cm^2 from interface. A table of the Monte Carlo values is in Appendix C, Table C-5.

Figure 3-9

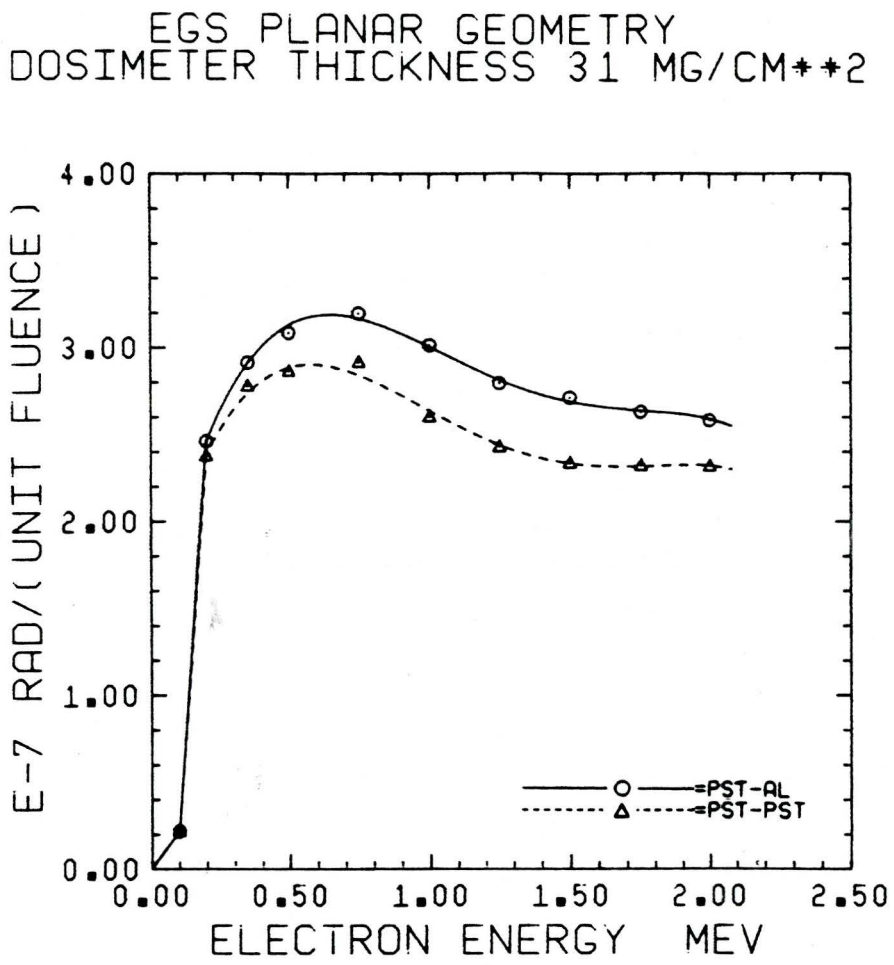

Monoenergetic point source 31 mg/cm^2 from interface. A table of the Monte Carlo values is in Appendix C, Table C-2.

The speed of EGS is dependent upon the ESTEPE and electron energy (longer for smaller ESTEPE and higher electron energies.) CYLTRAN was observed to be faster and the absence of the ESTEPE parameter made it more "user friendly".

The dose curve for the 31 mg/cm^2 thick dosimeter appears to decrease with energy in EGS (Figure 3-9) while with CYLTRAN (Figure 3-8) it appears to rise with energy. This effect may be due to the difference in algorithms used; the dose ratios however do not differ (refer to Table 3-3).

Table 3-3
Comparison of Experimental Dose Ratio with Computer Simulated Dose Ratio from EGS and CYLTRAN.

ISOTOPE	DOSIMETER THICKNESS 12 mg/cm^2 Dose Ratio			DOSIMETER THICKNESS 31 mg/cm^2 Dose Ratio		
	EGS*	CYLTRAN*	EXP'MNT	EGS*	CYLTRAN*	EXP'MNT
32P	-	-	-	1.11 +.02	1.12 +.02	1.12** +.03
204 Tl	1.06 +.02	1.08 +.02	1.08 +.03	1.06 +.02	1.03 +.02	1.06 +.03
147 Pm	1.01 +.02	1.00 +.02	1.03 +.02	-	-	-

* An error of 2% is estimated for the computer simulated dose ratio. This figure is chosen due to the experimental fit of the Monte Carlo data used in its calculation.

** Kwok et al (1985)

The good agreement of the computer simulation with experiment justifies its use for determining the low energy electron dose distribution in dimensions associated with the marrow cavities of trabecular bone.

CHAPTER 4

ELECTRON DOSE DISTRIBUTION IN SPHERICAL GEOMETRY

Having demonstrated the agreement of CYLTRAN with experiment involving low energy electrons and planar interfaces, it is feasible to use the same code to simulate low energy electron transport in the marrow cavities of trabecular bone. A version of CYLTRAN called ACCEPT was used to model the marrow cavity as a polystyrene (PST) sphere surrounded by aluminum. This chapter investigates the dose distribution due to a monoenergetic point source, a point source of beta emitting nuclide and a uniformly distributed monoenergetic electron source within the PST sphere. PST spheres with radii 200 and 500 microns were used.

ACCEPT was used rather than EGS because of the absence of the user supplied ESTEPE parameter and the faster speed (CPU time) of ACCEPT. CYLTRAN and ACCEPT differ in geometric modeling; CYLTRAN has an (axisymmetric) cylindrical material geometry. ACCEPT uses three-dimensional combinatorial geometry (i.e. ACCEPT enables the spherical geometry to be defined).

Both CYLTRAN and ACCEPT are base codes of the Integrated Tiger Series developed at Oak Ridge for the U.S. Department of Energy.

The PST sphere was divided into concentric spherical scoring regions. The dose ratio, as in the preceding chapters, is the dose in a region of the PST sphere bounded by an "infinite" thickness of aluminum (Al-PST geometry) divided by the dose in the same region bounded by an equal thickness of PST (PST-PST geometry). ACCEPT allowed a monoenergetic point source to be placed anywhere inside the sphere. The procedure to determine the dose ratio was to run ACCEPT in the PST-PST and the Al-PST geometry fixing the number of electron histories and energy of the electron source. For a point source with energy above 0.40 MeV fifty thousand electron histories were used. Below 0.40 MeV thirty thousand histories were used. The VAX 8600 at McMaster University was used for running ACCEPT.

The most probable path length across a marrow cavity of the lumbar vertebrae (adult) was estimated to be 275 microns (SPI69) to 690 microns (ECK85b) from the distribution of cavity size presented in the references. For a sphere, under μ-randomness the mean chord length is $^2/_3$ of its diameter (ECK85a). This implies that the most probable diameter of a sphere corresponding to

lumbar marrow cavities is 410 microns to 1040 microns. Spheres with radii 200 and 500 microns were chosen for this reason. (For a uniform distribution of activity within a sphere the mean ray length is $^3/_4$ of the sphere diameter (I-randomness)) (ECK85a).

Figures 4-1 and 4-2 are a cross sectional representation of the spherical geometry used in the transport simulation. The circles inside the outer most circle represent the defined scoring regions. The scoring regions were defined to spatially resolve the variation of the dose ratio inside the sphere. Thinner scoring regions (outer radius minus inner radius = thickness) were defined near the PST-Al interface due to the exponential behaviour of the dose ratio near it (inferred from experimental results with planar interface). The scoring region next to the interface approximates the endosteum lining the marrow cavities. Figure 4-1 is a cross sectional view of the 200 micron (radius) sphere. Figure 4-2 is a cross sectional view of the 500 micron (radius) sphere. Below each diagram is a table indicating the volume and mass of each scoring region.

Note that the scoring regions are spherical

Figure 4-1: Cross section of 200 micron sphere.

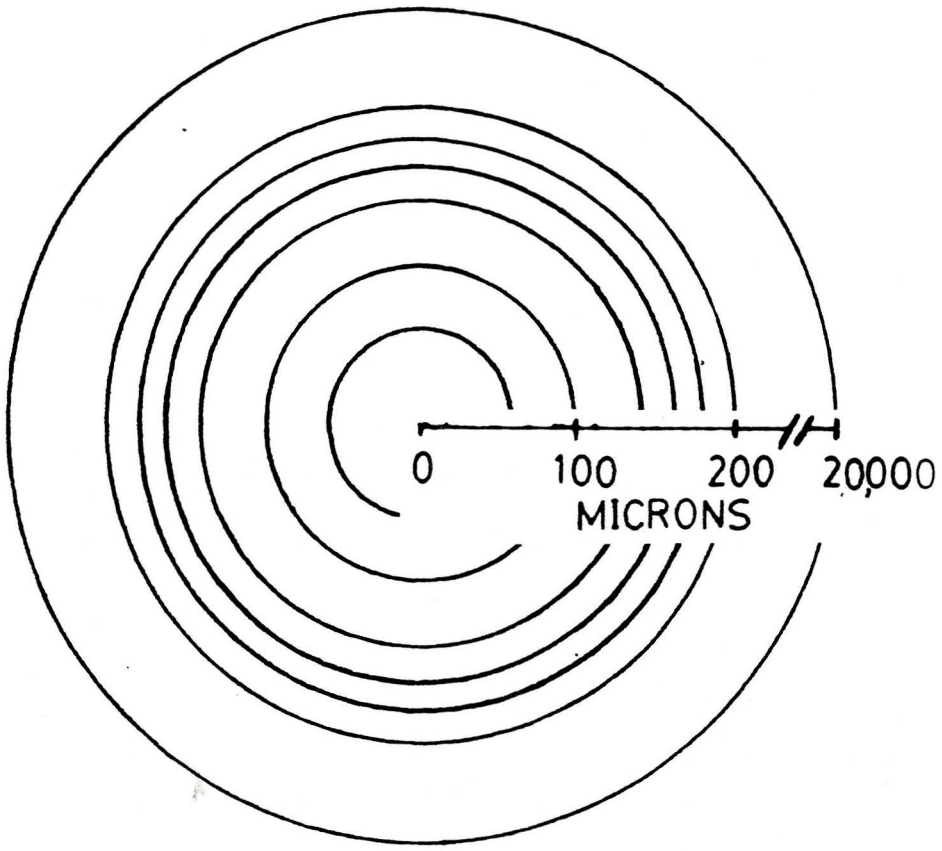

Cross sectional view of 200 micron radius sphere showing scoring regions. The table below indicates volume and mass of scoring regions.

Scoring Region Shell radii (inner - outer) Microns	Volume $X\ 10^{-6} cm^3$	Mass $x\ 10^{-6} g$
0-60	0.90	0.94
60-100	3.28	3.41
100-140	7.30	7.59
140-160	5.66	5.88
160-180	7.27	7.56
180-200	9.08	9.44

Figure 4-2: Cross section of 500 micron sphere.

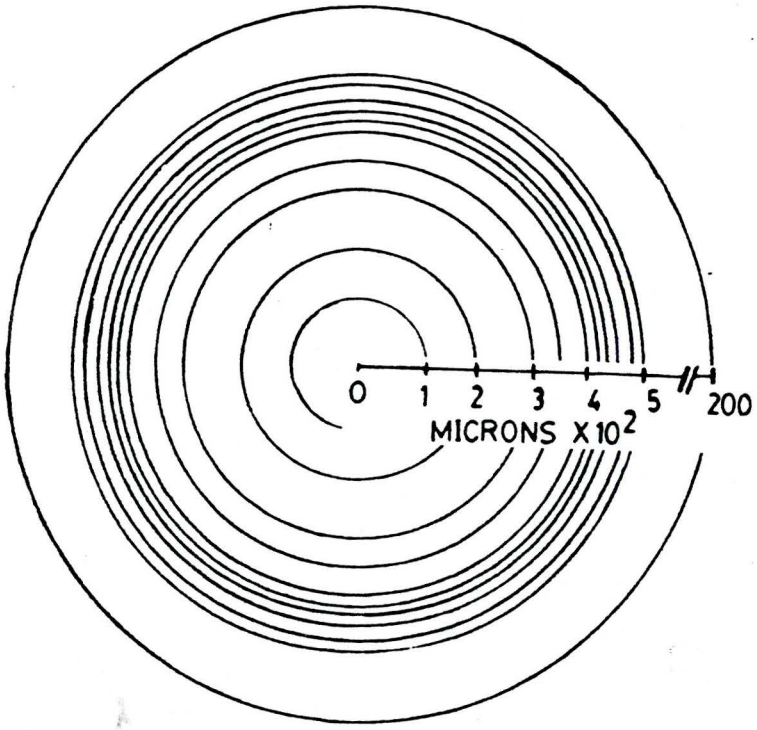

Cross sectional view of 500 micron radius sphere showing scoring regions. The table below indicates volume and mass of scoring regions.

Scoring Region Shell radii (inner-outer) microns	Volume $\times 10^{-6}$ cm^3	Mass $\times 10^{-6}$ g
0-100	4.18	4.35
100-200	29.32	30.49
200-300	79.58	82.77
300-350	66.49	69.15
350-400	88.48	92.03
400-420	42.25	43.94
420-440	46.47	48.34
440-460	50.90	52.94
460-480	55.53	57.74
480-500	60.35	62.77

shells. Graphs for individual scoring regions will have their inner and outer radii quoted. For example, the graph titled "ACCEPT Sphere Radius = 500 microns, Shell Radii = 350-400 microns" would imply that the graph depicts data from the scoring region of inner radii 350 microns and outer radii of 400 microns in the PST sphere with radius 500 microns.

The following Figures 4-3 through 4-18 show the energy deposited and monoenergetic dose ratio in different scoring regions due to a monoenergetic point source of electrons located at the center of the sphere. The first six Figures are for the PST sphere of radius 200 microns; the next ten are for the sphere with radius 500 microns.

The upper graph of each of these Figures is the energy deposited in the identified scoring region as a function of electron energy. The symbols correspond to the Monte Carlo data obtained from ACCEPT. The error bars are too small to be drawn, statistical errors in the Monte Carlo data are within 1%.

The lower graph of each Figure is the monoenergetic dose ratio versus electron energy. The monoenergetic dose ratio is the ratio of the Monte Carlo values from the upper Figure (the energy deposited in the PST-Al geometry divided by the energy deposited in the PST-PST geometry). The error bars correspond to one standard deviation of the mean.

The continuous and dashed lines in the upper graph are fits to the Monte Carlo data. Linear segments were

used to connect the data at low energy defining the sharp peak, at energies above the peak region. The data was fit with a function of the form C1 + C2 * EXP (-E*C3) (where the C's are constants).

The fit was used to perform an integration with the beta energy spectrum of a nuclide. This was used to determine the dose ratio in the sphere due to a point source of the nuclide located at the center of the sphere. (The procedure for calculating this ratio is described in Chapter 3). The results of this integration with isotopes ^{204}Tl, ^{32}P and ^{147}Pm are found in Figures 4-19 and 4-20 for the 200 and 500 micron sphere respectively.

The upper graphs in Figures 4-9 through 4-18 for the 500 micron sphere depicts energy deposited up to an electron energy of 1.0 MeV. To extend the data to include the endpoint energy of ^{32}P (1.71 MeV) the dose in each geometry at 1.0 MeV is averaged and assumed constant from 1.0 to 1.71 MeV. Negligible variation of the energy deposited with electron source energy was observed for the 200 micron sphere in this same energy range.

Figure 4-3

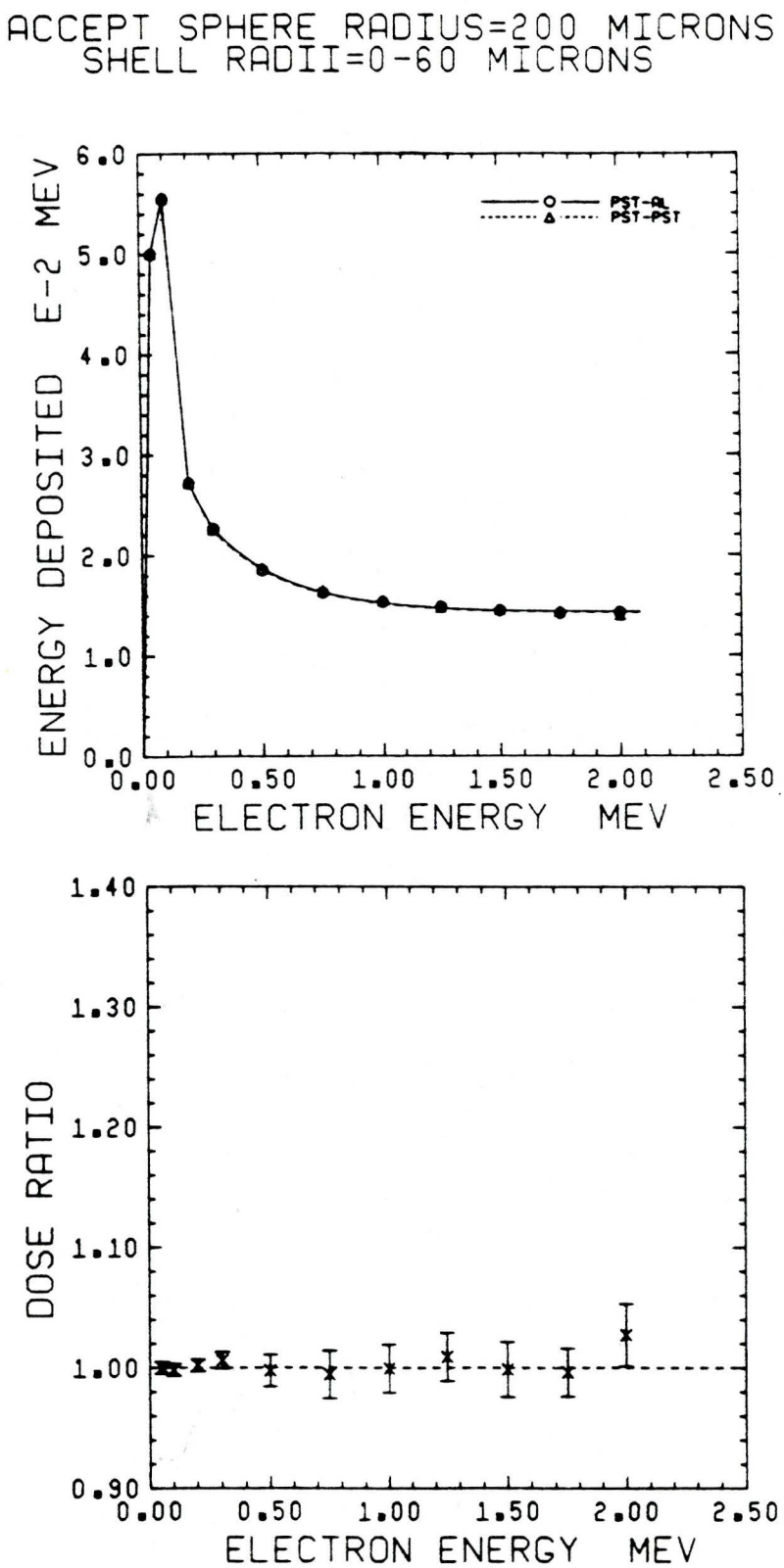
ACCEPT SPHERE RADIUS=200 MICRONS
SHELL RADII=0-60 MICRONS
ENERGY DEPOSITED E-2 MEV
6.0
5.0
4.0
3.0
2.0
1.0
0.0
PST-RL
PST-PST
0.00
0.50
1.00
1.50
2.00
2.50
ELECTRON ENERGY MEV
DOSE RATIO
1.40
1.30
1.20
1.10
1.00
0.90
0.00
0.50
1.00
1.50
2.00
2.50
ELECTRON ENERGY MEV

Figure 4-4

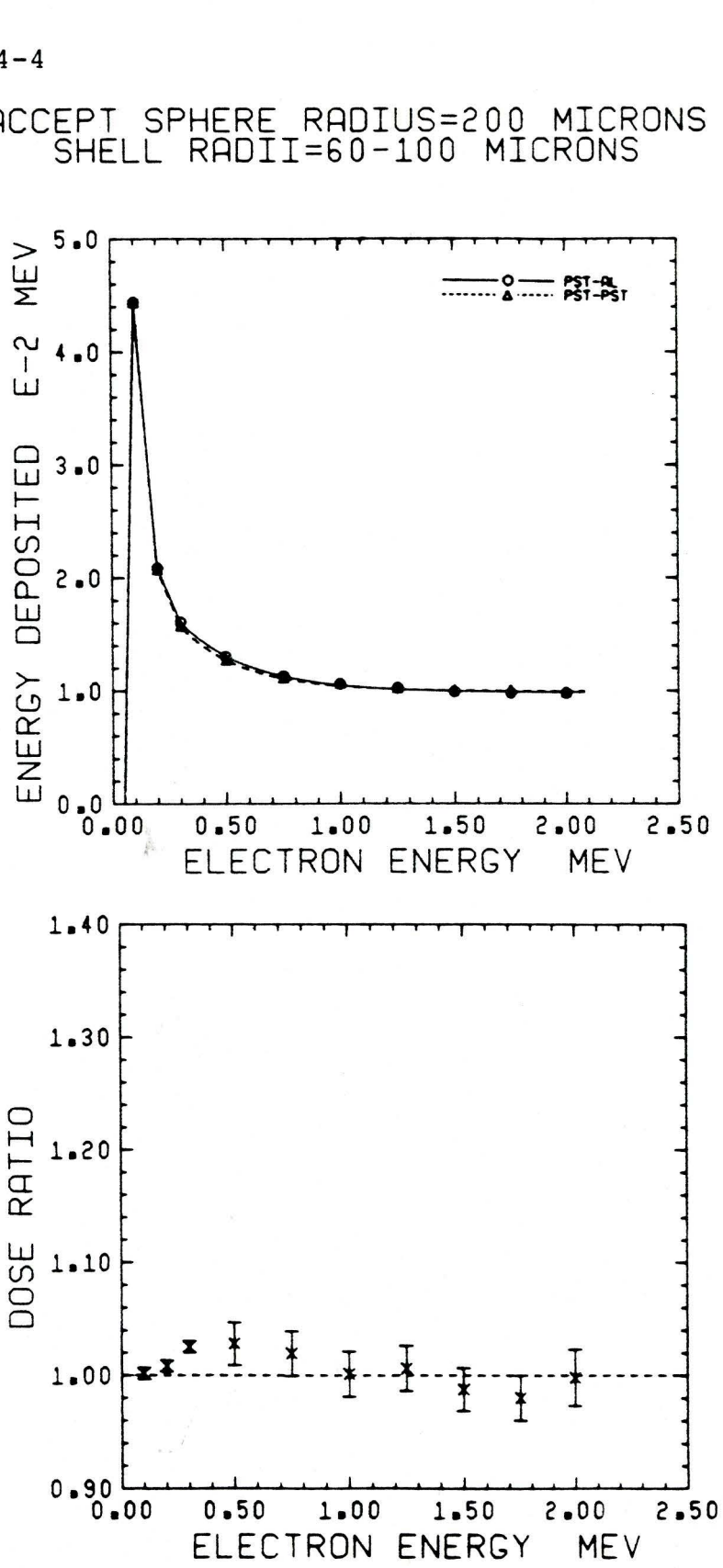
ACCEPT SPHERE RADIUS=200 MICRONS
SHELL RADII=60-100 MICRONS
ENERGY DEPOSITED E-2 MEV
5.0
4.0
3.0
2.0
1.0
0.0
PST-PL
PST-PST
0.00
0.50
1.00
1.50
2.00
2.50
ELECTRON ENERGY MEV
DOSE RATIO
1.40
1.30
1.20
1.10
1.00
0.90
0.00
0.50
1.00
1.50
2.00
2.50
ELECTRON ENERGY MEV

Figure 4-5

ACCEPT SPHERE RADIUS=200 MICRONS
SHELL RADII=100-140 MICRONS

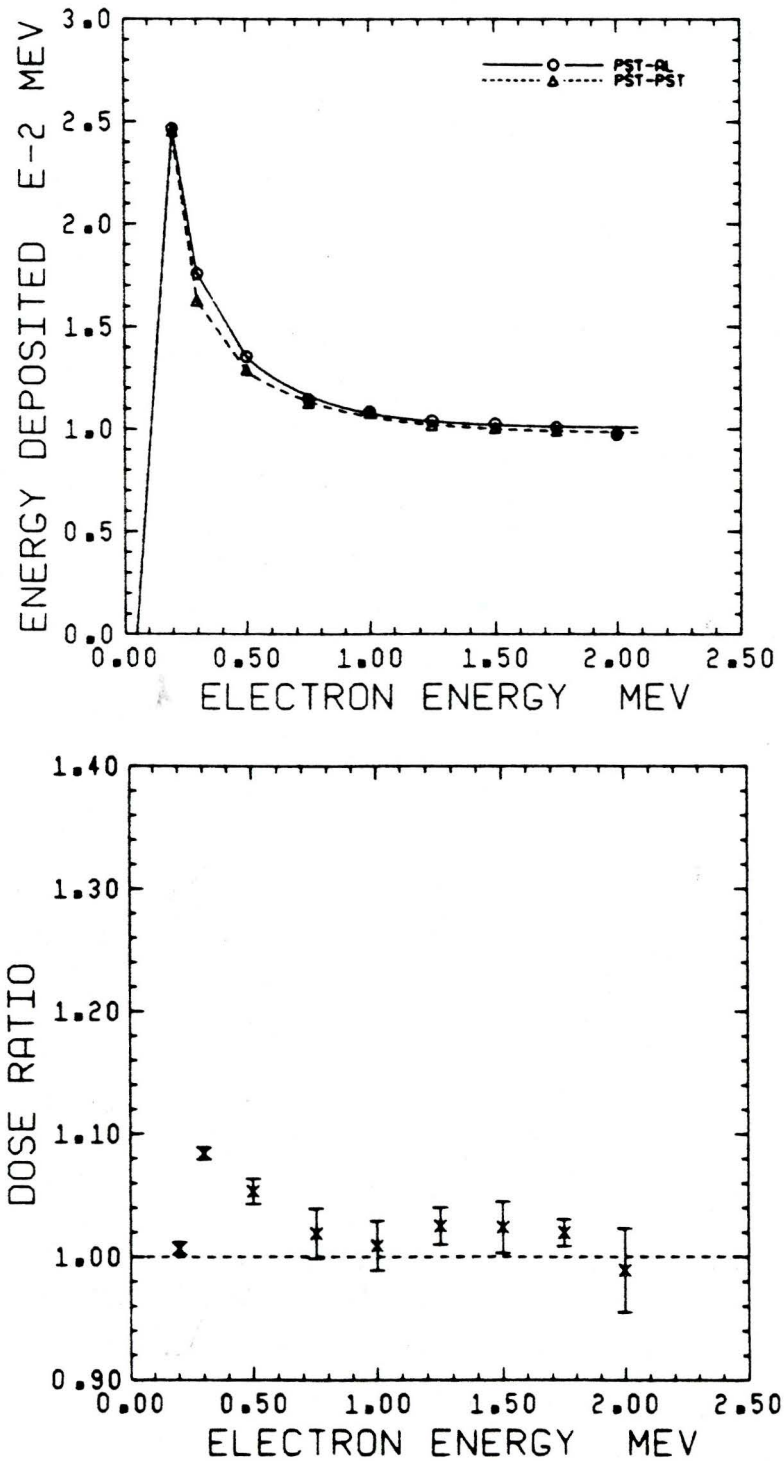

Figure 4-6

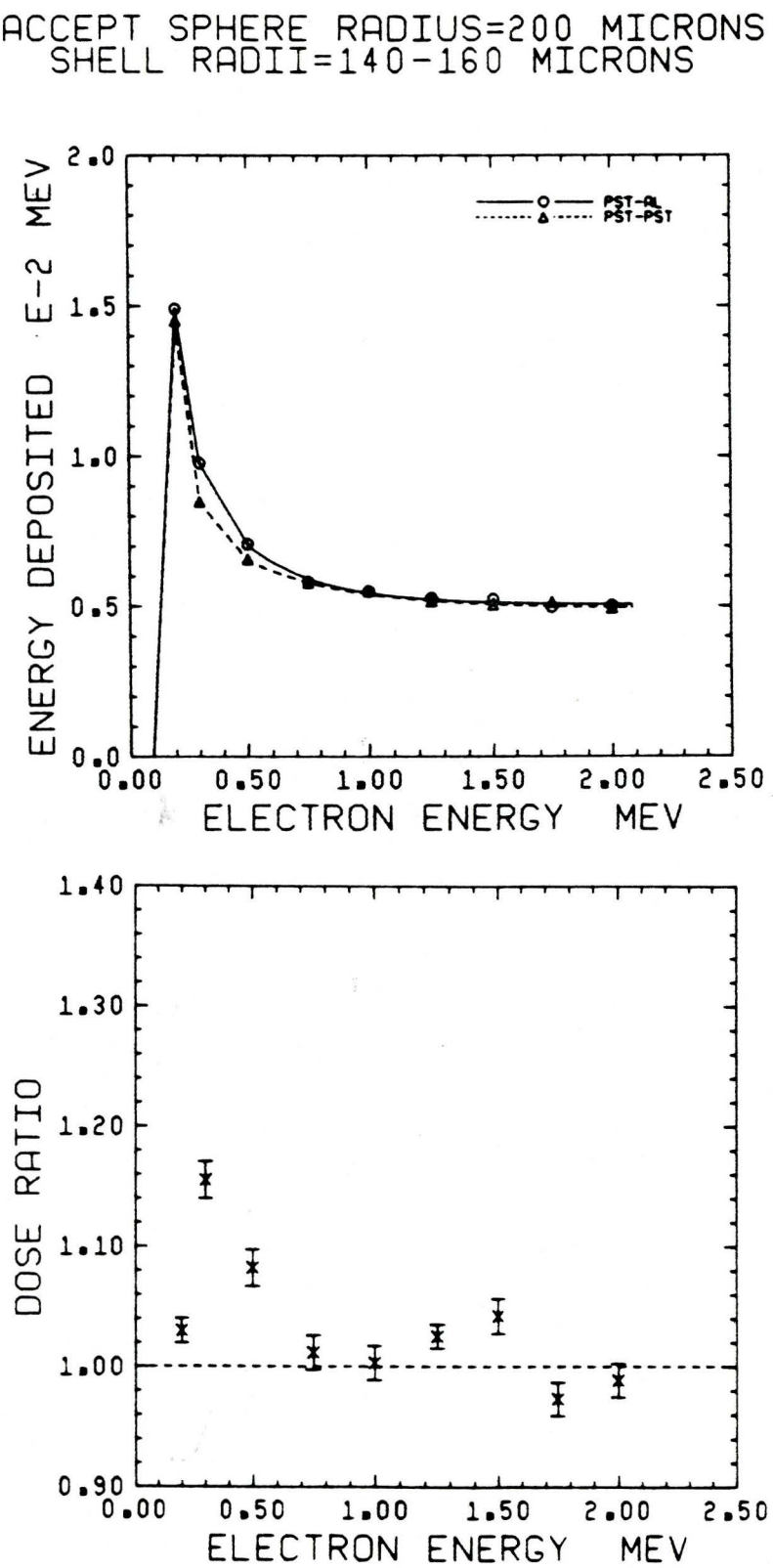
ACCEPT SPHERE RADIUS=200 MICRONS
SHELL RADII=140-160 MICRONS
ENERGY DEPOSITED E-2 MEV
2.0
1.5
1.0
0.5
0.0
PST-PL
PST-PST
0.00
0.50
1.00
1.50
2.00
2.50
ELECTRON ENERGY MEV
DOSE RATIO
1.40
1.30
1.20
1.10
1.00
0.90
0.00
0.50
1.00
1.50
2.00
2.50
ELECTRON ENERGY MEV

Figure 4-7

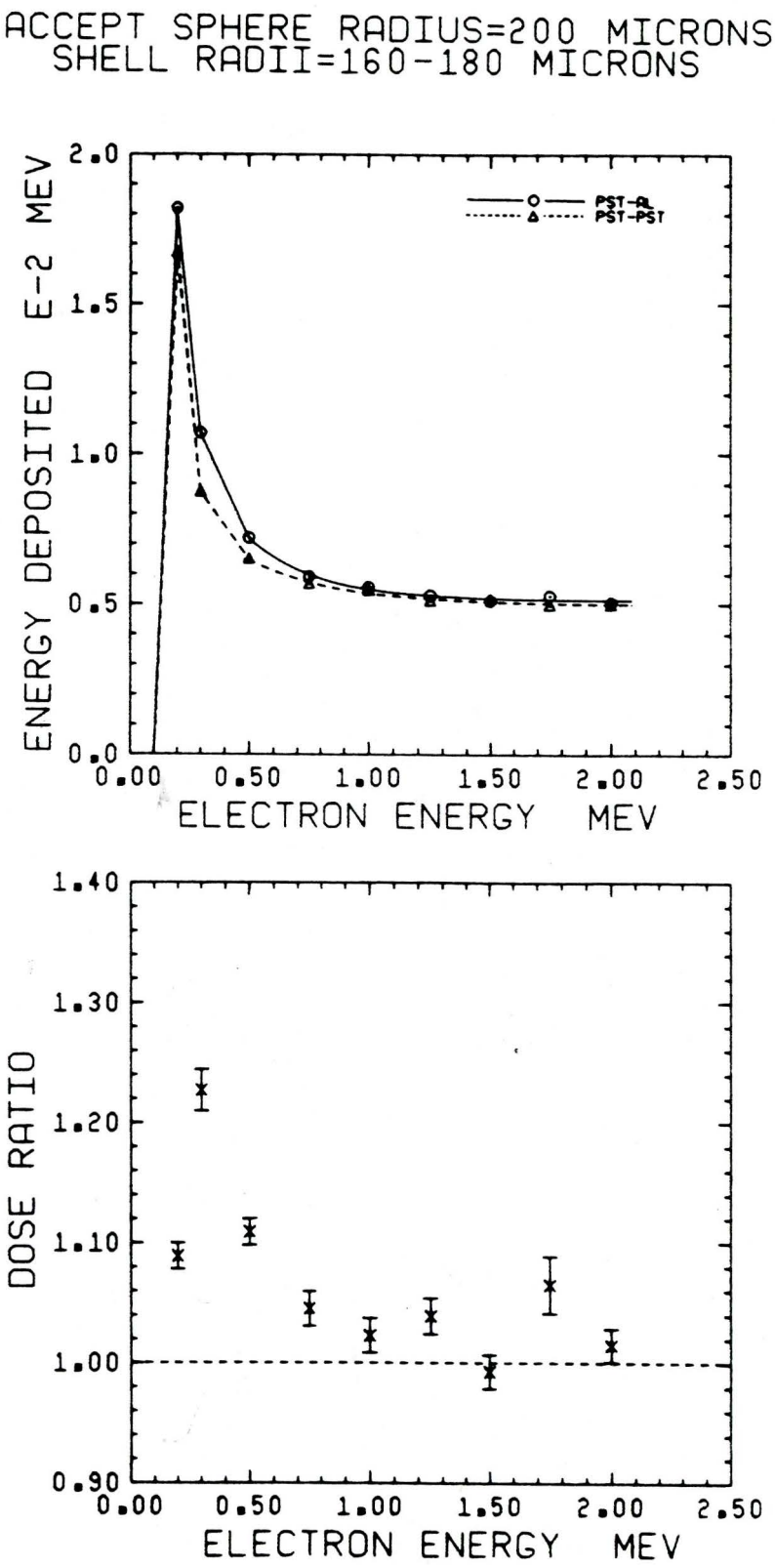
ACCEPT SPHERE RADIUS=200 MICRONS
SHELL RADII=160-180 MICRONS
ENERGY DEPOSITED E-2 MEV
2.0
1.5
1.0
0.5
0.0
PST-AL
PST-PST
0.00
0.50
1.00
1.50
2.00
2.50
ELECTRON ENERGY MEV
DOSE RATIO
1.40
1.30
1.20
1.10
1.00
0.90
0.00
0.50
1.00
1.50
2.00
2.50
ELECTRON ENERGY MEV

Figure 4-8

ACCEPT SPHERE RADIUS=200 MICRONS
SHELL RADII=180-200 MICRONS
Table of Values in Appendix C, Table C-6

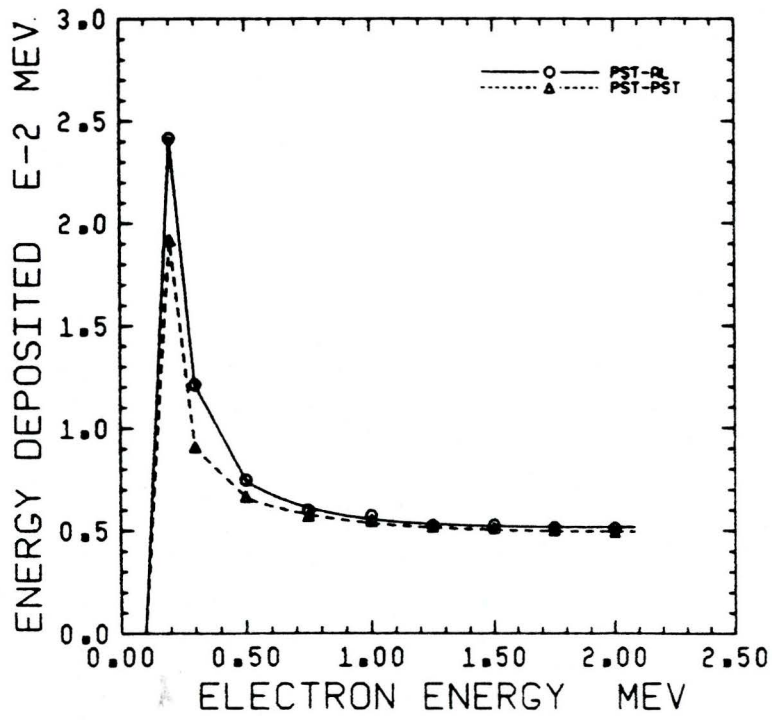

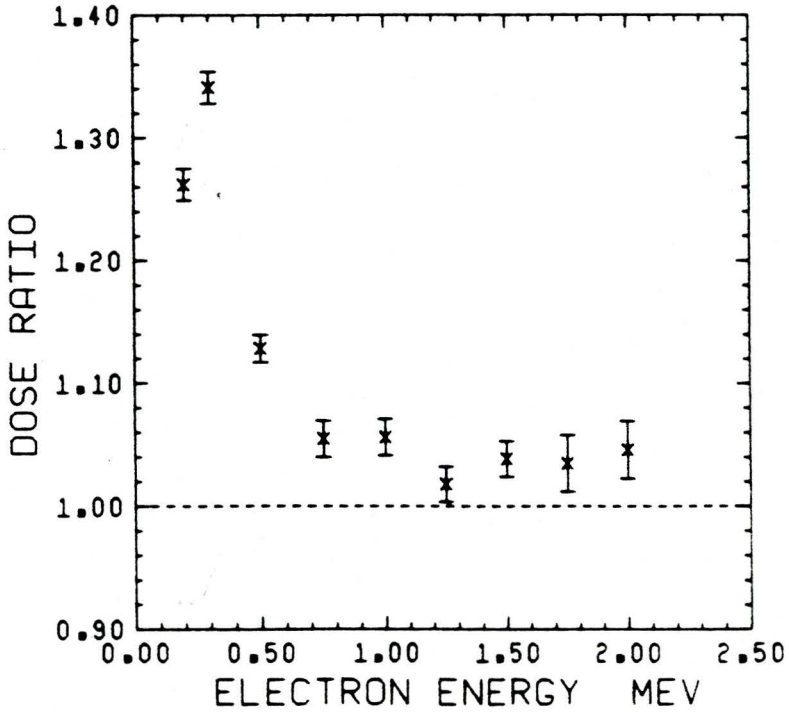

Figure 4-9

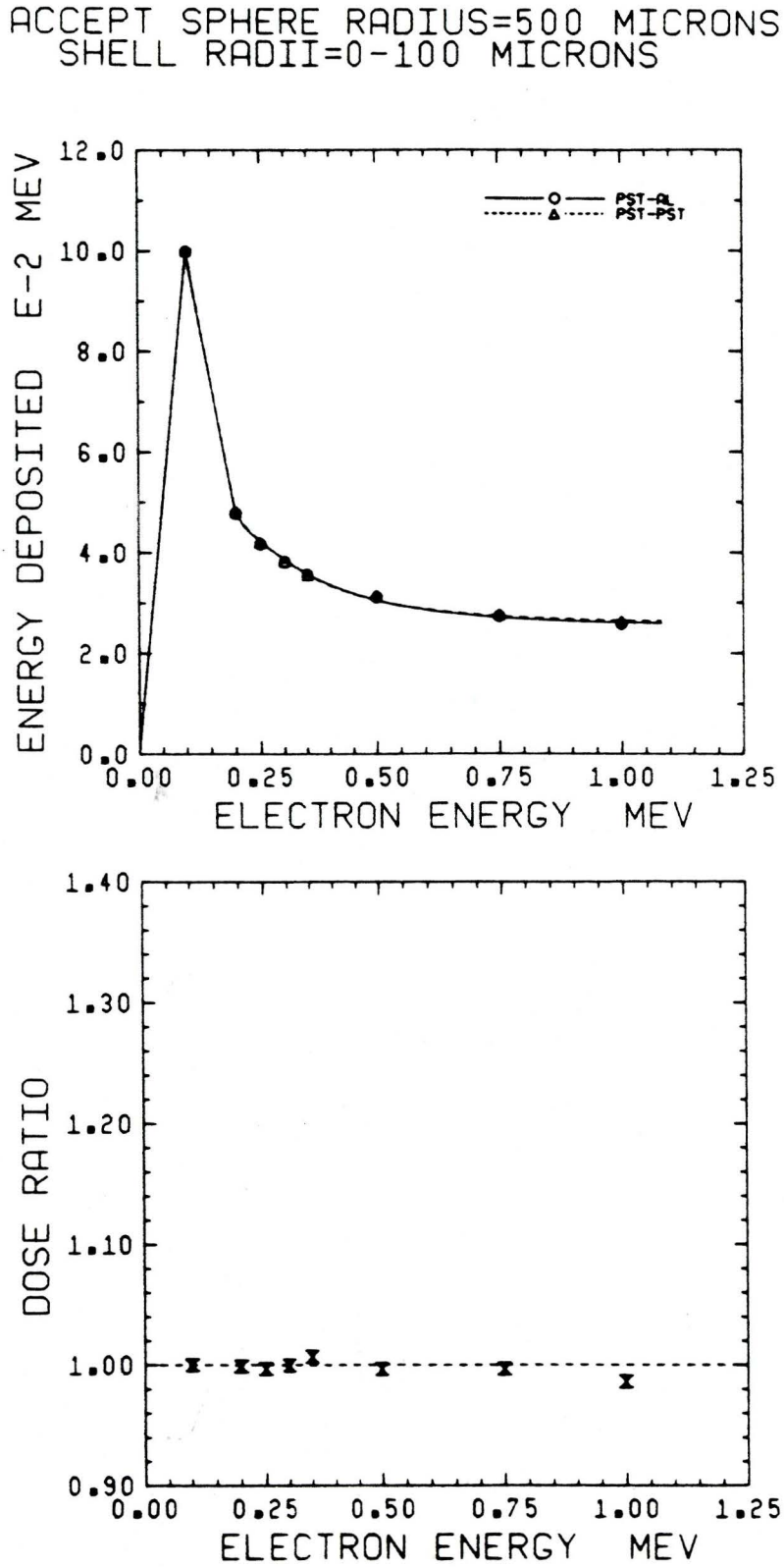
ACCEPT SPHERE RADIUS=500 MICRONS
SHELL RADII=0-100 MICRONS
ENERGY DEPOSITED E-2 MEV
12.0
10.0
8.0
6.0
4.0
2.0
0.0
PST-GL
PST-PST
0.00
0.25
0.50
0.75
1.00
1.25
ELECTRON ENERGY MEV
DOSE RATIO
1.40
1.30
1.20
1.10
1.00
0.90
0.00
0.25
0.50
0.75
1.00
1.25
ELECTRON ENERGY MEV

Figure 4-10

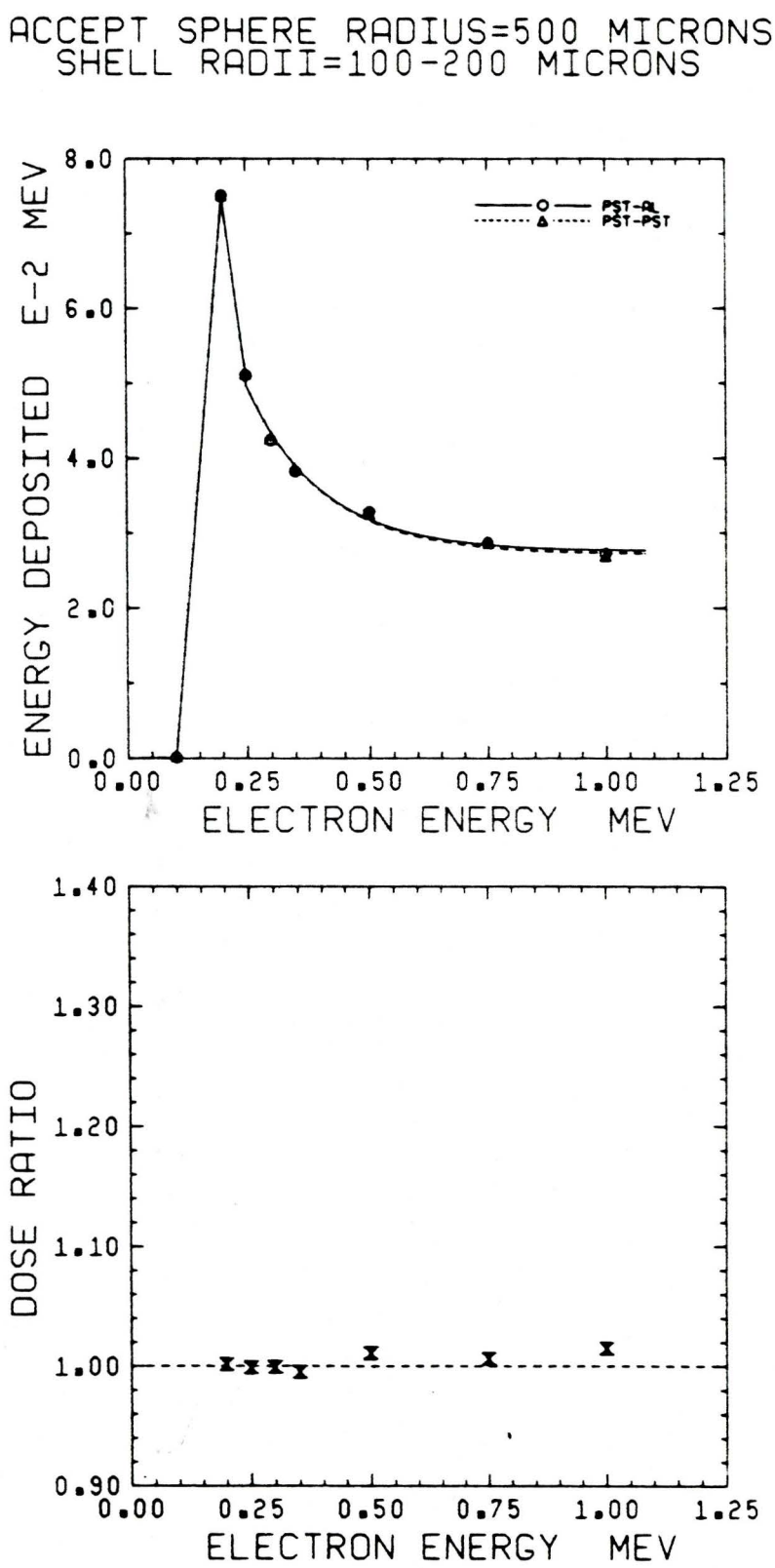
ACCEPT SPHERE RADIUS=500 MICRONS
SHELL RADII=100-200 MICRONS
ENERGY DEPOSITED E-2 MEV
8.0
6.0
4.0
2.0
0.0
PST-GL
PST-PST
0.00
0.25
0.50
0.75
1.00
1.25
ELECTRON ENERGY MEV
DOSE RATIO
1.40
1.30
1.20
1.10
1.00
0.90
0.00
0.25
0.50
0.75
1.00
1.25
ELECTRON ENERGY MEV

Figure 4-11

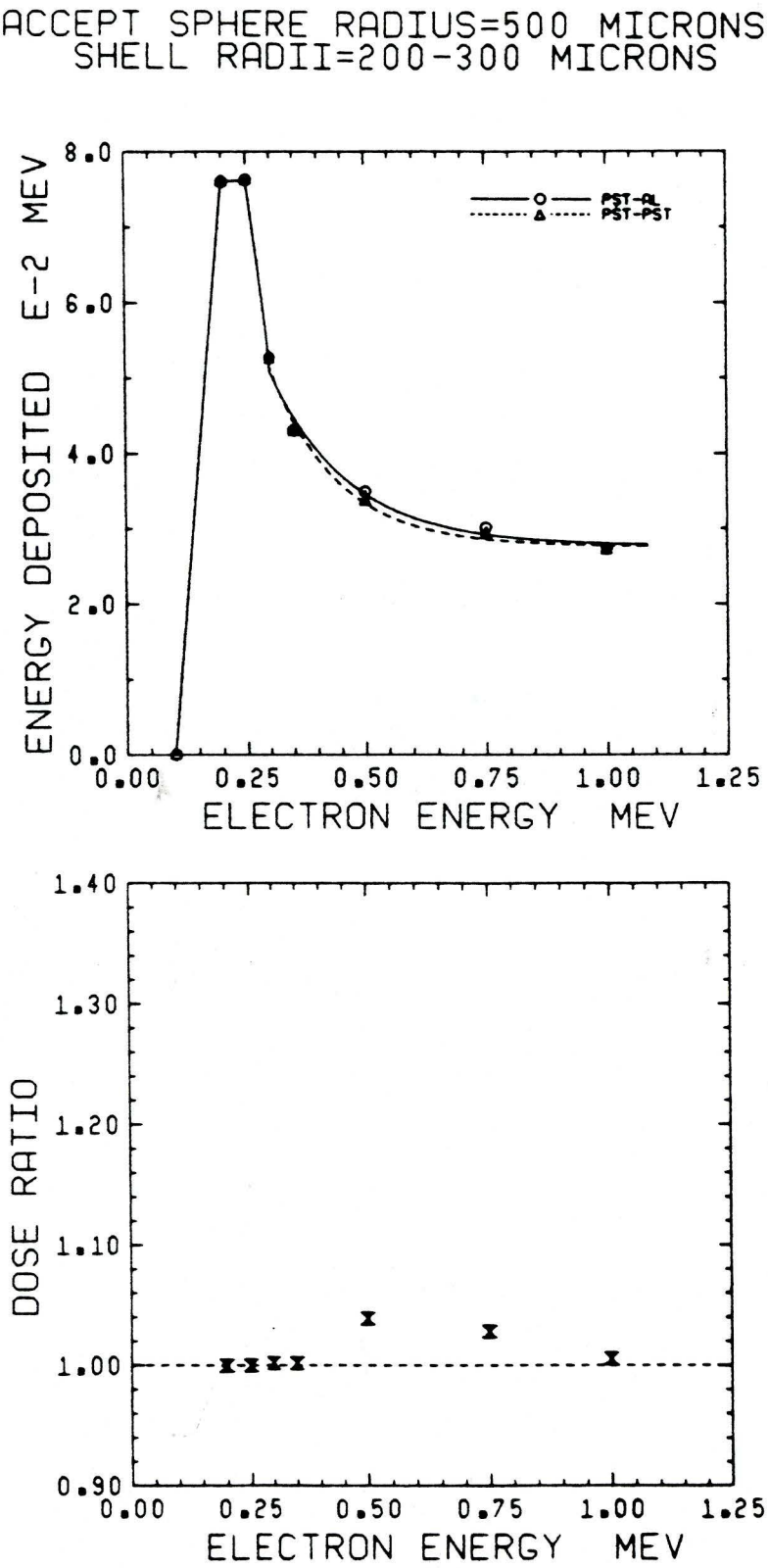
ACCEPT SPHERE RADIUS=500 MICRONS
SHELL RADII=200-300 MICRONS
ENERGY DEPOSITED E-2 MEV
8.0
6.0
4.0
2.0
0.0
PST-GL
PST-PST
0.00
0.25
0.50
0.75
1.00
1.25
ELECTRON ENERGY MEV
DOSE RATIO
1.40
1.30
1.20
1.10
1.00
0.90
0.00
0.25
0.50
0.75
1.00
1.25
ELECTRON ENERGY MEV

Figure 4-12

ACCEPT SPHERE RADIUS=500 MICRONS
SHELL RADII=300-350 MICRONS

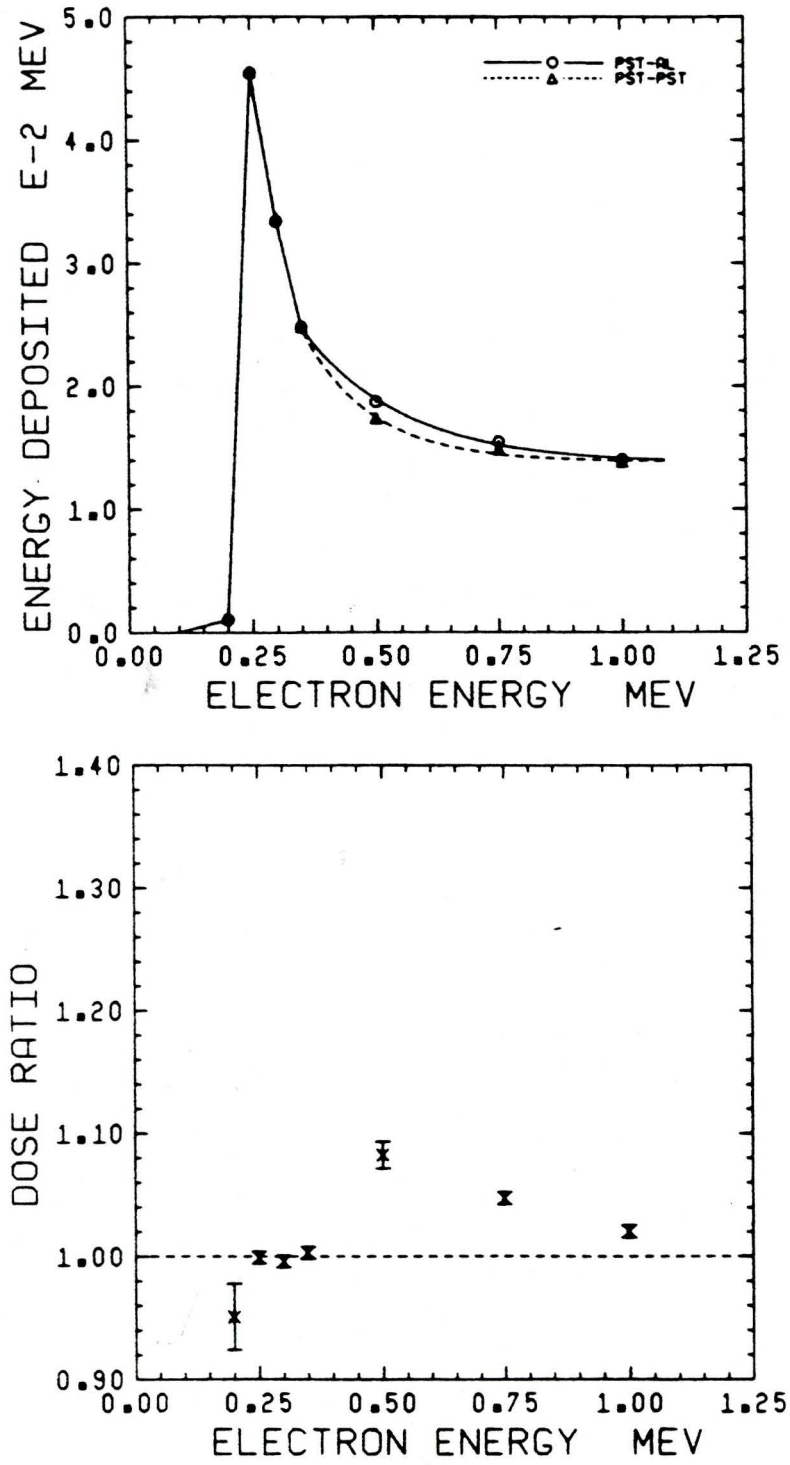

Figure 4-13

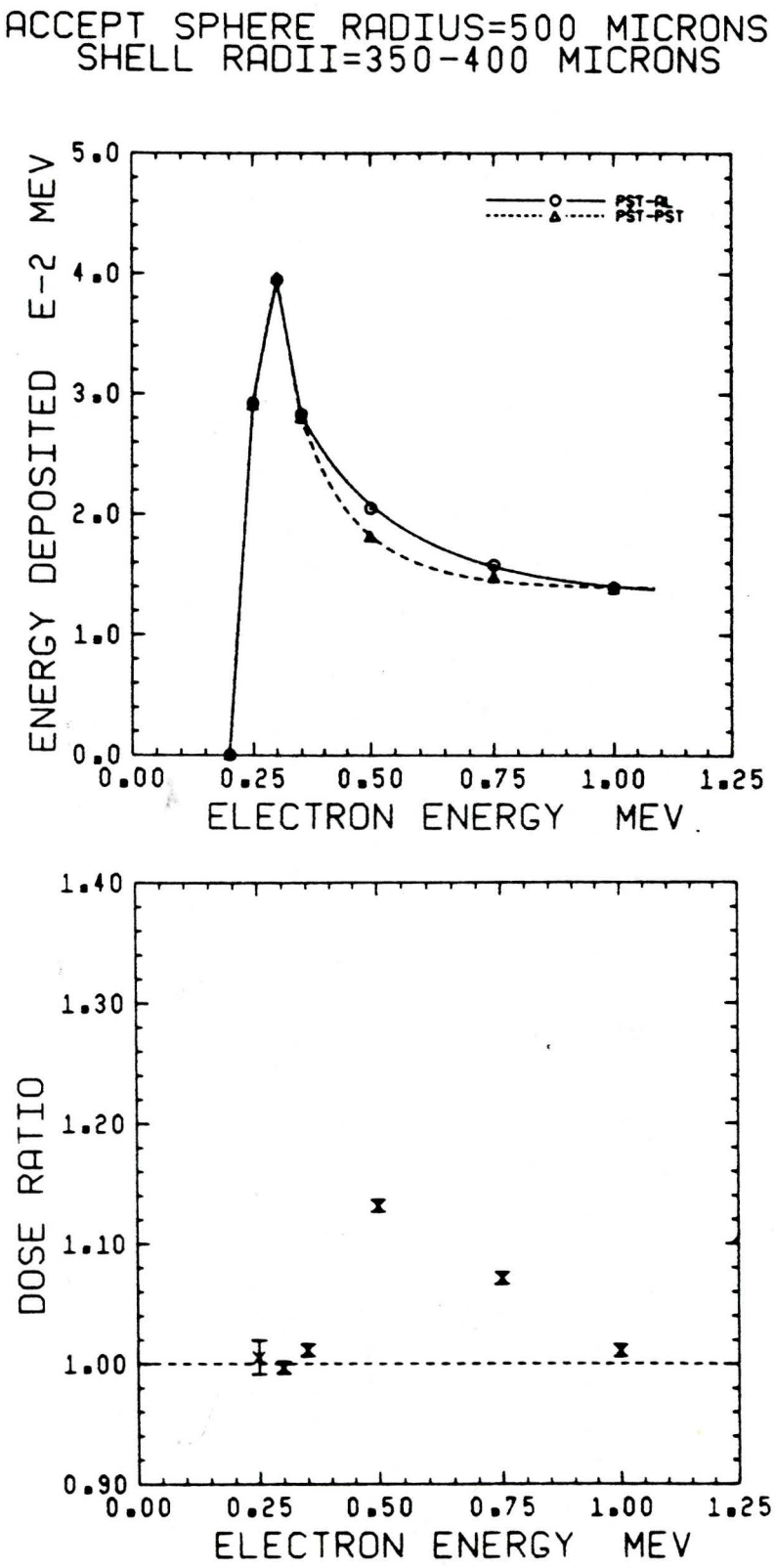
ACCEPT SPHERE RADIUS=500 MICRONS
SHELL RADII=350-400 MICRONS
ENERGY DEPOSITED E-2 MEV
5.0
4.0
3.0
2.0
1.0
0.0
PST-PST
0.00
0.25
0.50
0.75
1.00
1.25
ELECTRON ENERGY MEV
DOSE RATIO
1.40
1.30
1.20
1.10
1.00
0.90
ELECTRON ENERGY MEV

Figure 4-14

ACCEPT SPHERE RADIUS=500 MICRONS
SHELL RADII=400-420 MICRONS

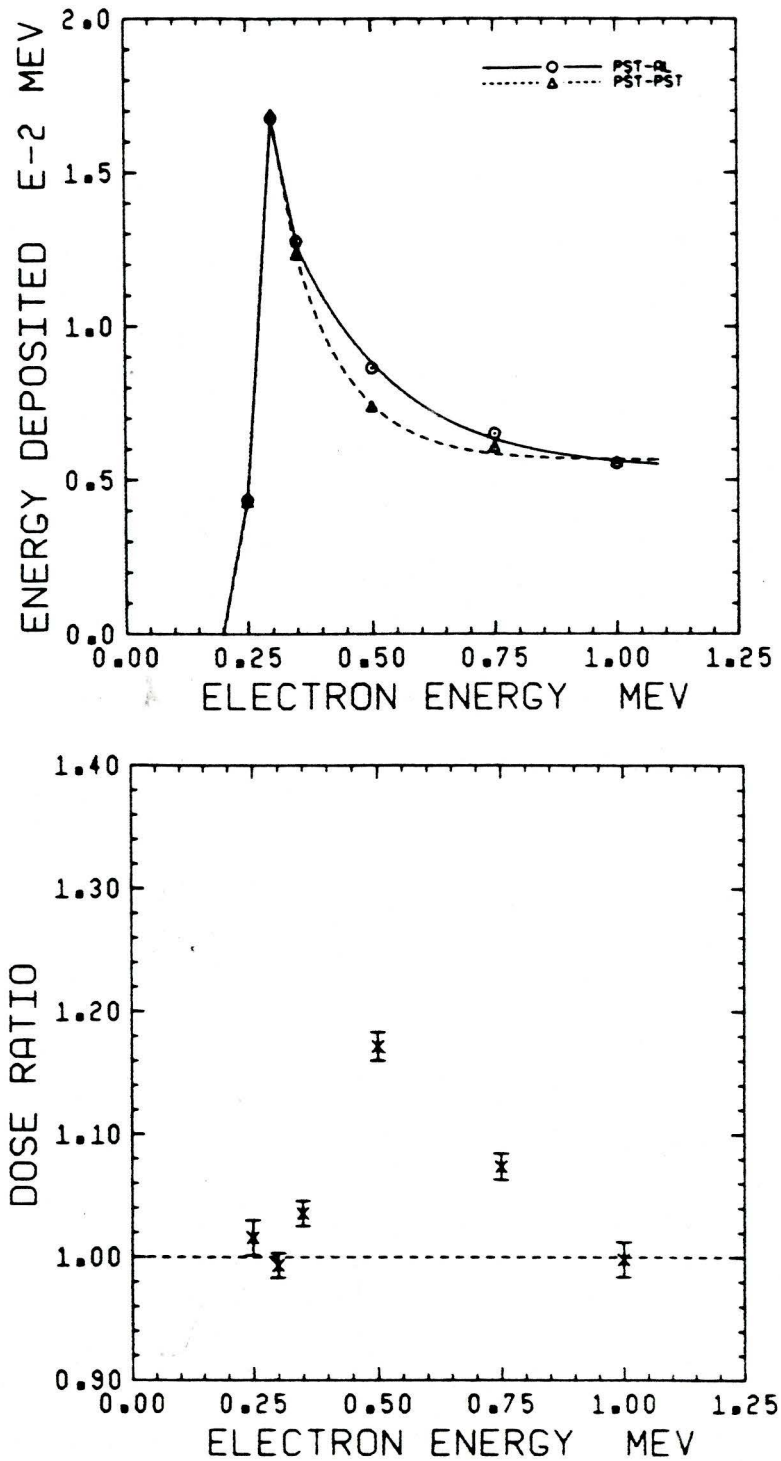

Figure 4-15

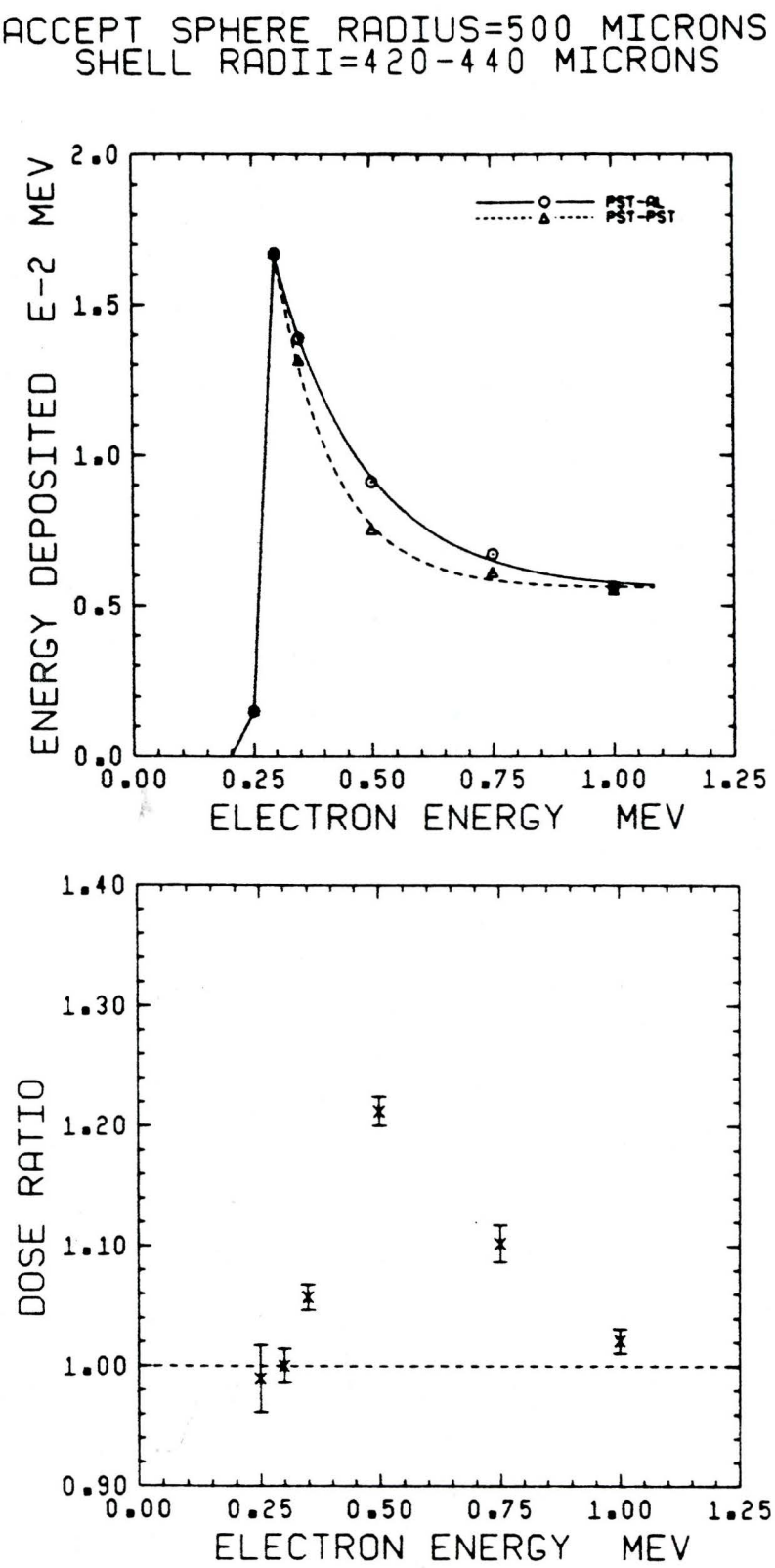
ACCEPT SPHERE RADIUS=500 MICRONS
SHELL RADII=420-440 MICRONS
ENERGY DEPOSITED E-2 MEV
2.0
1.5
1.0
0.5
0.0
0.00
0.25
0.50
0.75
1.00
1.25
ELECTRON ENERGY MEV
PST-GL
PST-PST
DOSE RATIO
1.40
1.30
1.20
1.10
1.00
0.90
0.00
0.25
0.50
0.75
1.00
1.25
ELECTRON ENERGY MEV

Figure 4-16

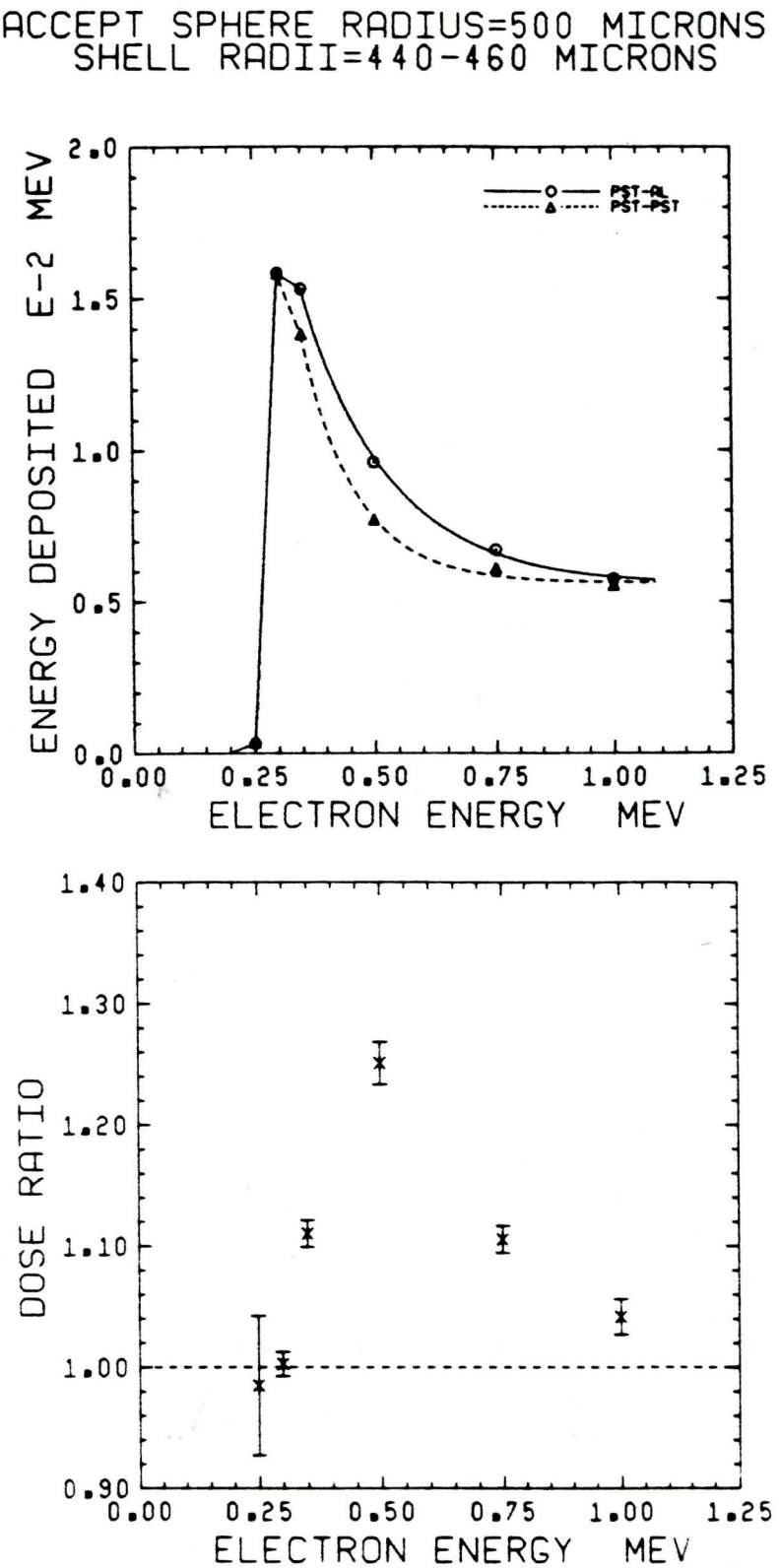
ACCEPT SPHERE RADIUS=500 MICRONS
SHELL RADII=440-460 MICRONS
ENERGY DEPOSITED E-2 MEV
2.0
1.5
1.0
0.5
0.0
PST-AL
PST-PST
0.00
0.25
0.50
0.75
1.00
1.25
ELECTRON ENERGY MEV
DOSE RATIO
1.40
1.30
1.20
1.10
1.00
0.90
0.00
0.25
0.50
0.75
1.00
1.25
ELECTRON ENERGY MEV

Figure 4-17

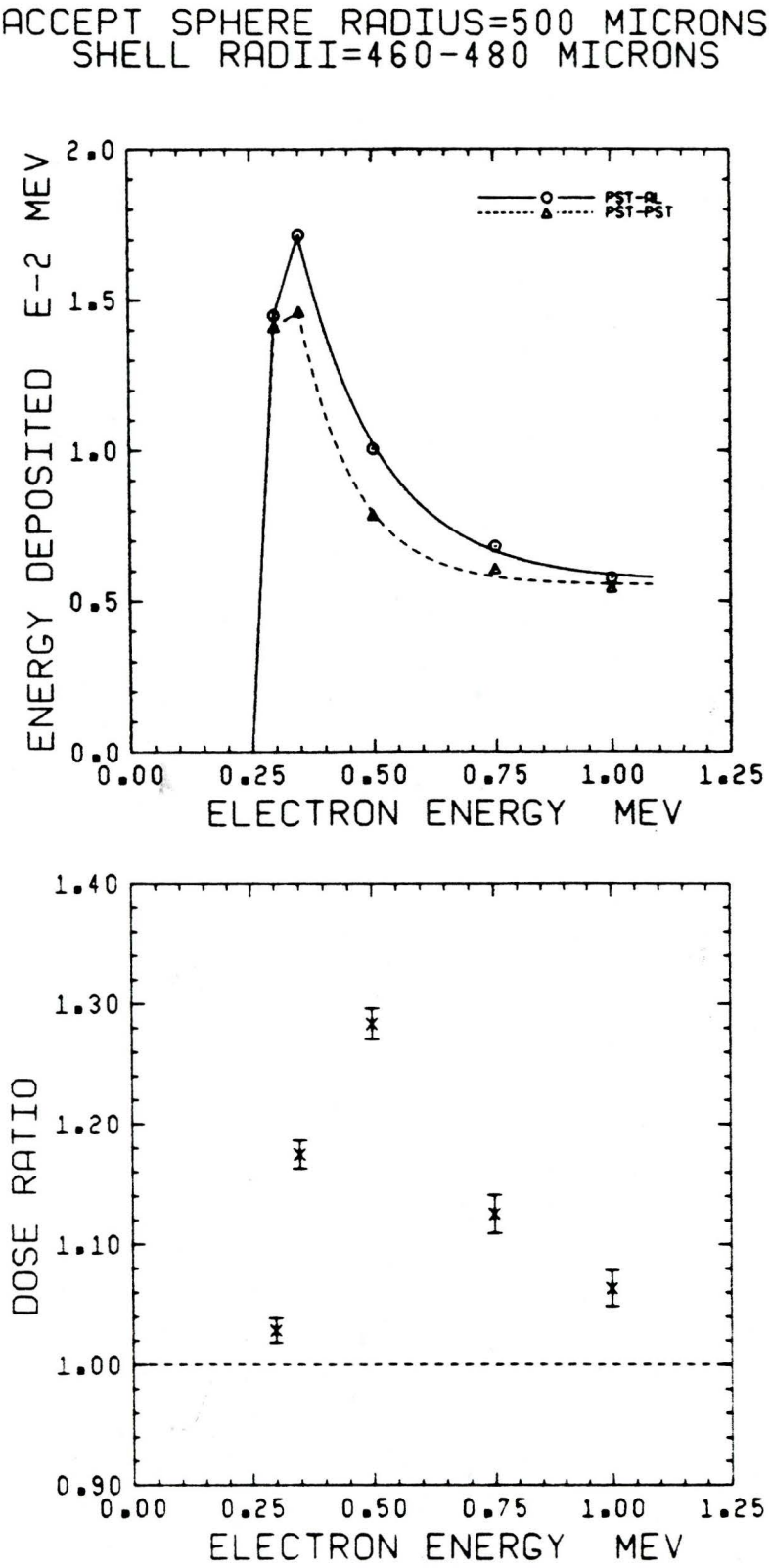
ACCEPT SPHERE RADIUS=500 MICRONS
SHELL RADII=460-480 MICRONS
ENERGY DEPOSITED E-2 MEV
2.0
1.5
1.0
0.5
0.0
PST-GL
PST-PST
0.00
0.25
0.50
0.75
1.00
1.25
ELECTRON ENERGY MEV
DOSE RATIO
1.40
1.30
1.20
1.10
1.00
0.90
0.00
0.25
0.50
0.75
1.00
1.25
ELECTRON ENERGY MEV

Figure 4-18

ACCEPT SPHERE RADIUS=500 MICRONS
SHELL RADII=480-500 MICRONS
Table of Values in Appendix C, Table C-7

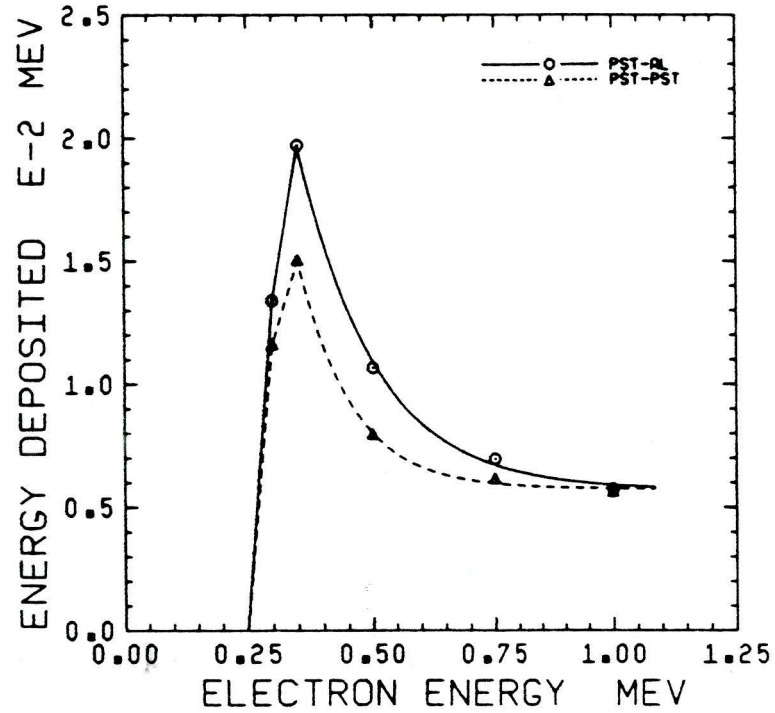

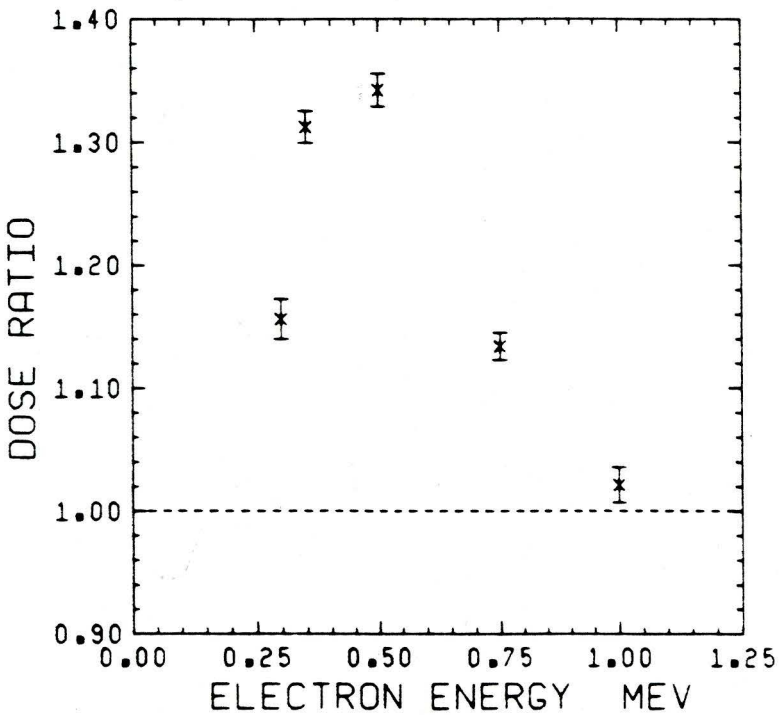

Figure 4-19

DOSE RATIO DUE TO A POINT SOURCE
AT THE CENTER OF A SPHERE
RADIUS=200 MICRONS

Table of values in Appendix C, Table C-8

(The data plotted is fit with function and parameters found in Appendix D)

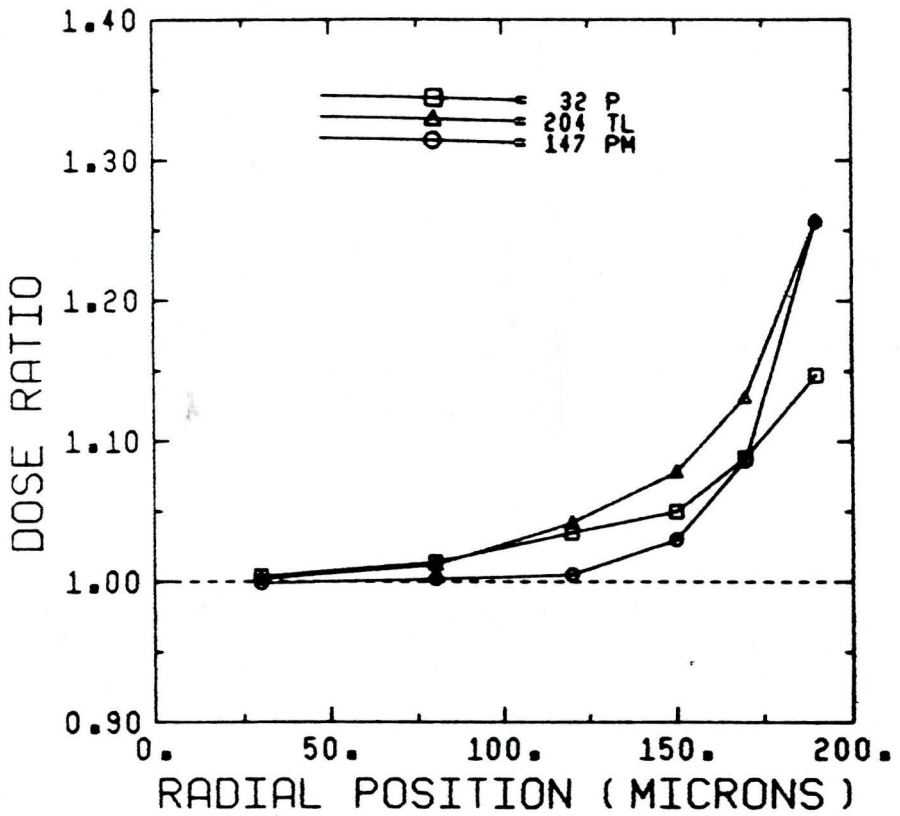

Figure 4-20

DOSE RATIO DUE TO A POINT SOURCE
IN THE CENTER OF A SPHERE
OF RADIUS=500 MICRONS

Table of values in Appendix C, Table C-9

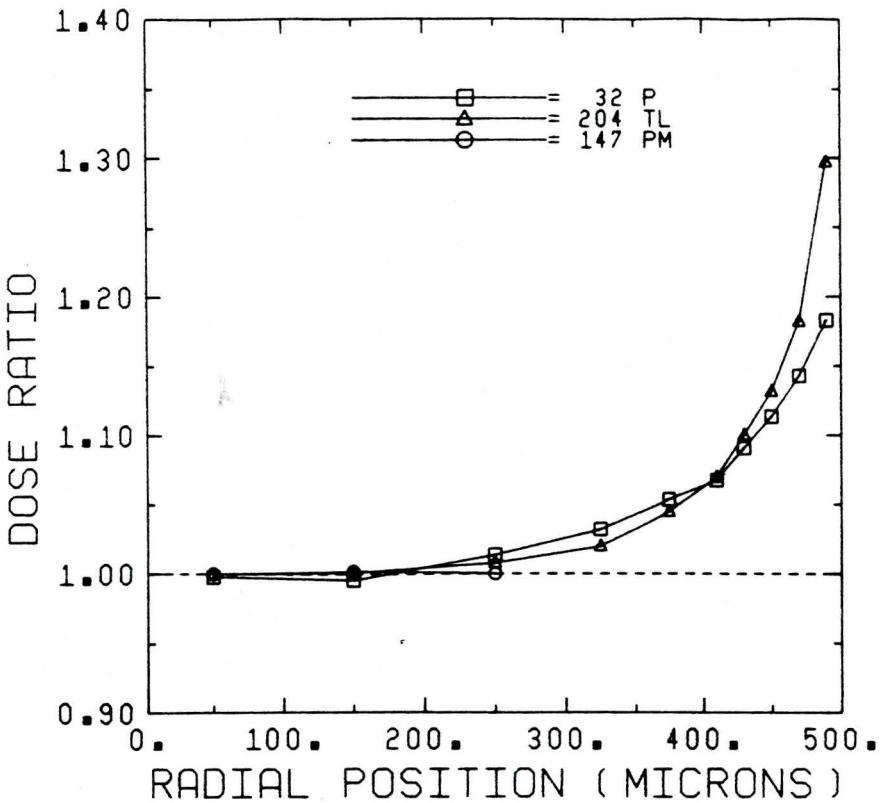

(The data plotted is fit with function and parameters found in Appendix D)

From the preceding graphs, the maximum dose ratio at the PST-Al interface for monoenergetic electrons is approximately 1.35. This maxima occurs at a source energy of 0.30 MeV for the 200 micron sphere and 0.50 MeV for the 500 micron sphere. These energies are used to study the dose ratio in the scoring regions as a function of monoenergetic point source position inside the sphere. Figures 4-21 through 4-26 show the dose ratio inside the 200 micron sphere due to a point source of 0.30 MeV electrons at the radial position as indicated in the Figure title. Figures 4-27 through 4-31 are the dose ratio inside the 500 micron sphere due to a point source of 0.50 MeV electrons at the radial position as indicated in the Figure title.

Figure 4-21

ACCEPT SPHERE RADIUS=200 MICRONS
0.30 MEV POINT SOURCE AT
RADIAL POSITION= 0 MICRONS

(The data plotted is fit with function and parameters found in Appendix D)

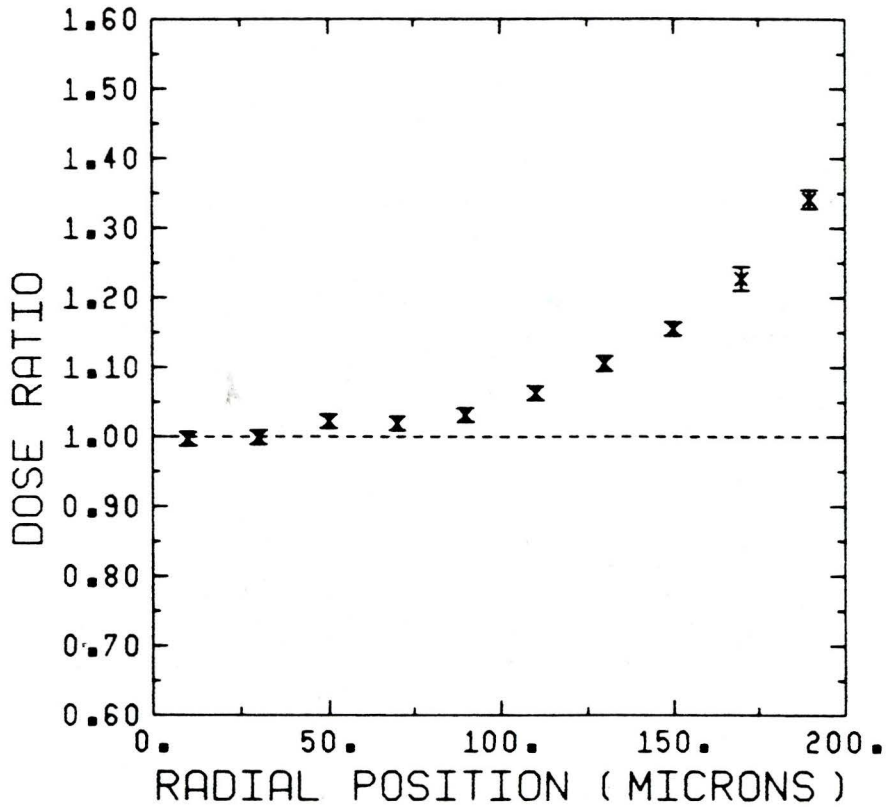

Figure 4-22

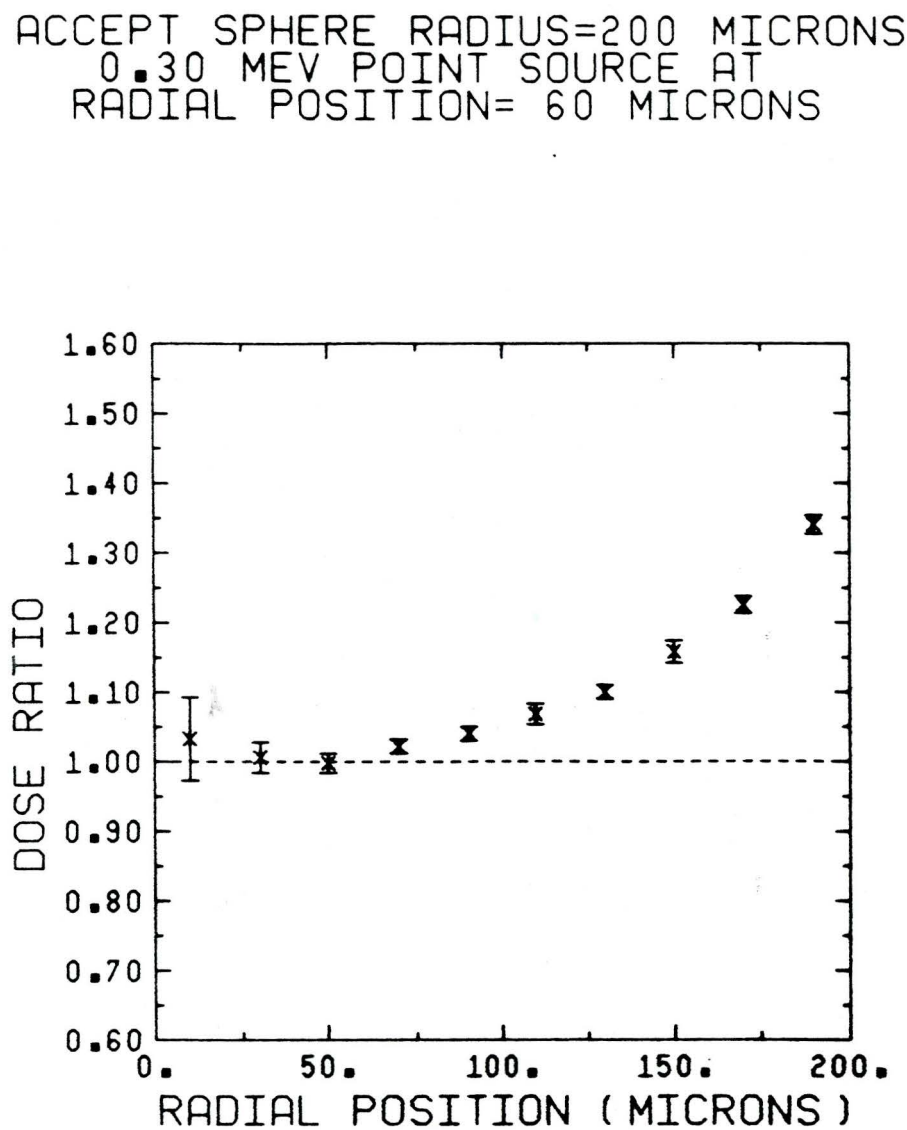
ACCEPT SPHERE RADIUS=200 MICRONS
0.30 MEV POINT SOURCE AT
RADIAL POSITION= 60 MICRONS
DOSE RATIO
1.60
1.50
1.40
1.30
1.20
1.10
1.00
0.90
0.80
0.70
0.60
0.
50.
100.
150.
200.
RADIAL POSITION (MICRONS)

Figure 4-23

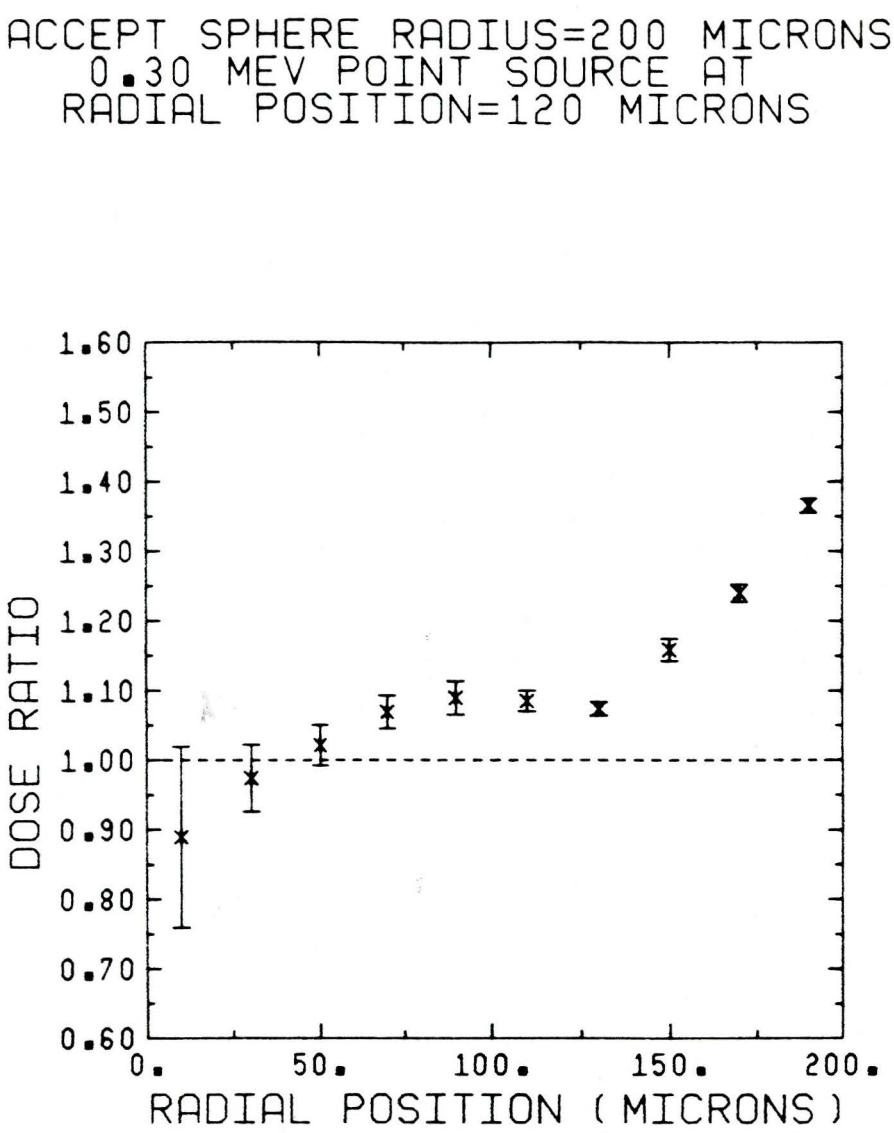
ACCEPT SPHERE RADIUS=200 MICRONS
0.30 MEV POINT SOURCE AT
RADIAL POSITION=120 MICRONS
DOSE RATIO
1.60
1.50
1.40
1.30
1.20
1.10
1.00
0.90
0.80
0.70
0.60
0.
50.
100.
150.
200.
RADIAL POSITION (MICRONS)

Figure 4-24

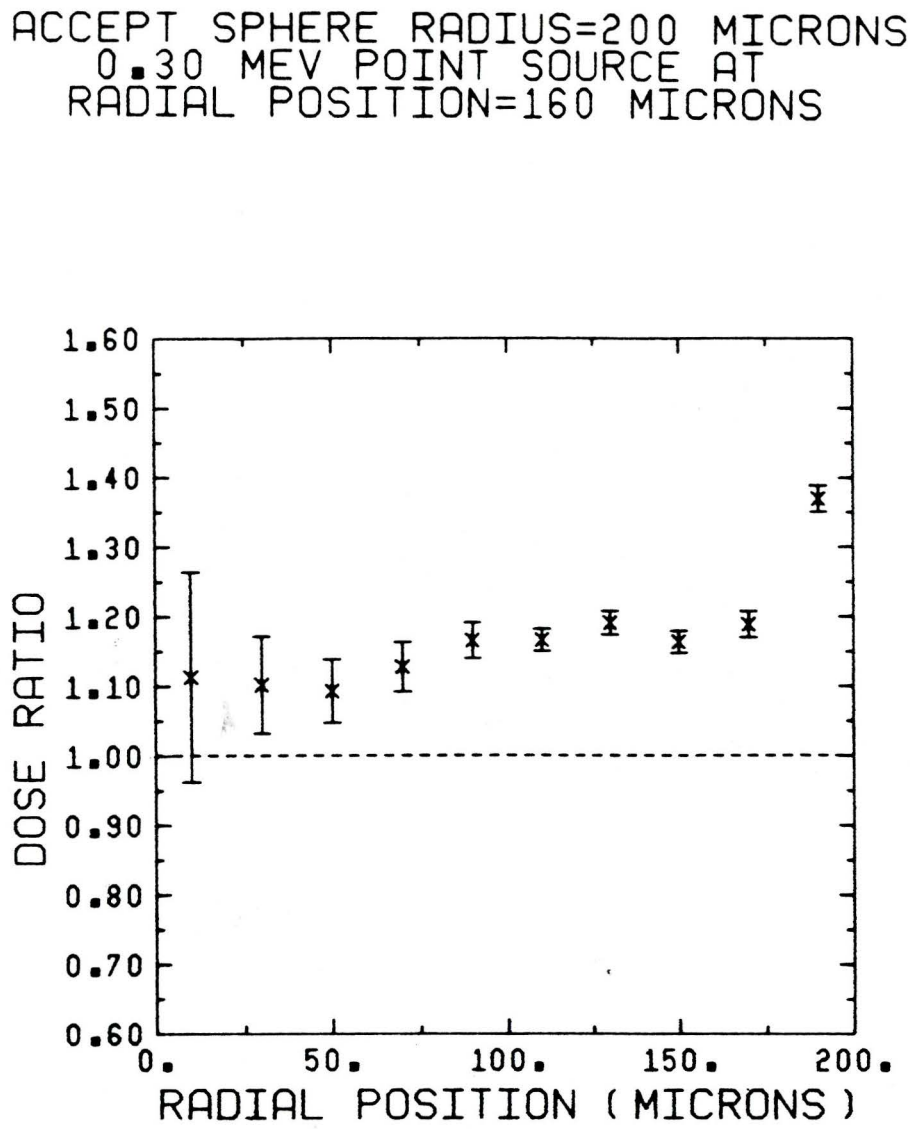
ACCEPT SPHERE RADIUS=200 MICRONS
0.30 MEV POINT SOURCE AT
RADIAL POSITION=160 MICRONS
DOSE RATIO
1.60
1.50
1.40
1.30
1.20
1.10
1.00
0.90
0.80
0.70
0.60
0.
50.
100.
150.
200.
RADIAL POSITION (MICRONS)

Figure 4-25

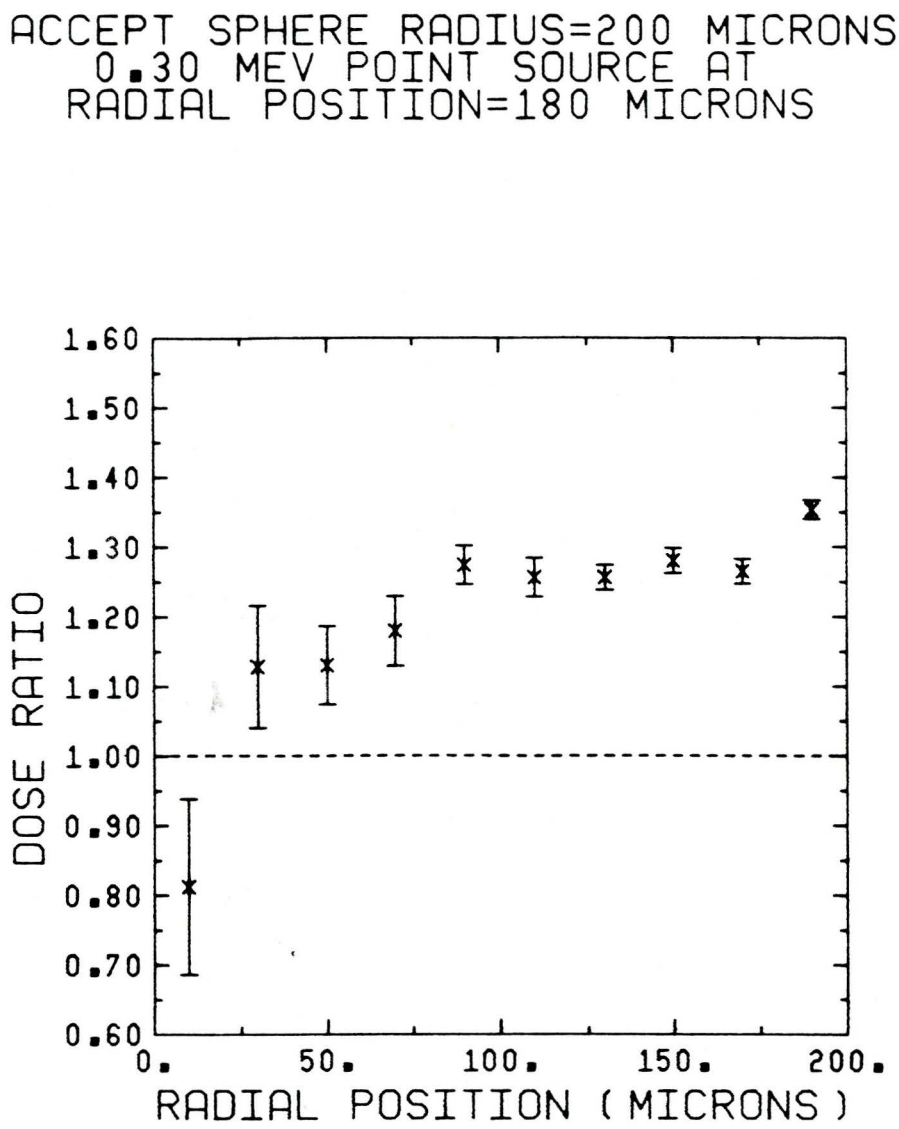
ACCEPT SPHERE RADIUS=200 MICRONS
0.30 MEV POINT SOURCE AT
RADIAL POSITION=180 MICRONS
DOSE RATIO
1.60
1.50
1.40
1.30
1.20
1.10
1.00
0.90
0.80
0.70
0.60
0.
50.
100.
150.
200.
RADIAL POSITION (MICRONS)

Figure 4-26

ACCEPT SPHERE RADIUS=200 MICRONS
0.30 MEV POINT SOURCE AT
RADIAL POSITION=200 MICRONS

Table of values in Appendix C, Table C-10.

(The data plotted is fit with function and parameters found in Appendix D)

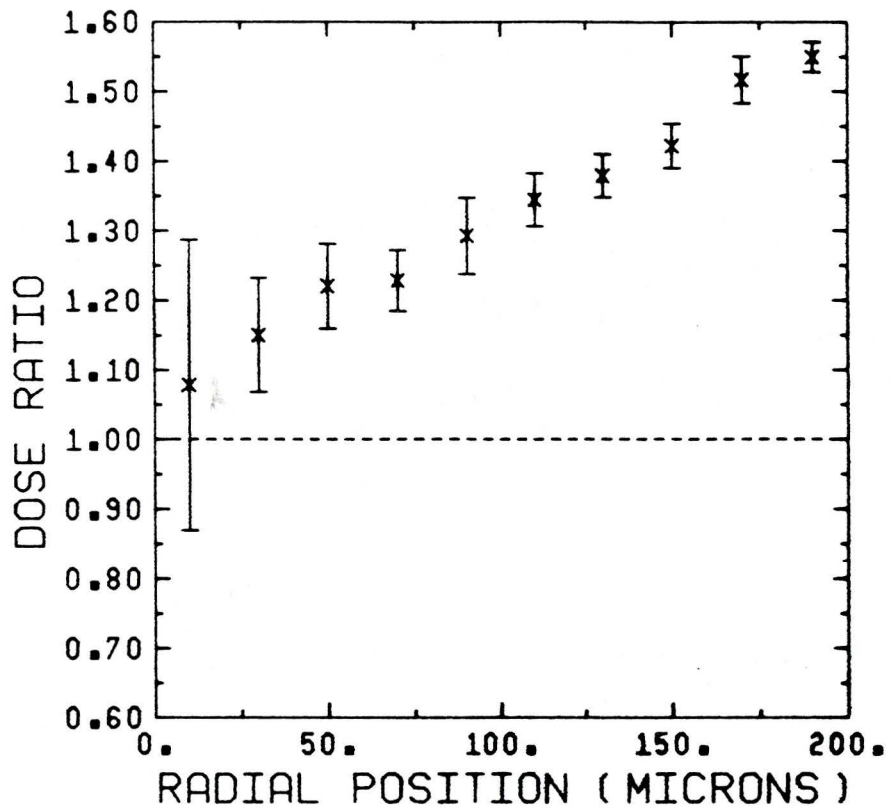

Figure 4-27

ACCEPT SPHERE RADIUS=500 MICRONS
0.50 MEV POINT SOURCE AT
RADIAL POSITION=0.0 MICRONS

(The data plotted is fit with function and parameters found in Appendix D)

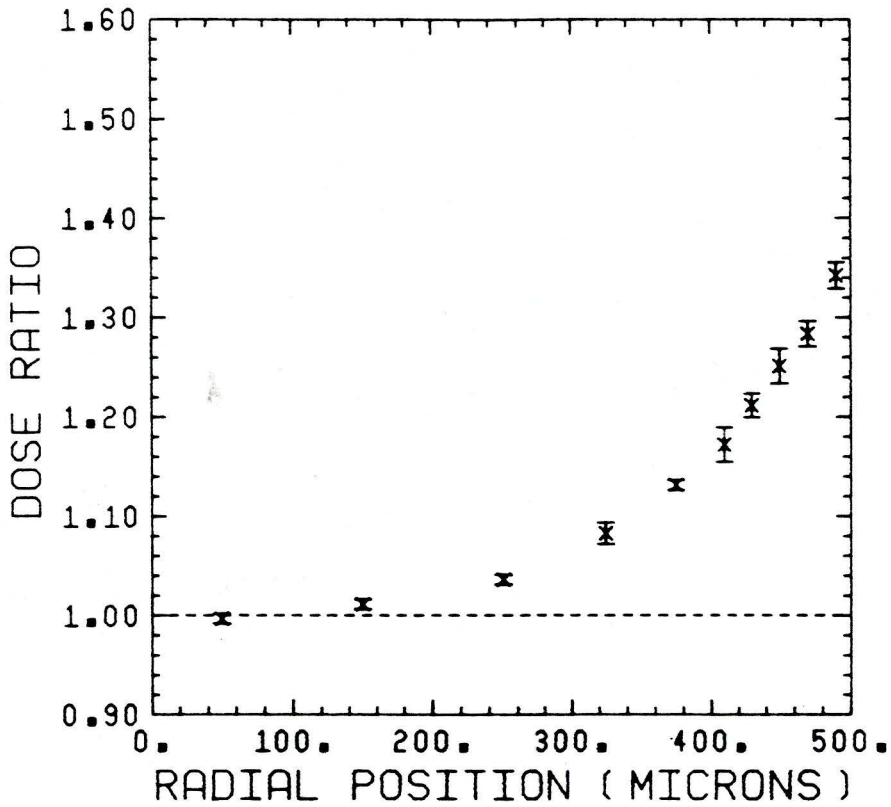

Figure 4-28

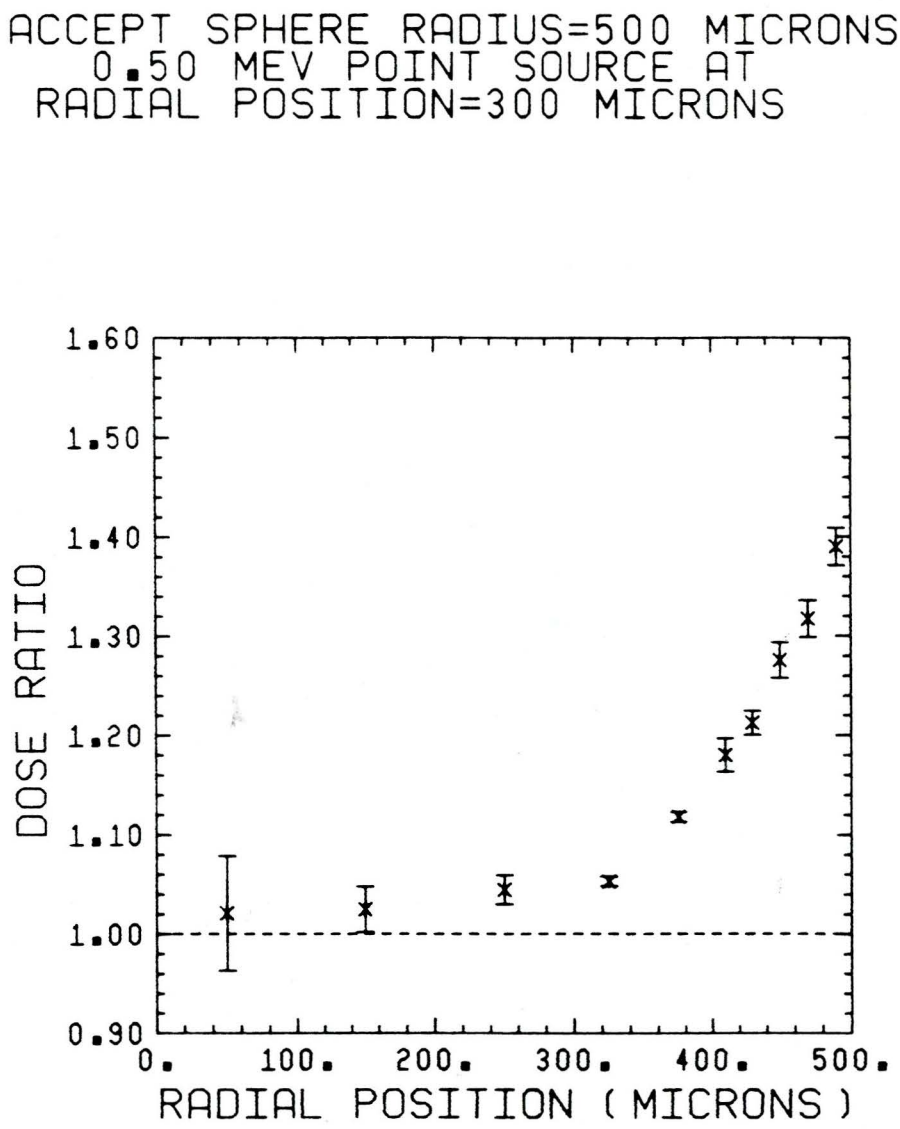
ACCEPT SPHERE RADIUS=500 MICRONS
0.50 MEV POINT SOURCE AT
RADIAL POSITION=300 MICRONS
DOSE RATIO
1.60
1.50
1.40
1.30
1.20
1.10
1.00
0.90
0.
100.
200.
300.
400.
500.
RADIAL POSITION (MICRONS)

Figure 4-29

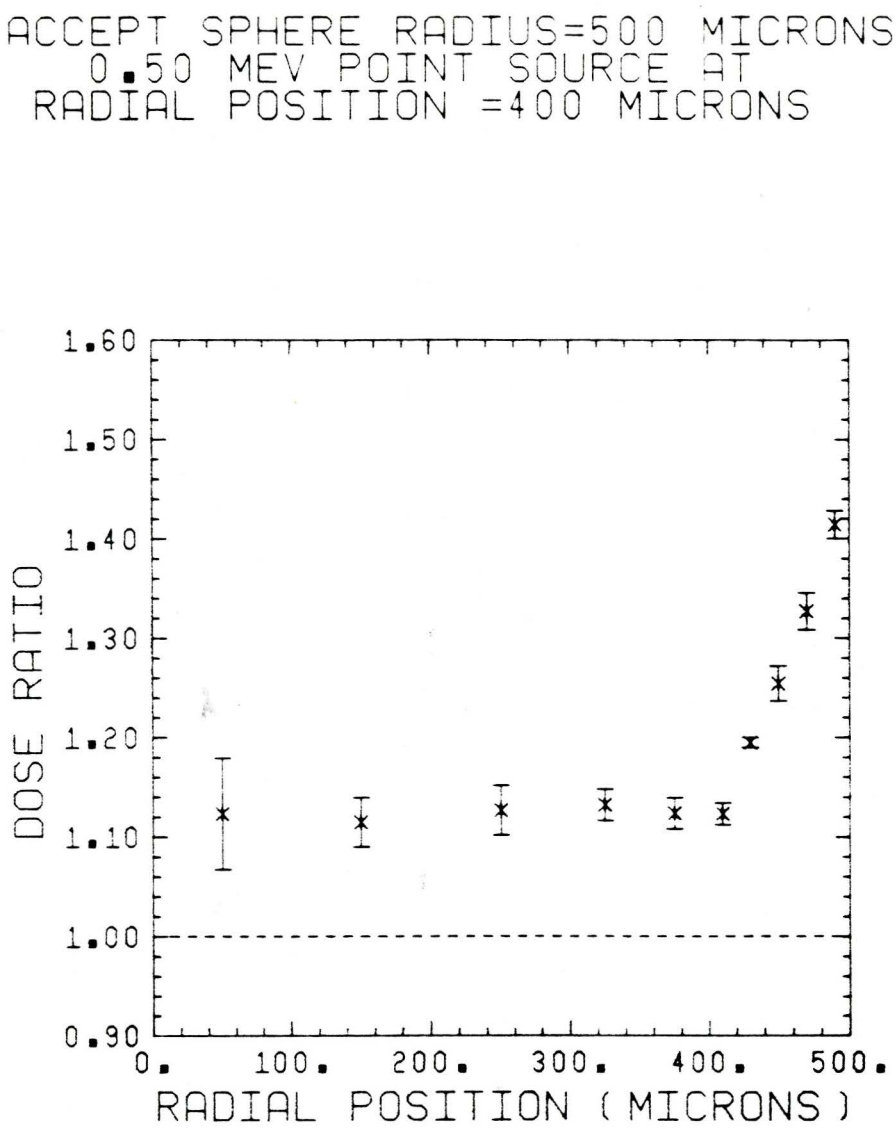
ACCEPT SPHERE RADIUS=500 MICRONS
0.50 MEV POINT SOURCE AT
RADIAL POSITION =400 MICRONS
DOSE RATIO
1.60
1.50
1.40
1.30
1.20
1.10
1.00
0.90
0.
100.
200.
300.
400.
500.
RADIAL POSITION (MICRONS)

Figure 4-30

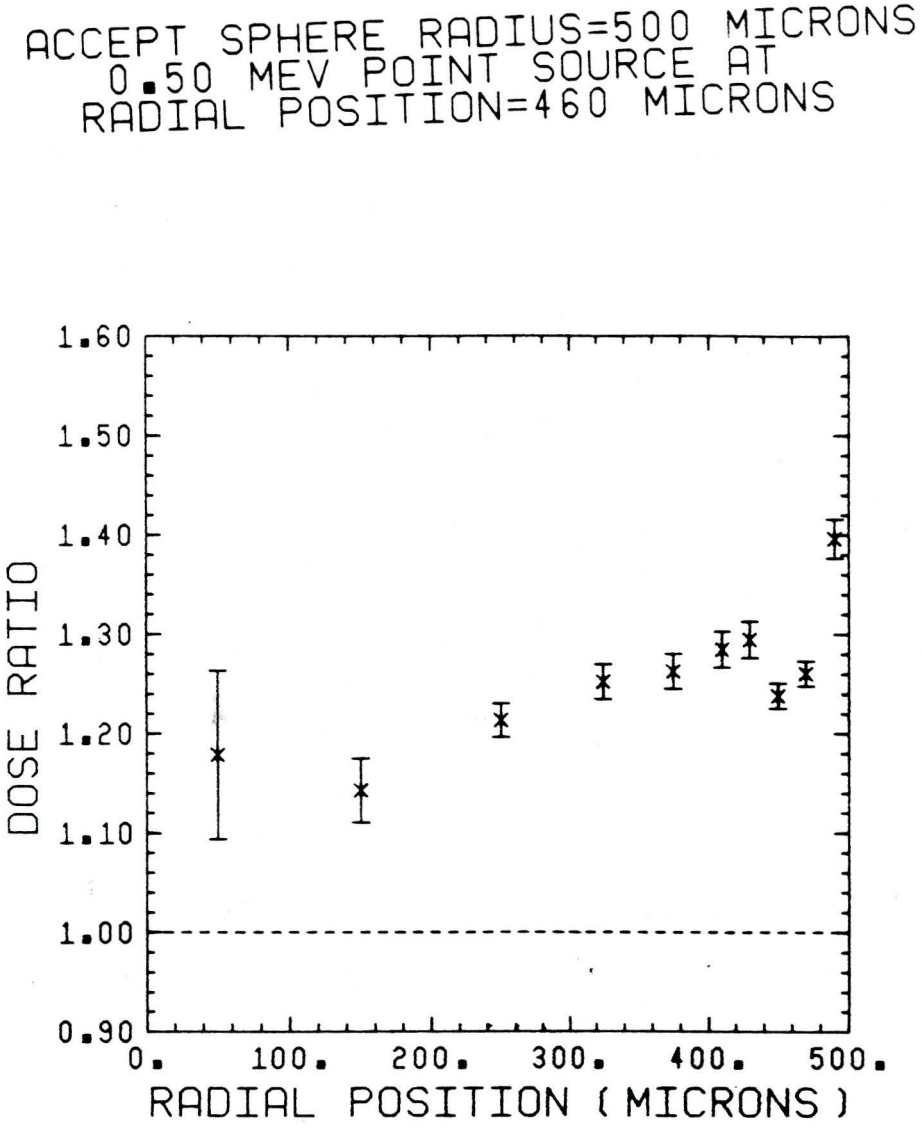
ACCEPT SPHERE RADIUS=500 MICRONS
0.50 MEV POINT SOURCE AT
RADIAL POSITION=460 MICRONS
DOSE RATIO
1.60
1.50
1.40
1.30
1.20
1.10
1.00
0.90
0.
100.
200.
300.
400.
500.
RADIAL POSITION (MICRONS)

Figure 4-31

ACCEPT SPHERE RADIUS=500 MICRONS
0.50 MEV POINT SOURCE AT
RADIAL POSITION=500 MICRONS
Table of values in Appendix C, Table C-11

(The data plotted is fit with function
and parameters found in Appendix D)

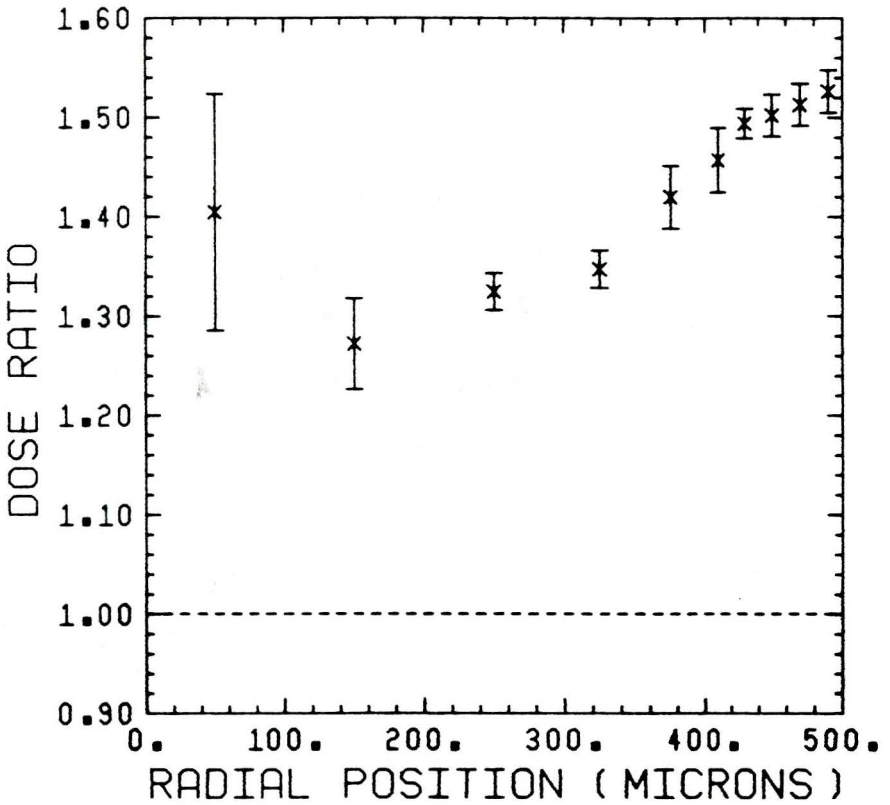

After determining the dose in each scoring region as a function of the radial point source position, a computer program was written (Appendix B) to integrate the dose in a scoring region with the point source position. This approximates the dose in the scoring region due to a homogeneous distribution of monoenergetic electrons in the sphere.

Let D(r,s) be the energy deposited in a scoring region "s" as a function of radial point source position "r". (This function was determined by linear interpolation of the Monte Carlo values.) A function of this type was obtained for both the PST-Al and PST-PST geometries for each scoring region. The integral takes the following form to find the energy deposited in a scoring region due to a homogenous distribution of electrons:

$$E_{PST}(S) = \int\int D_{PST}(r,s)\ r^2 dr\ d\Omega$$

$$E_{PAL}(S) = \int\int D_{PAL}(r,s)\ r^2 dr\ d\Omega$$

where

$E_{PST}(S)$ = Total energy deposited in the scoring region "s" (PST-PST geometry)

$E_{PAL}(S)$ = Total energy deposited in the scoring region "s" (PST-Al geometry)

$D_{PST}(r,s)$ = Energy deposited as a function of radial point source position in scoring region "s" (PST-PST geometry).

$D_{PAL}(r,s)$ = Energy deposited as a function of radial point source position in scoring region "s" (PST-Al geometry)

$d\Omega$ = element of solid angle.

The dose ratio in scoring region "s" due to a homogeneous distribution of electrons is $E_{PAL}(S)/E_{PST}(S)$. Figures 4-32 and 4-33 show the dose ratio due to a homogeneous distribution of monoenergetic electrons as a function of radial position for the 200 micron sphere (0.30 MeV electrons) and the 500 micron sphere (0.50 MeV electrons) respectively.

The dose ratio for the whole sphere is found by summing the energy deposited in each scoring region in the PST-Al geometry and that in the PST-PST geometry and then dividing the former sum by the latter.

$$\text{Dose Ratio} = \frac{\sum_s \int D_{PAL}(r,s) r^2 dr}{\sum_s \int D_{PST}(r,s) r^2 dr}$$

where the summation takes place over all the sphere scoring regions "s".

The average dose ratio in the whole sphere was calculated to be:

$1.22 \pm .04$ (200 micron sphere)

$1.19 \pm .03$ (500 micron sphere)

Figure 4-32

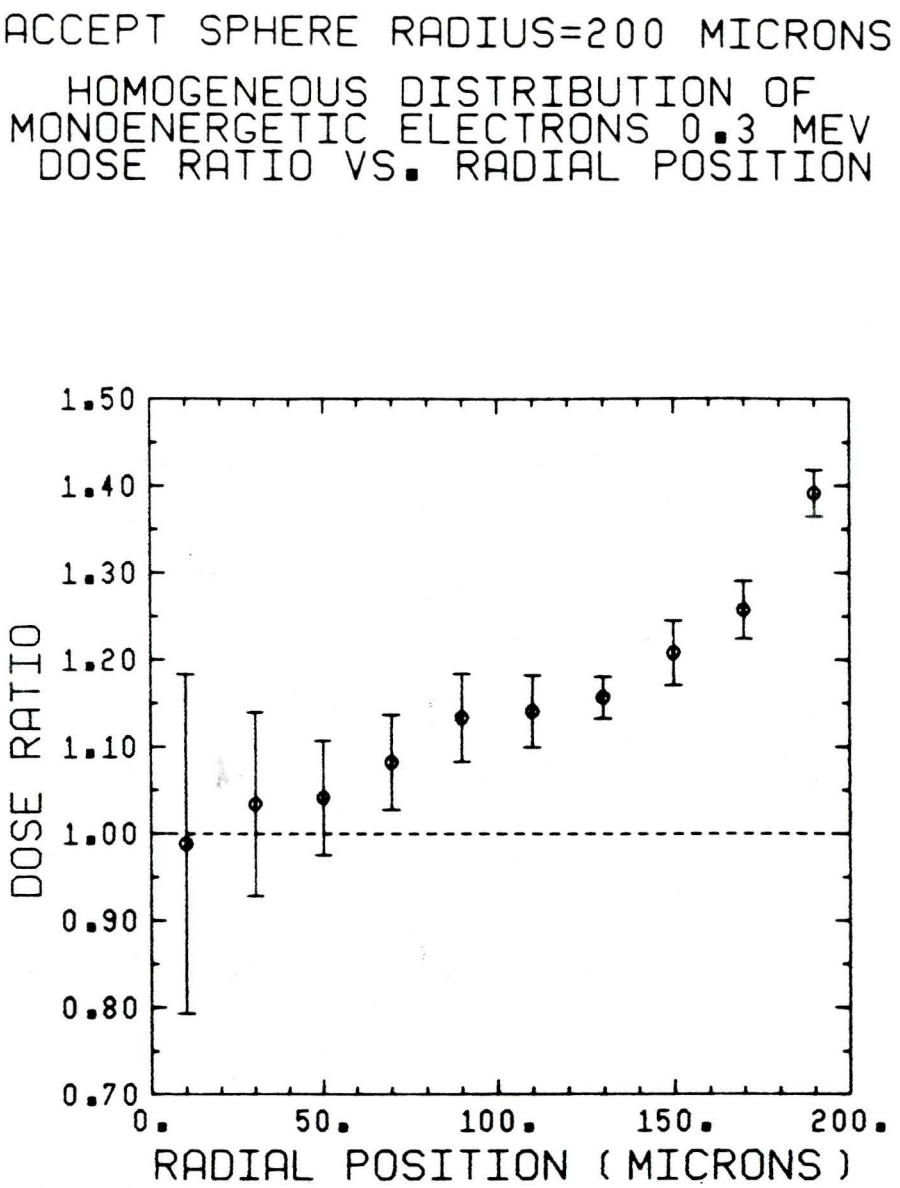
ACCEPT SPHERE RADIUS=200 MICRONS
HOMOGENEOUS DISTRIBUTION OF MONOENERGETIC ELECTRONS 0.3 MEV
DOSE RATIO VS. RADIAL POSITION
DOSE RATIO
1.50
1.40
1.30
1.20
1.10
1.00
0.90
0.80
0.70
0.
50.
100.
150.
200.
RADIAL POSITION (MICRONS)

Figure 4.33

ACCEPT SPHERE RADIUS=500 MICRONS

HOMOGENEOUS DISTRIBUTION OF MONOENERGETIC ELECTRONS 0.5 MEV DOSE RATIO VS. RADIAL POSITION

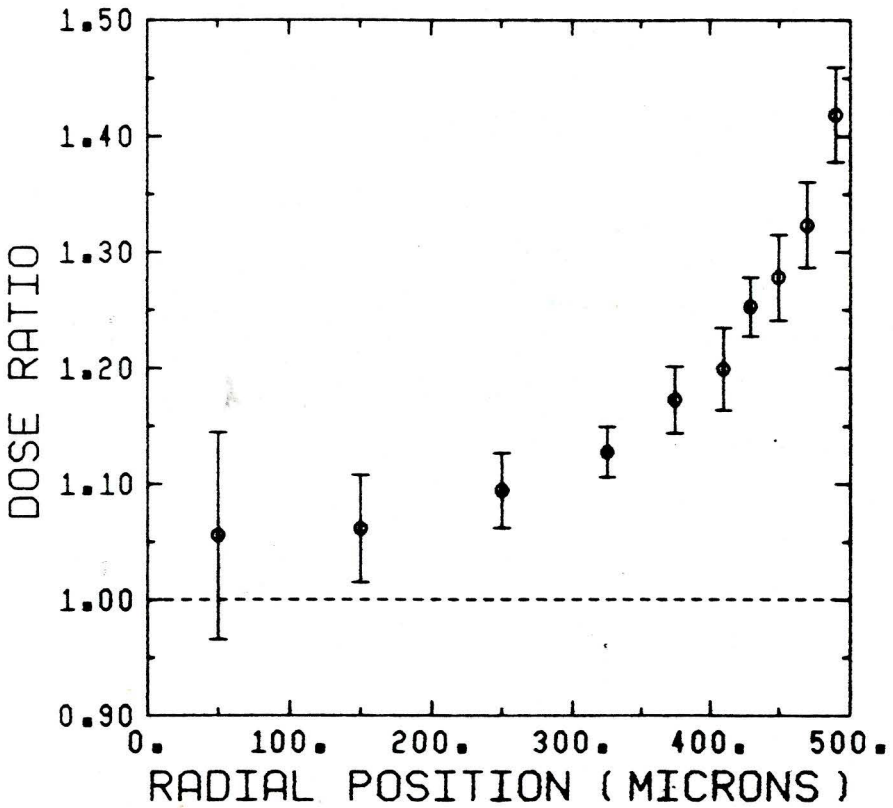

CHAPTER 5

CONCLUSION

Radioimmunotherapy will probably be used to treat conventionally undetectable micrometastases. A systemic introduction of activity would be limited by the dose to the radiosensitive red bone marrow and endosteum. The dose increase in the marrow cavity due to backscattered electrons from bone is a significant factor in calculating the dose to these tissues. Electron backscatter due to a uniform distribution of monoenergetic electrons can increase the dose to the endosteum by as much as 40% and red marrow by 20%.

When applying the results of this project directly to the marrow cavities, two sources of overestimation should be considered. Firstly, the results are overestimated due to the increased backscatter from aluminum (approximately a 14% increase in backscatter from aluminum relative to bone (refer to Chapter 3)). Another source of overestimation is due to the trabeculae not being thick enough for the saturation of electron backscatter. The trabeculae have typical thickness 100 microns (SP169) to 250 microns (ECK85b). The thickness

of aluminum required for "saturation backscatter" into vacuum for 0.50 MeV electrons is 0.35R where R is the CSDA range in Aluminum (BER63). Applying this to the thickness of trabeculae, saturation backscatter is achieved for 0.20 to 0.35 MeV electrons (using CSDA range in cortical bone ICRU37).

Using Monte Carlo methods, Eckerman (1985b) calculated the absorbed fraction in red marrow due to monoenergetic electrons within the marrow cavity. (The absorbed fraction $\phi(r_t \leftarrow r_s)$ is the ratio of the energy imparted to target volume r_t divided by the total energy emitted by source r_t). The method he used did not consider the dose increase due to electron backscatter. Using the data generated in this project for the 200 and 500 micron (radius) spheres, the absorbed fraction (red marrow - red marrow) in lumbar vertebrae due to 0.30-0.50 MeV electrons could be increased by a factor of 1.2. Electron backscatter from low energy electrons, therefore, results in a significant correction to electron dose in the marrow cavities.

REFERENCES

BAI80 N. Bailey. "Electron Backscattering", Med. Phys. 7(5), pp.514-519 (1980).

BAR75 D.E. Barber, R. Moore, T. Hutchinson. "Response of LiF to 1.0-4.0 KeV Electrons", Health Physics 28, pp.13-15 (1975).

BER63 M.J. Berger. "Monte Carlo Calculation of the Penetration and Diffusion of Fast Changed Particles" in "Methods In Computational Physics", B. Alder, S. Fernbach, M. Rotenberg eds. (Academic Press, New York, 1963) pp.135-215.

BIG85 R.E. Bigler, P.B. Zanzonico, R. Leonard, et al. "Bone Marrow Dosimetry for Monoclonal Antibody Therapy", in "Fourth International Radiopharmaceutical Dosimetry Symposium", (Oak Ridge Tennessee, November 5-8, 1985) pp.535-544.

CAR84 J.A. Carrasquillo, K.A. Krohn, P. Beaumier, et al. "Diagnosis of and Therapy for Solid Tumors with Radiolabelled Antibodies and Immune Fragments", Cancer Treat. Rep. 68, pp.317-328 (1984).

CON67 CON-RAD Thermoluminescence Dosimetry System. Model 5100B Readout Instrument, Operation Manual" (Controls for Radiation Inc. Cambridge, Massachusetts, 1967) p.1-2.

CRE77 P.J. Craven and E. Mihich. "The Clinical Toxicity of Anticancer Drugs and its Prediction", Semin. Oncol. 4, pp.147-163 (1977) in BIG85.

CRO68 W.G. Cross. "Variation of Beta Dose Attenuation in Different Media", Phys.Med.Biol. 13,pp.611-618 (1968).

CRO83 W.G. Cross, H. Ing, N. Freedman. "A Short Atlas of Beta-ray Spectra", Phys. Med. Biol. Vol. 28, No. 11, pp.1251-1260 (1983).

DEV85 V.T. De Vita, S. Hellman, and S.A. Rosenberg, eds. "Cancer Principle and Practice of Oncology" 2nd ed. Vol. 2 (J.B. Lippincott Company, Philadelphia, 1985) p.2232.

ECK85a K.F. Eckerman, J.C. Ryman, A.C. Taner et al. "Traversal of cells by Radiation and Absorbed function estimates for electrons and alpha particles", in "Fourth International Radiopharmaceutical Dosimetry Symposium" (Oak Ridge, Tennessee, November 5-8, 1985) pp.67-82.

ECK85b K.F. Eckerman. "Aspects of radionuclides within the skeleton with particular emphasis on the active marrow", in "Fourth International Radiopharmaceutical Dosimetry Symposium" (Oak Ridge, Tennessee, November 5-8, 1985) pp.514-544.

EPE82 A.A. Epenetos, K.E. Britton, S. Mather, et al. Targeting of Iodine-123-Labelled Tumor-Associated Monoclonal Antibodies to Ovarian, Breast and Gastrointestinal Tumors", Lancet 2, pp.999-1004 (1982).

EVA55 Robley Evans. "The Atomic Nucleus" (McGraw-Hill, New York, 1955) Chapter 18 "Ionization of Matter by Charged Particles".

EVE60 T.E. Everhart. "Simple Theory Concerning the Reflection of Electrons from solids", J. Appl.Phys.31, pp.1483-1490 (1960).

FAR82 P.A. Farrands, A.C. Perkins, M.V. Pimm, et al. "Radioimmunodetection of Human Colorectal Cancers by an Anti-Tumor Monoclonal Antibody". Lancet 2, pp.397-400 (1982).

FIS85 D.K. Fisher. "The micro-dosimetry of Monoclonal Antibodies labelled with alpha emitters" in "Fourth International Radiopharmaceutical Dosimetry Symposium", (Oak Ridge, Tennessee, November 5-8, 1985) pp.26-36.

GOL80 D.M. Goldenberg, E.E. Kim, F.H. Deland, et al. "Radioimmunodetection of Cancer with Radioactive Antibodies to Carcinoembryonic antigen", Cancer Res. 40, pp.2984-2992 (1980).

HAM84 Hammersmith Oncology Group. "Antibody-Guided Irradiation of Malignant Lesions: Three Cases Illustrating a New Method of Treatment", Lancet 1, pp.1441-43 (1984).

HEL82 K.E. Hellstrom, I. Hellstrom. Antigens in Human Melanomas detected by using Monoclonal Antibodies as Probes, In "Melanoma Antigens and Antibodies", (Plenum, New York, 1982).

HOA84 H.C. Hoagland. "Hematologic Complications of Cancer Chemotherapy," In M.C. Perry and J.W. Yarbro, "Toxicity of Chemotherapy" (Grune and Stratton, New York, 1984) pp.433-448. In BIG85.

ICRP38 Radionuclide Transformations: Energy and Intensity of Emissions, Annals of the ICRP, ICRP publication 38, Volume 11-13, (1983).

ICRU37 International Commission on Radiation Units and Measurements, "Stopping Power for Electrons and Positions; ICRU37" (ICRU, Bethesda, 1984).

KAS67 J. Kastner, R. Hukkoo, B.G. Oltman, et al. "Thermoluminescent Internal Beta-Ray Dosimetry", Radiation Research 32, pp.625-640 (1967).

KNO79 Glenn Knoll. "Radiation Detection and Measurement" (John Wiley and Sons, Toronto, 1979) pp.56-62.

KWO85 C.S. Kwok, M. Irfan, M.K. Woo, et al. "Effect of Tissue in Homogeneity on Beta Dose Calculation", In "Fourth International Radiopharmaceutical Dosimetry Symposium, (Oak Ridge, Tennessee, November 5-8, 1985) pp.545-561.

LAT69 Robert Lattes. "Methods of Resolution for Selected Boundary Problems in Mathematical Physics", (Gordon and Breach Science Publishers, New York, 1969) p.125.

PRE85 W.V. Prestwich, L.B.Chan, C.S. Kwok, et al. "Dose point kernels for Beta-emitting radioiosotopes", In "Fourth International Radiopharmaceutical Dosimetry Symposium, (Oak Ridge, Tennessee, November 5-8, 1985) pp.545-561.

RAI83 R.M. Rainsbury, R.J. Ott, J.H. Westwood, et al. "Location of Metastatic Breast Carcinoma by a Monoclonal Antibody Chelate Labelled with Indium-111", Lancet 12, pp.934-38, (1983).

ROG84 D.W.O. Rogers. "Low Energy Electron Transport with EGS." Nuclear Instr. and Meth. 227, pp.535-548 (1984).

SHA79 K.K. Sharma, M.Singh. "Variation of Beta-ray backscattering with target thickness", J. Appl. Phys. 50, pp 1529-32 (1979).

SPI69 F.W. Spiers. "Transition-zone Dosimetry" In Radiation Dosimetry Vol 3, Sources, Fields, Measurements and Applications" 2nd ed., ed. F.H. Arrix and E. Tochilin. (Academic Press, New York, 1969) pp.811-817.

TAB71 T. Tabata, R. Ito, S. Okabe. "An Empirical Equation for the Backscattering coefficient of Electrons", Nucl. Instr. and Meth. 94, pp.509-513 (1971)

WES86 B.W. Wessels, M.H. Griffith. "Miniature TLD Absorbed Dose Meausrements in Tumor Phantom Models", J. Nucl. Med. 27, pp.1308-14 (1986).

WOO82 H.Q. Woodward, D.R. White. "Bone models for use in radiotherapy dosimetry", Brit. J. of Radiol. 55, pp.277-282 (1982).

WOOD82 James Wood. "Computational Methods - Reactor Shielding" (Pergamon Press, Toronto, 1982) p.274.

APPENDIX A

```
      PROGRAM BETDOS
      REAL Y(301),ENG(301)
      REAL A(5,8),Q(2,4)
      CHARACTER ISO*6,ANS*1
      COMMON/BETPAR/ALPHZ,V0,GAM,RATIO,C1
      COMMON/PI/XPI
      COMMON/FRBDN/A1,A2,A3,A4,A5,A6,B1,B2
      COMMON/DAT/A,Q
      OPEN(UNIT=1,FILE='PRN')
      PRINT*,'  '
    1 PRINT*,'WOULD YOU LIKE TO PREFORM A SPECTRAL INTEGRATION [Y,N]'
      READ*,ANS
      IF (ANS.EQ.'N') GOTO 901
      PRINT*,'ISOTOPE '
      READ*,ISO
      WRITE(1,500) 'ISOTOPE: ',ISO
  500 FORMAT(10X,A8,A)
      WRITE(1,*)
      PRINT*,'Z(DAUGHTER),E0(MeV),L'
      READ*,Z,E0,L
      IZ=INT(Z)
      WRITE(1,510) 'DAUGHTER ATOMIC NO.: ',IZ
  510 FORMAT(A,I3)
      WRITE(1,520) 'END-POINT ENERGY :',E0,' MeV'
  520 FORMAT(A,F5.3,A)
      WRITE(1,*) 'FORBIDDENESS :',L
      WRITE(1,*)
      CALL SETUP(Z,E0)
      DEL=E0/300.0
      TOT=0.0
      ETOT=0.0
      ABA=0.0
      FUN=0.0
      DO 10 I=1,300
       E=DEL*(FLOAT(I-1)+0.5)
       CALL BETA(Z,E0,L,E,S)
       Y(I)=S
       ENG(I)=E
       TOT=TOT+S
       IF (E.GE.0.10) GOTO 93
       FUN=99.85*E
       GOTO 99
   93  IF (E.GE.0.2) GOTO 97
       FUN=-52.02*E + 15.187
       GOTO 99
   97  IF (E.GE.1.0) GOTO 98
       FUN=2.5674 +5.7045*EXP(-E*4.9390)
       GOTO 99
   98  FUN=2.598
   99  ETOT=ETOT+S*FUN
      ABA=ABA+E*S
   10 CONTINUE
      EAV=ETOT/TOT
      BAB=ABA/TOT
      PRINT*,'AVERAGE ENERGY',BAB
      PRINT*,'ENERGY VS BETA SPECTRUM DUMPED TO EXTERNAL FILE ? [Y/N]'
      READ*,ANS
      IF (ANS.EQ.'N') GOTO 21
      OPEN(UNIT=2,FILE=ISO)
      DO 20 I=1,300
       Y(I)=Y(I)/TOT
       WRITE(2,529)ENG(I),Y(I)
  529  FORMAT(F12.7,F12.7)
   20 CONTINUE
      CLOSE(UNIT=2)
   21 PRINT*,' INTEGRATED CURVE WITH BETA SPECTRUM ',EAV
```

Appendix A, continued

```
      WRITE(1,530)'INTEGRATED CURVE WITH BETA SPECTRUM: ',EAV,' UNITS'
530   FORMAT(A,F5.3,A)
      WRITE(1,540)'     '
      WRITE(1,540)'     '
540   FORMAT(A)
      GOTO 1
901   PRINT*,'END'
      END
      SUBROUTINE SETUP(Z,E0)
      SUBROUTINE TO CALCULATE ENERGY INDEPENDANT PARAMETERS
      USED IN BETA-BACHER APPROXIMATION OF FERMI FUNCTION
      THOMAS-FERMI SCREENING POTENTIAL AND C1 COMPONENT
      OF THE HIGH Z CORRECTION FACTOR.PARAMETERS ARE PASSED
      THROUGH COMMON BLOCK BETPAR.
      ENERGY INDEPENDENT PARAMETERS FOR FIRST-FORBIDDEN
      SHAPE FACTOR ARE PASSED THROUGH COMMON BLOCK FRBDN
      COMMON/BETPAR/ALPHZ,V0,GAM,RATIO,C1
      COMMON/FRBDN/A1,A2,A3,A4,A5,A6,B1,B2
      COMMON/PI/XPI
      ALPHZ=Z/137.0
      ALPHZ IS THE PRODUCT OF AT.NO. WITH FINE STRUCTURE CONSTANT
      V0=(1.13/(137.0**2))*(Z**(4./3.))
      GAM=SQRT(1.0-ALPHZ**2)-1.0
      XPI=4.0*ATAN(1.0)
      U=(1.0+V0)**2
      DEN=U*(ALPHZ**2)+0.25*(U-1.0)
      R=(((ALPHZ**2)/DEN)**GAM)/U
      A=2.0*XPI*(1.0+V0)*ALPHZ
      RATIO=R*(1.0-EXP(-A/SQRT(U-1)))
      ZABS=ABS(Z)
      C1=4.05E-04*(ZABS-50)+2.23E-05*((ZABS-50)**2)
      C1 IS ENERGY INDEPENDENT PART OF HIGH Z
      CORRECTION FACTOR
      THE FOLLOWING ARE THE ENERGY INDEPENDENT PARAMETERS
      USED TO CALCULATE THE L0 TERM OF THE SHAPE FACTOR:
      A1=0.997834+Z*(1.1975E-4-1.85E-5*Z)
      A2=4.555E-4-Z*(1.562E-4+1.0165E-6*Z)
      THE FOLLOWING ARE LINEAR CO-EFFICIENTS USED TO CALCULATE
      THE L1 TERM OF THE SHAPE FACTOR:
      A3=9.55727*(1.0-EXP(-3.81E-4*Z*Z))
      A4=0.5673*(1.-EXP(-4.15E-4*Z*Z))
      A5=0.111235-2.6377E-5*Z-8.738E-6*Z**2+2.204E-8*Z**3
      A6=2.8789E-5-1.146E-5*Z+4.483E-7*Z**2-6.1E-10*Z**3
      THE FOLLOWING ARE EXPONENTIAL CO-EFFICIENTS USED TO
      CALCULATE THE L1 TERM
      B1=20.0641
      B2=4.878-4.166E-3*Z
      RETURN
      END
      SUBROUTINE BETA(Z,E0,L,E,S)
      COMMON/BETPAR/ALPHZ,V0,GAM,RATIO,C1
      COMMON/PI/XPI
      BETPAR COMMON BLOCK TO BE OBTAINED FROM
      SETUP SUBROUTINE.ALPHZ IS PRODUCT OF FINE
      STRUCTURE CONSTANT AND DAUGHTER ATOMIC NUMBER.
      V0 IS THE SCREENING POTENTIAL IN RELATIVISTIC
      UNITS.RATIO CORRECTS THE SPECTRUM FOR E<V0
      L IS 0 FOR ALLOWED AND 1 FOR FIRST-FORBIDDEN.
      W0=1.0+E0/.511
      W=1.0+E/.511
      W1=W
      ETA1=SQRT(W*W-1.0)
      EREL=W-1.0
      W,EREL ARE TOTAL AND KINETIC ENERGIES IN REL. UNITS
      IF(EREL.GT.V0) W=W-V0
      WR=ALPHZ*W
```

Appendix A, continued

```
ETSQ=W*W-1.0
ETA=SQRT(ETSQ)
ETA IS THE MOMENTUM IN RELATIVISTIC UNITS
T1=(W*(E0-E))**2
T2=(WR**2+.25*ETSQ)**GAM
T2 IS THE NUMERATOR IN THE APP.FERMI FUNCTION.
T3=2.0*XPI*WR
IF(Z.GT.50) THEN
 CORR=1.0+C1*(1.0-EXP(-1.26*ETA))
ELSE
 CORR=1.0
ENDIF
IF (EREL.GT.V0) THEN
 S=CORR*T1*T2/(1.0-EXP(-T3/ETA))
ELSE
 S=CORR*T1*T2*RATIO
ENDIF
IF (L.EQ.1) THEN
SHAPE FACTOR CORRECTION FOR FIRST-FORBIDDEN
 CALL SHAPE(ETA,W,W0,SHP)
 S=S*SHP
ELSE
ENDIF
RETURN
END
SUBROUTINE SHAPE(ETA,W,W0,SHP)
ENERGY INDEPENDENT PARAMETERS A1-A6,B1,B2
ARE PASSED FROM SETUP USING COMMON/FRBDN/
REAL L0,L1
COMMON/FRBDN/A1,A2,A3,A4,A5,A6,B1,B2
THE FIRST FORBIDDEN SHAPE FACTOR IS GIVEN
BY SHP=L0*((W0-W)**2)+9.*L1
THE L0 AND L1 FACTORS ARE TABULATED IN
SIEGBAHN.THESE HAVE BEEN APPROXIMATED
HERE AS FOLLOWS:
L0=A1+A2*ETA
 Z1=A3*EXP(-B1*(ETA))+A4*EXP(-B2*(ETA))
Z2=A5+A6*ETA
L1=(Z1+Z2)*(ETA**2)
SHP=L0*((W0-W)**2)+9.0*L1
RETURN
END
```

APPENDIX B

```
10 CLS
20 REM ------------------------------------------------------
30 REM              ACCEPT Spherical Integration
40 REM        This program integrates the energy deposited
50 REM      in a spherical shell volume with respect to radial
60 REM      point source position.Input data is taken from
70 REM      the ACCEPT Monte Carlo code.
80 REM        The program accesses 10 separate data files
90 REM      containing  energy deposited/(unit fluence) as a
100 REM      function of source position for a particular volume.
110 REM      There are ten volumes corresponding to to
120 REM     the spherical shells of inner and outer radii
130 REM     [ i*20 , (i+1)*20 ] microns  { i is an integer 1-10
140 REM     inclusive } for the sphere of radius 200 microns
150 REM    The program is slightly modified for the 500 micron
160 REM    sphere.
170 REM-------------------------------------------------------
180 INPUT " OUTPUT FILENAME: ",B$
190 OPEN B$ FOR OUTPUT AS #2
200 PRINT#2,"output filename :",B$
210 DEFDBL T
220 DIM X(30)
230 DIM A(30)
240 DIM P(30)
250 DIM DP(30)
260 DIM DA(30)
270 DIM TOTA(30)
280 DIM TOTP(30)
290 DIM TOTAER(30)
300 DIM TOTPER(30)
310 A$="00020406081012141618"
320 C$="3AC"
330 F$=".DAT"
340 REM---------- BEGINNING OUTER LOOP - FILE SELECTION------
350 FOR K=1 TO 10
360 Y$= MID$(A$,1+((K-1)*2),2)
370 Z$=C$+Y$+F$
380 OPEN Z$ FOR INPUT AS #1
390 PRINT" FILE CURRENTLY BEING PROCESSED : ",Z$
400 PRINT "THIS IS FILE ",K,"OF 10"
410 REM --------- DATA READ IN -FILE PROCESSING BEGINS-------
420 FOR I=1 TO 6
430 INPUT#1,X(I),A(I),DA(I)
440 NEXT I
450 INPUT#1,EF,EF1,EF2
460 REM  EFS are irrelevant to the program.The data
470 REM  file is formatted to be software compatible.
480 FOR I=1 TO 6
490 INPUT#1,X(I),P(I),DP(I)
500 NEXT I
510 REM-------------------------------------------------
520 REM     Volume integration of energy in shell
530 REM    as a function of source position
540 REM-------------------------------------------------
550 DEL=.2
560 PRINT "       PERCENT COMPLETED "
570 PRINT,0
580 FOR I=1 TO 5
590 XO=X(I)+DEL/2
600 N=(X(I+1)-X(I))/DEL
610 MA=(A(I+1)-A(I)) / (X(I+1)-X(I))
620 MP= (P(I+1)-P(I)) / (X(I+1)-X(I))
630 BA= A(I)-MA*X(I)
640 BP= P(I)-MP*X(I)
650 ERMA=SQR( (DA(I)/A(I))^2 + (DA(I+1)/A(I+1))^2 )
660 ERMP=SQR( (DP(I)/P(I))^2 + (DP(I+1)/P(I+1))^2 )
```

Appendix B, continued

```
670 ERBA=SQR( (DA(I)/A(I))^2 + ERMA^2 )
680 ERBP=SQR( (DP(I)/P(I))^2 + ERMP^2 )
690 FOR J=1 TO N-1
700 ARA=DEL*XO*XO*(MA*XO+BA)
710 ARP=DEL*XO*XO*(MP*XO+BP)
720 TOTAER(K)= TOTAER(K) + ARA*SQR( ERMA^2+ERBA^2 )
730 TOTPER(K)= TOTPER(K) + ARP*SQR( ERMP^2 + ERBP^2 )
740 TOTA(K)=TOTA(K) + ARA
750 TOTP(K)=TOTP(K) + ARP
760 ARA=0
770 ARP=0
780 XO=XO+DEL
790 NEXT J
800 PRINT, INT(100*I/5)
810 NEXT I
820 REM ------- PRINT-OUT -----------
830 PRINT#2,"  "
840 PRINT#2,"-----------------------------------------"
850 PRINT#2,"    INPUT  FILE NAME       ",Z$
860 PRINT#2,  " VOLUME INTEGRAL CORRESPONDING TO SPECIFIED REGION"
870 PRINT#2, " PST-AL  GEOMETRY :",INT(TOTA(K)),"+/-",INT(TOTAER(K))
880 PRINT#2, " PST-PST GOEMETRY :",INT(TOTP(K)),"+/-",INT(TOTPER(K))
890 PRINT#2," "
900 R=TOTA(K)/TOTP(K)
910 REL= 100*SQR( (TOTAER(K)/TOTA(K))^2 + (TOTPER(K)/TOTP(K))^2 )
920 PRINT#2,"  RATIO :",R," +/- ",REL*R/100,"% ERROR",REL
930 REM ---- SCREEN DUMP -----
940 PRINT" "
950 PRINT" FILENAME :",Z$
960 PRINT" "
970 PRINT" AL-PST AREA : ",TOTA(K),"+/-",TOTAER(K)
980 PRINT"PERCENT RELATIVE ERROR :",TOTAER(K)/TOTA(K)*100
990 PRINT" "
1000 PRINT" PST-PST AREA :",TOTP(K),"+/-",TOTPER(K)
1010 PRINT" PERCENT RELATIVE ERROR :",TOTPER(K)/TOTP(K)*100
1020 PRINT" "
1030 PRINT" RATIO AL-PST/PST-PST:",R,"+/-",REL/100*R
1040 PRINT"PERCENT RELATIVE ERROR :",REL
1050 PRINT" "
1060 CLOSE#1
1070 NEXT K
1080 REM-----------------------------------------
1090 REM  CALCULATION OF TOTAL ENERGY DEPOSITED
1100 REM-----------------------------------------
1110 TOTAL = 0
1120 TOTPST=0
1130 ALERR=0
1140 PSTERR=0
1150  FOR I=1 TO 10
1160 TOTAL=TOTAL+ TOTA(I)
1170 TOTPST= TOTPST + TOTP(I)
1180 ALERR= ALERR + TOTAER(I)
1190 PSTERR= PSTERR + TOTPER(I)
1200 NEXT I
1210 REM ----- PRINT OUT / SCREEN DUMP -----
1220 PRINT#2," "
1230 PRINT#2,";;;;;;;;;;;; TOTAL ENERGY DEPOSITED IN SPHERE;;;;;;;;;;;;
1240 PRINT#2," AL-PST TOTAL :",INT(TOTAL),"+/-",INT(ALERR)
1250 PRINT#2,"PERCENT RELATIVE ERROR :",INT(1000*ALERR/TOTAL)/10
1260 PRINT#2," "
1270 PRINT#2," PST-PST TOTAL :",INT(TOTPST),"+/-",INT(PSTERR)
1280 PRINT#2,"PERCENT RELATIVE ERROR :",INT(1000*PSTERR/TOTPST)/10
1290 PRINT#2," "
1300 RAT=TOTAL/TOTPST
1310 UNC= SQR( (ALERR/TOTAL)^2 + (PSTERR/TOTPST)^2 )
1320 PRINT#2," RATIO : ",RAT,"+/-",UNC*RAT
```

Appendix B, continued

```
1330 PRINT#2,"PERCENT RELATIVE ERROR :",INT(1000*UNC)/10
1340 REM ------------SCREEN DUMP---------------
1350 PRINT" "
1360 PRINT"-------------------------------------------"
1370 PRINT"             TOTAL ENERGY DEPOSITED"
1380 PRINT"-------------------------------------------"
1390 PRINT" AL-PST TOTAL :";:PRINT USING "##.######^^^^";INT(TOTAL)
1400 PRINT"PERCENT RELATIVE ERROR :",INT(1000*ALERR/TOTAL)/10
1410 PRINT" "
1420 PRINT" PST-PST TOTAL :",INT(TOTPST),"+/-",INT(PSTERR)
1430 PRINT"PERCENT RELATIVE ERROR :",INT(1000*PSTERR/TOTPST)/10
1440 PRINT" "
1450 PRINT" ratio  :",RAT,"+/-",UNC*RAT
1460 PRINT"PERCENT RELATIVE ERROR ;",INT(1000*UNC*RAT)/10,"%"
1470 END
```

APPENDIX C

Table C-1
Table of values for Figures 3-1 and 3-2.

PST-PST GEOMETRY

Electron Energy (MeV)	Dose E-7 rad/unit fluence* ESTEPE 0.002	0.005	0.01	0.02	0.04
0.20	-	2.394	2.377	-	2.458
0.35	-	-	2.781	-	2.900
0.50	-	-	2.865	-	2.913
0.75	2.887	2.913	2.916	2.955	3.023
1.00	-	-	2.602	-	2.686
1.25	2.374	2.439	2.438	2.447	2.481
1.50	-	-	2.333	-	2.390
1.75	-	-	2.321	-	2.334
2.00	-	-	2.316	-	2.341

PST-AL GEOMETRY

0.20	2.327	-	2.401	-	2.455
0.35	2.937	-	2.914	-	3.038
0.50	3.107	-	3.084	-	3.113
0.75	3.226	-	3.197	-	3.222
1.00	2.955	-	3.012	-	3.029
1.25	2.850	-	2.794	-	2.863
1.50	2.678	-	2.711	-	2.729
1.75	2.599	-	2.630	-	2.623
2.00	2.521	-	2.579	-	2.550

* Errors in dose: standard deviation of the mean less than 1% of value quoted.

Appendix C, continued...

Table C-2

EGS Dosimeter Thickness 31 mg/cm^2

Electron Energy (MeV)	DOSE E-7 RAD/(UNIT FLUENCE)			
	PST-Al		PST-PST	
0.10	0.219	1.0*	0.219	1.0*
0.20	2.461	0.6	2.377	0.4
0.35	2.914	0.8	2.781	0.6
0.50	3.084	0.8	2.865	0.3
0.75	3.197	0.6	2.916	0.6
1.00	3.012	0.7	2.602	0.6
1.25	2.794	0.4	2.438	0.6
1.50	2.711	0.6	2.333	0.7
1.75	2.630	0.4	2.321	1.0
2.00	2.579	0.6	2.316	0.5

* Standard deviation of the mean, percent relative error.

Appendix C, continued...

Table C-3

EGS Dosimeter Thickness 12 mg/cm^2

Electron Energy (MeV)	DOSE E-8 RAD/(UNIT FLUENCE) PST-Al		PST-PST	
0.05	1.581	0.7*	1.581	0.7
0.10	3.918	0.7	3.923	0.6
0.20	5.288	0.5	5.016	0.5
0.35	5.324	0.7	4.866	0.5
0.50	5.196	0.9	4.773	0.7
0.75	5.260	0.7	4.817	0.5

* Standard deviation of the mean, percent relative error.

Table C-4

CYLTRAN Dosimeter Thickness 12 mg/cm^2

Electron Energy MeV	DOSE E-2 MeV/g PST-Al	PST-PST
0.05	2.512	2.514
0.10	4.983	4.989
0.20	7.451	7.039
0.25	7.748	7.200
0.35	7.968	7.088
0.50	8.122	7.152
0.75	8.091	7.071

* Errors in Dose less than 1.0%

Appendix C, continued...

Table C-5

CYLTRAN Dosimeter Thickness, 31 mg/cm^2

Electron Energy MeV	DOSE MeV/g PST-Al	PST-PST
0.05	0.780*	0.781
0.10	1.555	1.555
0.20	3.092	3.132
0.25	3.773	3.769
0.35	4.262	4.180
0.50	4.694	4.326
0.75	5.039	4.497
1.00	5.266	4.651
1.25	5.386	4.798
1.50	5.481	4.848
1.75	5.672	5.004
2.00	5.565	4.959

* Errors in Dose less than 1%.

Appendix C, continued ...

Table C-6

ACCEPT sphere radius = 200 microns
shell radii 180-200 microns

Electron Energy (MeV)	Energy deposited E-2 (MeV) PST-Al		PST-PST		Dose Ratios
0.20	2.416	1*	1.914	0*	1.262 ± .013
0.30	1.212	1	0.904	0	1.341 ± .013
0.50	0.748	1	0.663	0	1.1282 ± .011
0.75	0.599	1	0.568	1	1.055 ± .015
1.00	0.574	1	0.543	1	1.056 ± .015
1.25	0.526	1	0.517	1	1.018 ± .014
1.50	0.529	1	0.509	1	1.038 ± .015
1.75	0.517	2	0.500	1	1.035 ± .023
22.00	0.513	1	0.491	2	1.046 + .023

* Percent relative error.

Table C-7

ACCEPT sphere radius = 500 microns
shell radii = 480-500 microns

Electron Energy (MeV)	Energy deposited E-2 MeV PST-Al		PST-PST		DOSE RATIO
0.30	1.339	1*	1.158	1	1.156 ± .016
0.35	1.970	1	1.501	0	1.312 ± .013
0.50	1.066	1	0.794	0	1.342 ± .013
0.75	0.696	0	0.614	1	1.134 ± .011
1.00	0.574	1	0.562	1	1.021 + .014

* Percent relative error.

Appendix C, continued ...

Table C-8
Dose Ratio due to a point source at the center of the 200 micron sphere.

Mean radii $\frac{(\text{inner}+\text{outer})}{2}$ (Microns)	ISOTOPE Pm-147	Tl-204	P-32
30	0.999*	1.002	1.004
80	1.002	1.012	1.014
120	1.005	1.042	1.035
150	1.030	1.078	1.050
170	1.086	1.131	1.088
190	1.256	1.257	1.147

* Percent relative error 2% (estimated)

Table C-9

Dose ratio due to a point source at the center of the 500 micron sphere.

Mean radii $\frac{(\text{inner}+\text{outer})}{2}$ (Microns)	ISOTOPE Pm-147	Tl-204	P-32
50	1.000*	1.000	0.998
150	1.002	1.001	0.996
250	1.000	1.008	1.014
325	-	1.020	1.032
375	-	1.045	1.054
410	-	1.070	1.068
430	-	1.100	1.091
450	-	1.132	1.113
470	-	1.182	1.143
490	-	1.297	1.183

* Percent relative error 2% (estimated)

Appendix C, continued ...

Table C-10

Monoenergetic point source at radial position 200 microns sphere radius 200 microns.

Radii (Inner + Outer)/2 Microns	Dose Ratio
10	1.078 ± .209
30	1.150 ± .082
50	1.220 ± .061
70	1.288 ± .044
90	1.292 ± .055
110	1.344 ± .038
130	1.379 ± .031
150	1.422 ± .032
170	1.517 ± .032
190	1.549 ± .022

Table C-11

Monoenergetic point source at radial position 500 microns. Sphere radius 500 microns.

Radii (inner+outer)/2 Microns	Dose Ratio
50	1.405 ± 0.119
150	1.272 ± 0.046
250	1.325 ± 0.019
325	1.347 ± 0.019
375	1.420 ± 0.032
410	1.457 ± 0.033
430	1.494 ± 0.015
450	1.502 ± 0.021
470	1.513 ± 0.021
490	1.526 + 0.026

APPENDIX D

Figure 2-8, p.32

Functional fit for
ln (% Backscatter Dose) vs distance from the interface (X)

$$\ln (\%\ BD) = P1 + P2 * x$$

where

$P1 = 2.03 \pm .12$

$P2 = (-3.8 \pm 1.2) \times 10^{-3}$

Figure 4-19, p.75

Functional form of fit to plotted data.
Dose Ratio = P1 + P2 * EXP(P3* (X-200))

where

For ^{32}P the constants are:

$P1 = 1.005 \pm .005$

$P2 = 0.182 \pm .009$

$P3 = 0.026 \pm .003$

For ^{204}Tl the constants are:

$P1 = 1.006 \pm .005$

$P2 = 0.347 \pm .022$

$P3 = 0.032 \pm .005$

For ^{147}Pm the constants are:

$P1 = 1.000 \pm .001$

$P2 = 0.439 \pm .004$

$P3 = 0.0542 \pm .0007$

Figure 4-20, p.76

Functional form of fit to plotted data.
Dose Ratio = P1 + P2 * EXP (P3* (X-500))

Where X is the radial position

For ^{32}P the constants are:

$P1 = 0.997 \pm .003$

$P2 = 0.205 \pm .005$

$P3 = (11.0 \pm .7) \times 10^{-3}$

For ^{204}Tl the constants are:

$P1 = 1.004 \pm .005$

$P2 = 0.342 \pm .012$

$P3 = 0.019 \pm .001$

Appendix D, cont...

Figure 4-21, p.78

Functional form of fit to plotted data:
Dose Ratio = P1 + P2*EXP (P3* (X-200))

Where X is the radial position

$P1 = 0.982 \pm .005$
$P2 = 0.436 \pm .007$
$P3 = 0.018 \pm .001$

Figure 4-26, p.83

Functional form of fit to plotted data.
Dose Ratio = P1 + P2*X

Where X is the radial position
$P1 = 1.05 \pm 0.02$
$P2 = 0.0026 \pm 0.0001$

Figure 4-27, p.84

Functional form of fit to plotted data
Dose Ratio = P1 + P2*EXP (P3* (X-500))

Where X is the radial position

$P1 = 0.984 \pm .002$
$P2 = 0.386 \pm .004$
$P3 = (7.8 \pm .2) \times 10^{-3}$

Figure 4-31, p.88

Functional form of fit to plotted data
Dose Ratio = P1 + P2*X
Where X is the radial position

$P1 = 1.11 \pm .04$
$P2 = (8.4 \pm .9) \times 10^{-4}$